Measurement of neutrino interactions at an off-axis angle 1.6 degrees using the near-detector INGRID and development of a new neutrino near-detector for the T2K neutrino oscillation experiment

(T2Kニュートリノ振動実験における前置検出器
INGRIDを用いたOff-axis角1.6度での
ニュートリノ反応の研究および
新型ニュートリノ前置検出器の開発)

理学研究科
数物系専攻
金 賢一

Abstract

The T2K project is a long-baseline neutrino oscillation experiment. The neutrino beam is injected from J-PARC in Tokai and the neutrino oscillation is observed at Super-Kamiokande (SK) located 295 km apart from J-PARC. The off-axis method is used in this experiment, the neutrino beam axis is shifted by 2.5 degrees from the direction of SK in order to select the neutrino energy which maximizes the oscillation probability. The peak of the neutrino energy decreases along with the angle from the beam axis (off-axis), so in the large off axis position the neutrino energy becomes low. The stability and intensity of the neutrino beam is monitored by near-detectors located at J-PARC, and one of them is called INGRID. It is located at the beam axis position and consists of iron targets and scintillator tracking planes. It is necessary to understand the neutrino interaction cross section on the iron in order to monitor the neutrino beam precisely by INGRID. However, there are little data as to the sub-GeV region (< 1 GeV), so the uncertainty is large. Then, one of INGRID modules is moved to B2 floor in the near-detector hall, where the off-axis angle is about 1.6 degrees. From measurements for the anti-neutrino beam by the moved module (B2 module), we find no difference between the data and the Monte Carlo simulation. Moreover, the percentage of background events at the B2 module is about 2%, and especially, events from the upstream wall in the detector hall are dominant.

ND280 is also one of near-detectors in the T2K experiment, and measures the neutrino flux before the oscillation. The beam target of ND280 is mainly the hydrocarbon, but the target of SK is the water. This target nucleus difference between near-detectors and the far detector causes the maximum systematic error in the error source in the neutrino oscillation analysis in the T2K. In order to reduce this error, we are planning to construct a new neutrino near-detector for measuring the neutrino cross section ratio between the water and hydrocarbon. The new detector is composed of two water target modules and two hydrocarbon modules, and each module has scintillators which are aligned in the 3D grid-like structure. The light yield of each scintillator is measured by cosmic-rays and we confirm that it is more than 20 p.e. (photon equivalent) and is sufficient for the demand of the detector. Now, one water module is under construction as a prototype detector. The construction work will be finished by the end of Mar. 2016, and we will take the data using it

from Apr. 2016.

Acknowledgment

I am grateful to all the people who have supported me over the years.

First of all, I would like to thank my supervisors. Prof. Yoshihiro Seiya always taught me what the physicist should be. His attitude of working even if it is a holiday inspired me to come to the laboratory everyday. Prof. Kazuhiro Yamamoto always gave me a critical advice. His keen insight into the nature of things is my admiration as a physicist. Prof. emeritus Toru Okusawa often pointed out my mistake at the OCUHEP meeting. His opinions suggest me to find out directions to my research.

In the T2K experiment, I particularly acknowledge Dr. Akihiro Minamino, Prof. Tsuyoshi Nakaya, Prof. A. K. Ichikawa, and Prof. Masashi Yokoyama. They are my role models of a physicist. For students, Taichiro Koga, Tatsuya Hayashino, Keigo Nakamura, Naruhiro Chikuma, Fuminao Hosomi, Tenmon Lou, Ayami Hiramoto, and Yoshie Nakanishi were very reliable. They were my motive power when I was in Tokai, very rough environment Ota-Danchi. Other members, Benjamin, Matthieu, Bastian, Tatiana, and Neha, who helped to construct the WAGASCI detector at J-PARC were my excellent colleagues. They talked with me regardless of my clumsy English. I also appreciate Kento Yoshida who has graduated from Kyoto University. The construction work for the pre-prototype detector with him is my starting point for the WAGASCI experiment. I thank to the cooperation of the KOTO experiment group for the development of the gluing system. Dr. Yosuke Maeda and Dr. Daichi Naito gave me valuable advice and sincerely answered my elementary questions. I also owe a lot to Huang Kunxian who invited me to a hot-pot party, Dr. Kiseki Nakamura who visited Oarai as a pilgrimage together. I was indebted to Eriko Hayashi and Kuniko Kono for my travel allowance.

I am very happy that most of my research time was shared with all the members of my laboratory. I could spend very blessed time and my mind was relaxed during my Master's course. Especially, Keiju Wakamatsu who has graduated from Osaka City University told me basic concepts of the analysis method for the INGRID detector. Jun Harada helped me a lot during my trip to J-PARC.

Finally, I would like to express my deepest gratitude to my family for various supports of my life. Thanks for financial supports and the delicious food.

Contents

Chapter 1

Introduction

1.1 Neutrino

The neutrino is an elementary particle which has no electrical charge and interacts with matter only through the weak interaction. This particle was originally postulated by W.Pauli in 1930[1], and was first detected by Reines and Cowan in 1953 by observing the electron antineutrinos produced in reactors[2]. In 1962, by L.M. Lederman, M. Schwartz, and J.Steinberger, it was shown that there were more than one flavor (type) of neutrino[3], and in 1995, it was revealed at the CERN LEP collider that three neutrino types exist : electron neutrino (ν_e), muon neutrino (ν_μ), and tau neutrino (ν_τ), associating with three charged leptons. Neutrino mass measurements have also been done for a long time, but it only sets upper limits on these masses. These limits were very small, so many physicists considered that neutrino had no mass. That's why in the standard model, neutrino was defined as a massless particle and transformation from the neutrino in one flavor to another flavor was not allowed. However, in 1998, the neutrino oscillation was observed by measuring the atmospheric neutrinos at Super-Kamiokande (SK)[4]. Moreover, in 2001, the oscillation of solar neutrinos was reported by SNO (Sudbury Neutrino Observatory) experiment with a D_2O target[5]. These results indicated a non-zero neutrino mass.

1.2 Neutrino oscillation

1.2.1 Neutrino mixing

If the neutrino has mass, the weak eigenstate (flavor eigenstate) of neutrinos $|\nu_\alpha\rangle(\alpha = e, \mu, \tau)$ could be different from the mass eigenstate $|\nu_i\rangle(i = 1, 2, 3)$ (Fig.1.2.1).

Each weak eigenstate can be described by linear combination as follows :

$$|\nu_\alpha\rangle = \sum_i U_{\alpha i}|\nu_i\rangle. \tag{1.2.1}$$

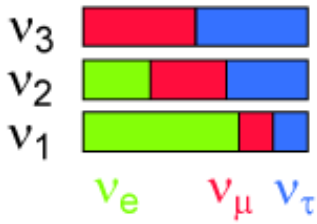

Figure 1.2.1: Neutrino flavor mixing

$U_{\alpha i}$ is a 3 × 3 unitary matrix, called the Pontecorvo-Maki-Nakagawa-Sakata (PMNS) matrix :

$$U_{\alpha i} = \begin{pmatrix} 1 & 0 & 0 \\ 0 & c_{23} & s_{23} \\ 0 & -s_{23} & c_{23} \end{pmatrix} \begin{pmatrix} c_{13} & 0 & s_{13}e^{-i\delta} \\ 0 & 1 & 0 \\ -s_{13}e^{i\delta} & 0 & c_{13} \end{pmatrix} \begin{pmatrix} c_{12} & s_{12} & 0 \\ -s_{12} & c_{12} & 0 \\ 0 & 0 & 1 \end{pmatrix} \tag{1.2.2}$$

$$= \begin{pmatrix} c_{12}s_{13} & s_{12}c_{13} & s_{13}e^{-i\delta} \\ -s_{12}c_{23} - c_{12}s_{13}s_{23}e^{i\delta} & c_{12}c_{23} - s_{12}s_{13}s_{23}e^{i\delta} & c_{13}s_{23} \\ s_{12}s_{23} - c_{12}s_{13}c_{23}e^{i\delta} & c_{12}s_{23} - s_{12}s_{13}c_{23}e^{i\delta} & c_{13}c_{23} \end{pmatrix}, \tag{1.2.3}$$

where $c_{ij} = \cos\theta_{ij}$, $s_{ij} = \sin\theta_{ij}$ (θ_{ij} is a mixing angle), and δ is a CP (Charge and Parity) violating phase.

1.2.2 Neutrino oscillation probability

When a neutrino travels in vacuum, evolution of a mass eigenstate after traveling time t is derived from Schrödinger equation :

$$i\frac{d}{dt}|\nu_i(t)\rangle = H|\nu_i(t)\rangle = E_i|\nu_i(t)\rangle, \tag{1.2.4}$$

$$|\nu_i(t)\rangle = e^{-E_i t}|\nu_i\rangle, \tag{1.2.5}$$

where H is the Hamiltonian, E_i is the energy of the mass eigenstate. Then, the flavor eigenstate at time t can be written as follows :

$$|\nu_\alpha\rangle = \sum_i U_{\alpha i}e^{-E_i t}|\nu_i\rangle. \tag{1.2.6}$$

The neutrino mass is very small, so we can treat it as relativistic particle and use following approximation :

$$E_i = \sqrt{p^2 + m_i^2} \simeq p + \frac{m_i^2}{2p}$$

$$\simeq p + \frac{m_i^2}{2E_i}, \tag{1.2.7}$$

where p, m_i are the momentum and mass of the neutrino eigenstates. Therefore Equation (1.2.6) can be arranged as :

$$|\nu_\alpha\rangle = \sum_i U_{\alpha i}e^{-ipt}e^{\frac{m_i^2}{2E}t}|\nu_i\rangle$$

$$= \sum_{i,\beta} U_{\alpha i}e^{-ipt}e^{\frac{m_i^2}{2E}t}U^\dagger_{\beta i}|\nu_\beta\rangle, \tag{1.2.8}$$

where E is the energy of the neutrino and time-independent parameter.

The probability that ν_β is observed after ν_α traveling the time t is as follows :

$$\begin{aligned} P(\nu_\alpha \to \nu_\beta) &= \left|\langle \nu_\beta | \nu_\alpha(t)\rangle\right|^2 \\ &= \left|\sum_{i,\beta} U_{\alpha i} e^{-ipt} e^{\frac{m_i^2}{2E}t} U^\dagger_{\beta i}\right|^2 \\ &= \sum_{i,j} U^\dagger_{\alpha i} U_{\beta i} U_{\alpha j} U^\dagger_{\beta j} e^{-\frac{i(m_i^2 - m_j^2)L}{2E}}, \end{aligned} \tag{1.2.9}$$

where time t can be replaced with the travel distance L (=ct) in natural system of units, and the term e^{-ipt} is omitted since it only changes the overall phase in the calculation of the neutrino oscillation probability. Using the unitary condition $\sum_i U^\dagger_{\alpha i} U_{\beta i} = \delta_{\alpha\beta}$, Equation (1.2.9) can be re-written :

$$\begin{aligned} P(\nu_\alpha \to \nu_\beta) &= \sum_{i,j} U^\dagger_{\alpha i} U_{\beta i} U_{\alpha j} U^\dagger_{\beta j} e^{-\frac{i\Delta m_{ij}^2 L}{2E}} \\ &= \delta_{\alpha\beta} - 4\sum_{i>j} Re(U^\dagger_{\alpha i} U_{\beta i} U_{\alpha j} U^\dagger_{\beta j}) \sin^2(\frac{\Delta m_{ij}^2 L}{4E}) \\ &+ 2\sum_{i>j} Im(U^\dagger_{\alpha i} U_{\beta i} U_{\alpha j} U^\dagger_{\beta j}) \sin(\frac{\Delta m_{ij}^2 L}{2E}), \end{aligned} \tag{1.2.10}$$

where $\Delta m_{ij}^2 = m_i^2 - m_j^2$. From neutrino experiments up to now, we know that $\Delta m_{21}^2 \ll \left|\Delta m_{31}^2\right| \simeq \left|\Delta m_{32}^2\right|$, so Equation (1.2.10) can be written as below :

$$P(\nu_\alpha \to \nu_\beta) \simeq \delta_{\alpha\beta} + 4\left|U_{\alpha 3}\right|^2 \left(\left|U_{\beta 3}\right|^2 - \delta_{\alpha\beta}\right) \sin^2(\frac{\Delta m_{31}^2 L}{4E}). \tag{1.2.11}$$

Then, $\Delta m_{31}^2 \simeq \Delta m_{32}^2, \theta_{13} \neq 0$, so we can derive the probability about ν_μ from Equation(1.2.10) :

$$P(\nu_\mu \to \nu_e) \simeq \sin^2 2\theta_{13} \sin^2\theta_{23} \sin^2(\frac{1.27\Delta m_{31}^2[\mathrm{eV}^2]L[\mathrm{km}]}{E[\mathrm{GeV}]}), \tag{1.2.12}$$

$$P(\nu_\mu \to \nu_\mu) \simeq 1 - (\cos^4\theta_{13} \sin^2 2\theta_{23} + \sin^2 2\theta_{13} \sin^2\theta_{23}) \sin^2(\frac{1.27\Delta m_{32}^2[\mathrm{eV}^2]L[\mathrm{km}]}{E[\mathrm{GeV}]}), \tag{1.2.13}$$

where the oscillation phase is not written in the natural unit : $\frac{\Delta m^2 L}{4E\hbar e} = \frac{1.27\Delta m^2 L}{E}$. The neutrino energy when the probability $P(\nu_\mu \to \nu_\mu)$ becomes minimum, that is to say, when the probability that neutrino oscillation occurs becomes maximum can be derived from :

$$\frac{1.27\Delta m_{32}^2 L}{E} = \frac{\pi}{2}, \tag{1.2.14}$$

where L is the fixed value in the accelerator experiment, so we can control the neutrino oscillation probability by selecting the neutrino energy appropriately for Equation (1.2.14). As to the T2K experiment, described in Chapter 2, the value of L is 295 km, so the neutrino energy which maximizes the probability of the neutrino oscillation is about 0.6 GeV.

Besides, if we consider the oscillation probability $P(\overline{\nu}_\alpha \to \overline{\nu}_\beta)$, all we have to do is to replace U with $U^\dagger$. So, the positive sign of the third term of Equation (1.2.10) changes to the negative sign. Then, if δ has non-zero value :

$$P(\nu_\alpha \to \nu_\beta) \neq P(\overline{\nu}_\alpha \to \overline{\nu}_\beta). \tag{1.2.15}$$

Equation (1.2.15) indicates the CP violation, that is why δ is called as the CP violation phase.

1.2.3 Neutrino oscillation parameter

Until now, many experiments have measured neutrino oscillation parameters.

$\theta_{32}, \Delta m^2_{23}$

These parameters are referred to as the atmospheric mixing angle and mass splittings. The oscillation of atmospheric neutrinos was discovered at SK, and this result was confirmed by the long baseline accelerator neutrino experiments (K2K[6] and MINOS[7]). The best fit values in PDG 2015 are as follows :

$$\sin^2 2\theta_{23} = 0.999^{+0.001}_{-0.018} \text{ (normal mass hierarchy}^1\text{)}, \tag{1.2.16}$$

$$1.000^{+0.000}_{-0.017} \text{ (inverted mass hierarchy)}, \tag{1.2.17}$$

$$m^2_{32} = (2.42 \pm 0.06) \times 10^{-3}\ \text{eV}^2 \text{ (normal mass hierarchy)}, \tag{1.2.18}$$

$$(2.49 \pm 0.06) \times 10^{-3}\ \text{eV}^2 \text{ (inverted mass hierarchy)}. \tag{1.2.19}$$

$\theta_{21}, \Delta m^2_{12}$

These parameters are referred as the solar mixing angle and mass splittings. The disappearance of electron neutrinos from the sun has been measured by several experiments (SK, SNO, and so on), and this result was confirmed by KamLAND[8] via the disappearance of anti electron neutrinos from reactors. The best fit values in PDG 2015 are as follows :

$$\sin^2 2\theta_{12} = 0.846 \pm 0.021, \tag{1.2.20}$$

$$m^2_{21} = 7.53 \pm 0.16 \times 10^{-5}\ \text{eV}^2. \tag{1.2.21}$$

θ_{13}

Until 2012, this parameter has not been measured precisely and only set the upper limit ($sin2\theta^2_{13} < 0.15$). In 2012, the T2K experiment first reported the indication of ν_e appearance and measured the non-zero θ_{13} value. This result was confirmed by several reactor experiments (Double Chooz[9], Daya Bay[10], and

[1]There are two possible types of the neutrino mass hierarchy : the normal hierarchy ($\Delta m^2_{32} > 0$, $\Delta m^2_{31} > 0$), and the inverted hierarchy ($\Delta m^2_{32} < 0$, $\Delta m^2_{31} < 0$)

RENO[11]). The average fitted value in PDG 2015 is as follows :

$$\sin^2 2\theta_{13} = 8.5 \pm 0.5. \tag{1.2.22}$$

$\underline{\delta}$

This parameter is the CP violation phase, as mentioned above. The measurement of δ comes from atmospheric and accelerator experiments looking at ν_e appearance. Combining the results of the T2K experiment and reactor experiments, δ value can be constrained, and excluded values with 90% confidence level are as follows :

$$\delta \neq 0.19\pi \; to \; 0.80\pi \;\; \text{(normal mass hierarchy)}, \tag{1.2.23}$$

$$-\pi \; to \; -0.97\pi, \; -0.04\pi \; to \; \pi \;\; \text{(inverted mass hierarchy)}. \tag{1.2.24}$$

1.3 Neutrino interaction

There are mainly two modes of neutrino interaction : Charged Current interaction (CC) and Neutral Current interaction (NC). CC interaction produces charged lepton with exchanging a W boson. On the other hand, NC interaction does not produce charged lepton and exchanges a Z boson. The main CC or NC interaction is as follows :

Charged Current Quasi-Elastic interaction (CCQE)

$$\nu_l + n \; \rightarrow \; l^- + p, \tag{1.3.1}$$

where l is a lepton (e, μ, or τ).

Neutral Current elastic interaction (NC elastic)

$$\nu_l + N \; \rightarrow \; \nu_l + N, \tag{1.3.2}$$

where N is a nucleon (p or n).

Charged Current single meson production

$$\nu_l + N \; \rightarrow \; l^- + N^* \; \rightarrow \; l^- + N' + m. \tag{1.3.3}$$

where N* is an intermediate baryon resonance, m is a meson, and N' is a nucleon. Especially, in a few GeV region, the intermediate state is dominated by the Δ(1232) resonance, which mainly decays into a nucleon and a pion (CC1π).

$$\nu_l + N \rightarrow l^- + \Delta \rightarrow l^- + N' + \pi^+. \tag{1.3.4}$$

Neutral Current single meson production

$$\nu_l + N \rightarrow \nu_l + N^* \rightarrow \nu_l + N' + m. \tag{1.3.5}$$

Same as the CC1π interaction, π is produced by the Δ resonance (NC1π).

$$\nu_l + N \rightarrow \nu_l + \Delta \rightarrow \nu_l + N' + \pi. \tag{1.3.6}$$

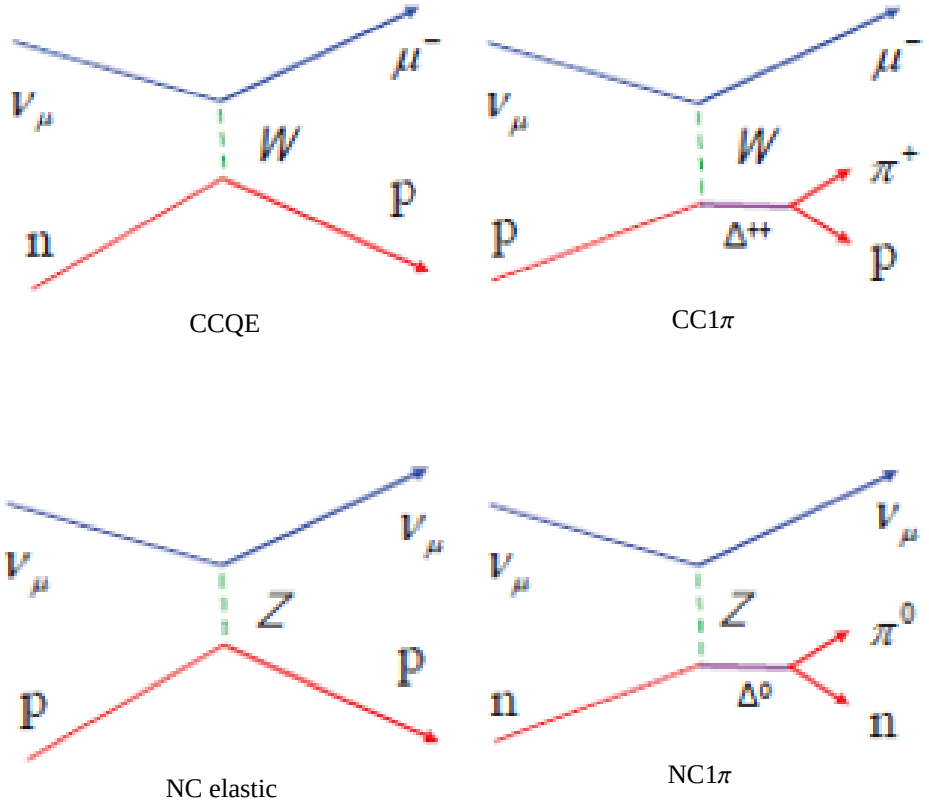

Figure 1.3.1: Diagrams of neutrino interaction

Some supplements are described in Appendix A.

Chapter 2

T2K experiment

2.1 Overview

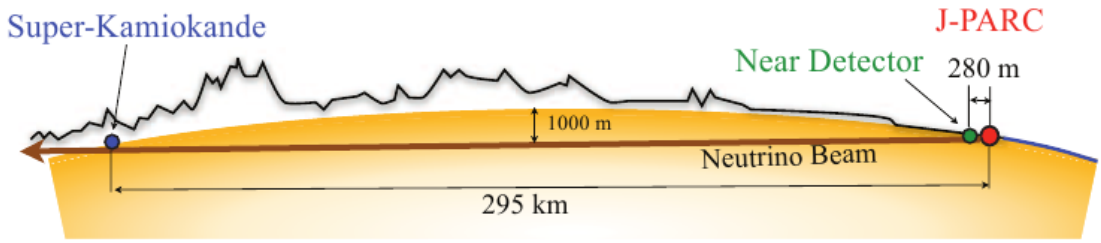

Figure 2.1.1: The T2K experiment

The T2K experiment[12, 13] (Tokai to Kamioka) is a long-baseline accelerator neutrino oscillation experiment, using an intense ν_μ beam. The beam is produced at J-PARC (Japan Proton Accelerator Research Complex) in Tokai, and neutrinos are measured by near-detectors in J-PARC and a far detector SK located 295km away from J-PARC. Neutrino oscillation parameters are determined by measuring the neutrino beam before oscillation at near-detectors and after oscillation at the far detector, respectively. The T2K started to take the data from 2009, and the accumulated POT (Proton On Target) is 7.0×10^{20} for the neutrino mode and 4.0×10^{20} for the antineutrino mode up to 2015[1].

2.1.1 Physics motivation

Primary goals of this experiment are as follows :

- **Measurement of the non-zero $sin^2 2\theta_{13}$ via the ν_e appearance**

  T2K has observed $\nu_\mu \rightarrow \nu_e$ oscillation for the first time in the world and measured the non-zero θ_{13}

[1]The approved total POT is 7.8×10^{21}

value. From Equation (1.2.12), we can write the probability more in detail :

$$P(\nu_\mu \to \nu_e) \simeq \sin^2 2\theta_{13} \sin^2 \theta_{23} \sin^2(\frac{1.27\Delta m^2_{31} L}{E}) - \frac{\sin 2\theta_{12} \sin 2\theta_{23}}{2\theta_{13}} \sin \frac{1.27\Delta m^2_{21} L}{E} \sin^2 2\theta_{13} \sin^2 \frac{1.27\Delta m^2_{31} L}{E} \sin \delta + (\text{CP violation term, matter effect term, and so on}). \quad (2.1.1)$$

Equation (2.1.1) indicates that the measurement of this type of oscillation is sensitive to not only θ_{13} but also δ. So the T2K experiment also aims to measure the δ value with more precise measurements of $\nu_\mu \to \nu_e$ oscillation. Moreover, reactor experiments also have measured θ_{13} value via the anti ν_e disappearance, so it is important to combine results of the T2K and reactor experiments to measure δ.

- **Measurement of $sin^2 2\theta_{23}$ and Δm^2_{32} via the ν_μ disappearance**

  The oscillation probability in this mode is shown in Equation (1.2.13) :

$$P(\nu_\mu \to \nu_\mu) \simeq 1 - (\cos^4 \theta_{13} \sin^2 2\theta_{23} + \sin^2 2\theta_{13} \sin^2 \theta_{23}) \sin^2(\frac{1.27\Delta m^2_{32} L}{E}).$$

  In this equation, θ_{23} accompanies with θ_{13}, so it is important to measure θ_{23} more precisely for understanding neutrino oscillation parameters.

- **Search for sterile components in ν_μ disappearance**

  The sterile neutrino is a hypothetical particle and is considered to interact only through gravitation. It can be measured via the disappearance signal in NC interactions (for example, $\nu + p \to \nu + p + \pi^0$), because they are sensitive to all types of active neutrino and in these interactions we cannot observe any oscillations between active flavors.

2.1.2 Off-axis method

The beam axis (on-axis) is slightly shifted by 2.5 degrees from the direction of SK (off-axis) so that the muon neutrino beam has a narrow energy peak. The ν_μ beam is produced from pion decay $\pi^+ \to \mu^+ + \nu_\mu$ ($\pi^- \to \mu^- \bar{\nu}_\mu$), and the neutrino energy E_ν can be written as follows :

$$E_\nu = \frac{m_\pi^2 - m_\mu^2}{2\,(E_\pi - p_\pi \cos\theta)}, \quad (2.1.2)$$

where m_μ is the muon mass, and m_π, E_π, and p_π are mass, energy, and momentum of a pion, and θ is the angle between pion and neutrino directions. Using this equation, p_π - E_π correlation can be drawn as shown in Fig.2.1.2. If the off-axis angle (OA) is 0 degrees, the neutrino energy increases linearly. On the other hand, if OA is non-zero, the energy spectrum weakly depends on p_π and has a narrow spread. As shown

in Fig.2.1.3, we adjust OA to 2.5 degrees so that the neutrino oscillation probability become maximum at the peak of the neutrino energy spectrum (about 0.6 GeV). Moreover, as described later, CCQE interaction is the signal event of the T2K experiment. In the region where the neutrino energy is smaller than 1 GeV, the ratio of CCQE events to other interaction events increases, as shown in Fig.2.1.4. In short, using OA method, we can measure the neutrino oscillation more efficiently in less background environment. However, there is a correlation between the beam direction and the beam intensity or the energy at SK. So, the beam direction should be monitored carefully.

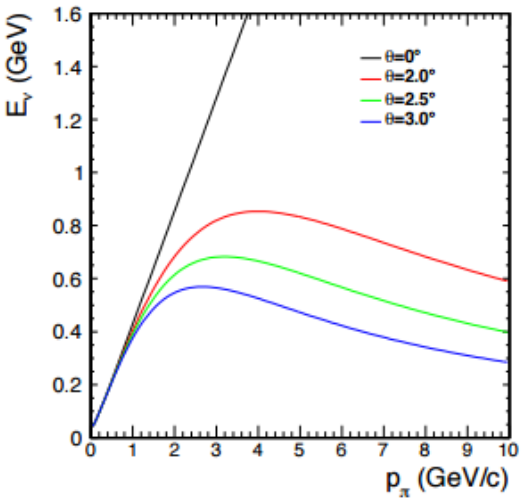

Figure 2.1.2: Relation between the pion momentum and the neutrino energy

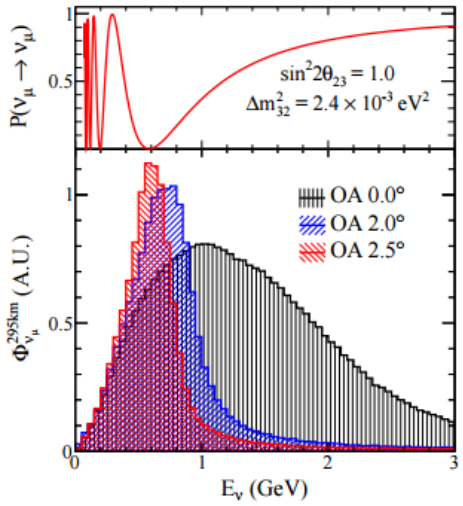

Figure 2.1.3: Neutrino energy and oscillation probability

2.2 J-PARC

2.2.1 Accelerator

J-PARC[14] consists of three types of accelerator, as shown in Fig.2.2.1 : Linear Accelerator (LINAC), Rapid-Cycling Synchrotron (RCS), and Main Ring (MR). The H^- beam is produced at the upper stream of LINAC and accelerated up to 400 MeV, and the beam is converted to the proton beam by charge-stripping foils at the RCS injection. Then, the beam is accelerated up to 3 GeV at RCS, injected to MR, and more accelerated up to 30 GeV every 2 to 3 seconds. In each acceleration, the beam is extracted from MR to the T2K neutrino beam line as a spill. Eight bunches make up one spill in 4.1 μs, as shown in Fig.2.2.2. During the interval time up to next eight bunches, the cosmic data is taken. Parameters and their designed values of the extracted beam are summarized in Table.2.2.1.

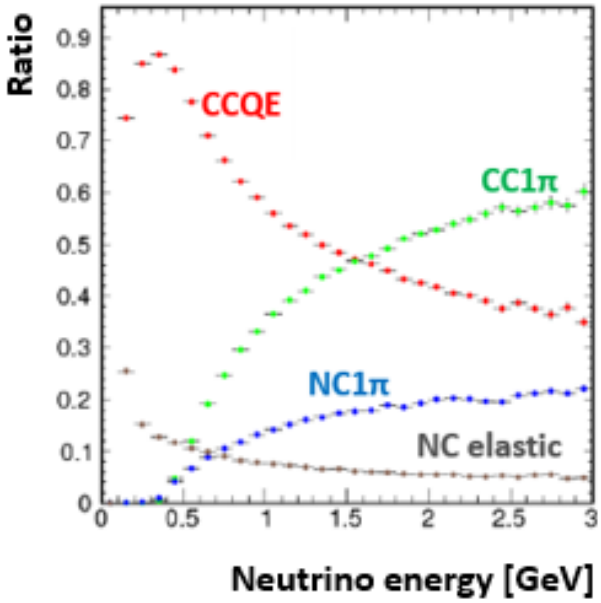

Figure 2.1.4: Ratio between Neutrino interactions

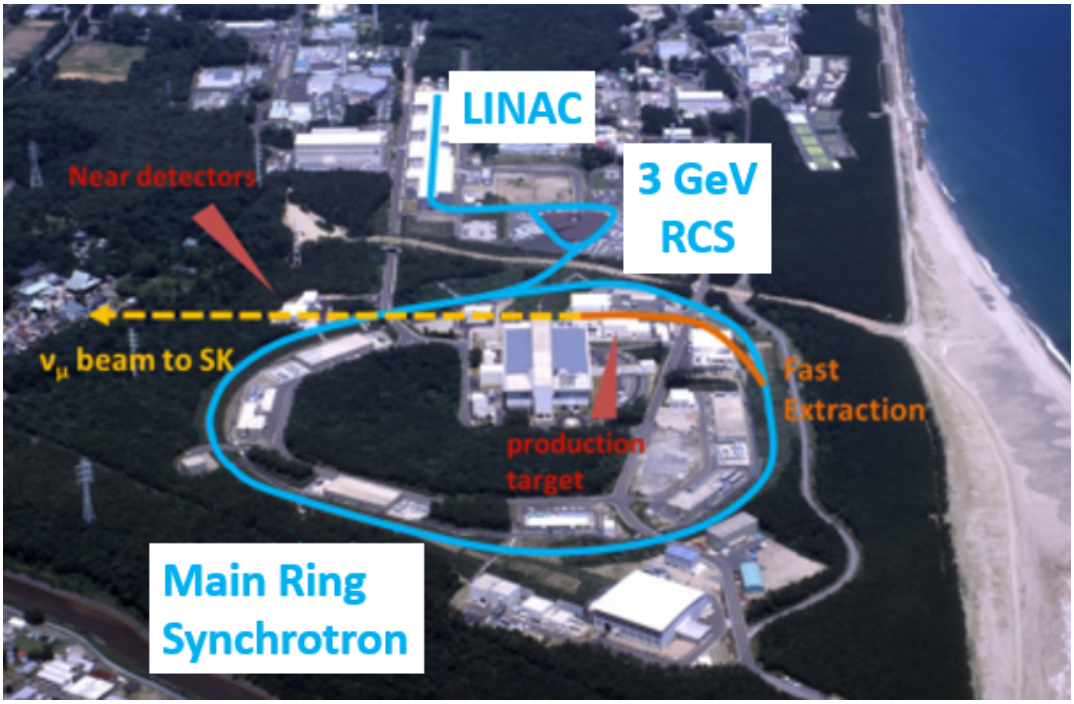

Figure 2.2.1: J-PARC

Table 2.2.1: Designed parameters and values of J-PARC MR

Parameter	Designed value
Beam power	750 kW
Beam kinetic energy	50 GeV
Number of protons	3.3×10^{14} /spill
Number of bunches	8 bunches/spill
Spill interval	3.3 s
Bunch interval	581 ns
Bunch width	58 ns
Spill width	4.1 μs

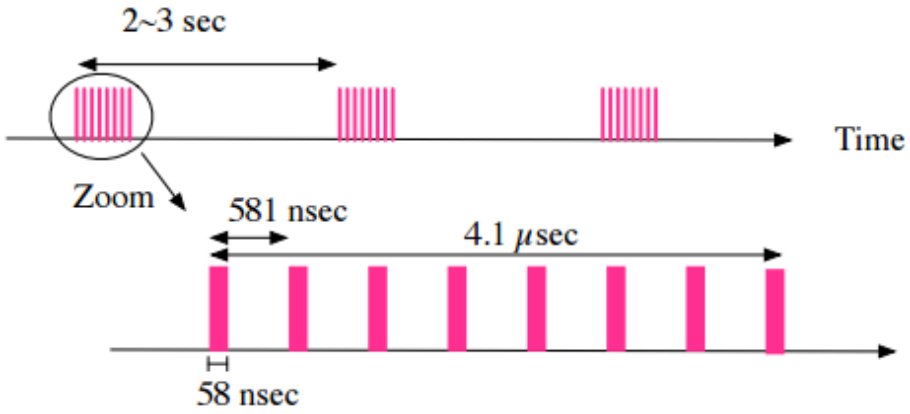

Figure 2.2.2: Scheme of the spill

Now, J-PARC beam intensity is about 400 kW but, as described in Table2.2.1, the designed intensity is 750 kW. It is important to achieve the designed value to obtain more statistics for the T2K experiment.

2.2.2 Neutrino beam line

The neutrino beam line is composed of the primary beam line and the secondary beam line[15, 16], as shown in Fig.2.2.3.

Primary beam line

As shown in Fig.2.2.4, the primary beam line is composed of the preparation section (54 m), the arc section (147 m), and the final focusing section (37 m). In this beam line, 28 super-conductive magnets are connected in series, as shown in Fig.2.2.5. They can generate 2.6 T dipole[2] and 19 T/m quadrapole magnetic field[3] at the same time, in order to bend the proton beam by 80.7 degrees in the arc section. In the final focusing section, there are 10 normal conduction magnets in order to bend the beam downward by 3.637 degrees and focus it to the target.

[2] In order to bend the beam
[3] In order to converge the beam

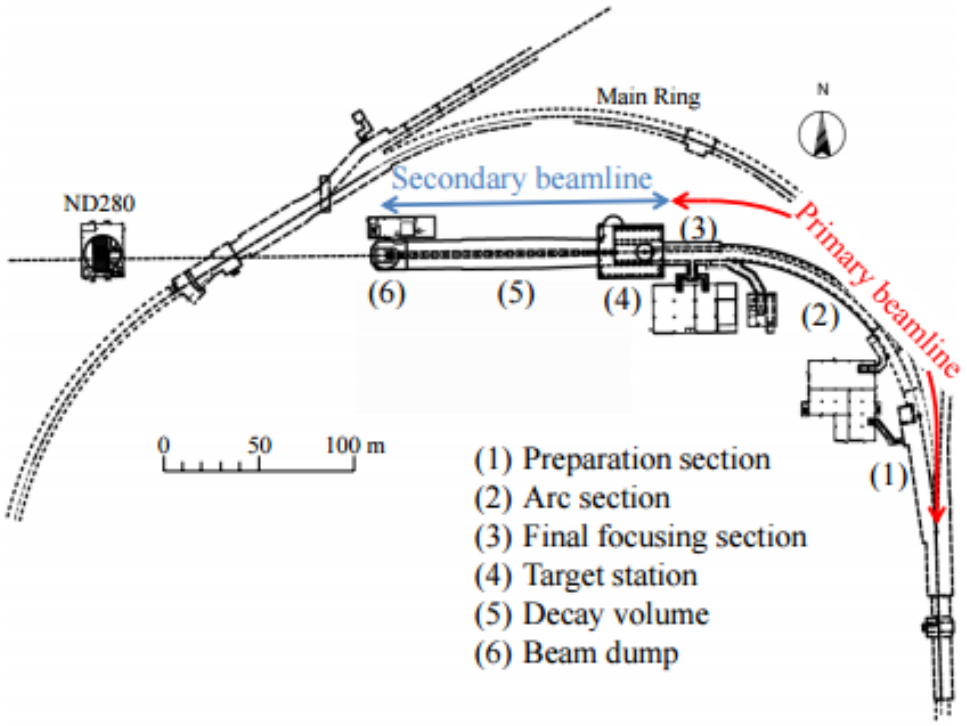

Figure 2.2.3: The neutrino beam line

In order to precisely check the intensity, position, and profile of the proton beam, there are several beam monitors (Fig.2.2.6) : 5 Current Transformers (CT), 21 Electrostatic Monitors (ESM), 19 Segmented Secondary Emission Monitors (SSEM), and 50 Beam Loss Monitors (BLM).

Beam intensity and timing monitor : CT

The CT is a toroidal coil around a cylindrical ferromagnetic core. It reads out the induced current which is generated from the toroidal magnetic field by the proton beam, and monitors the number of protons in the beam. The beam intensity can be measured with 2% accuracy.

Beam position monitor : ESM

The ESM is composed of four segmented cylindrical electrodes surrounding the proton beam orbit. It measures the charged current induced to each electrode by the proton beam. Comparing the amount of each induced current, the projected beam position can be measured with 450 μm accuracy.

Beam profile monitor : SSEM

The SSEM has two 5 μm titanium foil strips oriented horizontally and vertically to the beam axis. It detects secondary electrons which are produced in the interaction of protons with the foil and induce currents on strips.

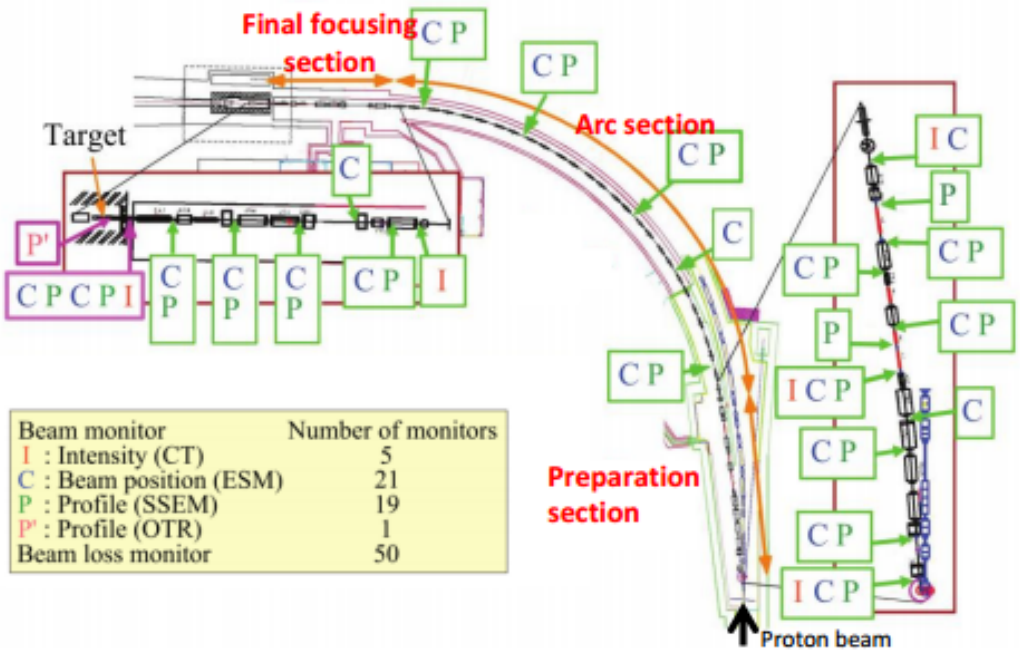

Figure 2.2.4: The primary beam line

Figure 2.2.5: Super-conductive magnets

Beam loss monitor : BLM

The BLM is a Ar-CO_2 mixture gas filled proportional chamber. The beam abort signal is fired when the beam loss integrated during each spill exceeds a threshold.

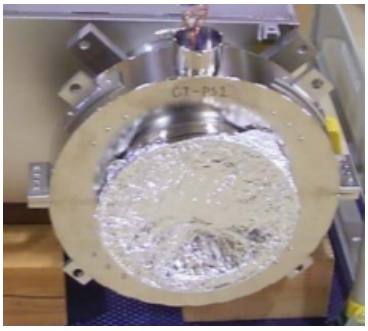

CT

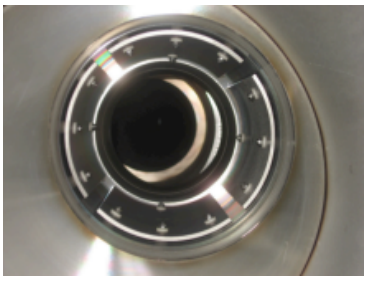

ESM

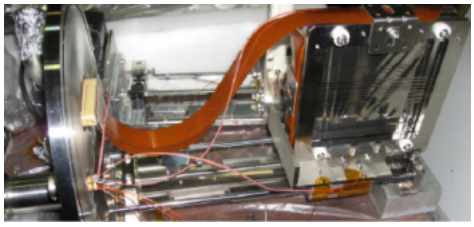

SSEM

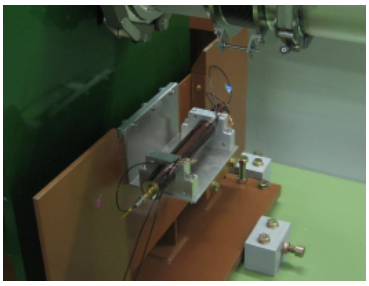

BLM

Figure 2.2.6: Beam monitors in the primary beam line

In addition, the Optical Transition Radiation monitor (OTR, Fig.2.2.7) is placed 30 cm upstream of the target. It measures two dimensional beam profiles by imaging the light come from the transition radiation which are produced when the beam crosses a 50 μm thick titanium alloy foil. Just the upstream of the OTR, the carbon block (1.7 m $\times$ 0.3 m $\times$ 0.4 m) is placed in order to protect machines downstream if the beam position is largely shifted.

Secondary beam line

In the secondary beam line (Fig.2.2.8), there are mainly four sections : the target station, decay volue, beam dump, and muon monitor.

Target station

The target station consists of the proton beam target (Fig.2.2.9) and 3 magnetic horns (Fig.2.2.10). In the first horn (Horn 1), there is a graphite rod (2.6 cm diameter, 91.4 cm long) as the pion production target. Produced pions are focus to the direction of SK by using 3 horns in order to maximize the

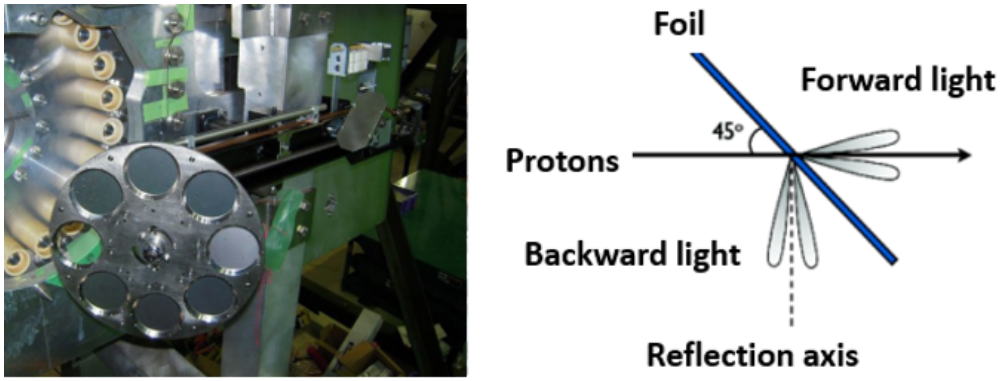

Figure 2.2.7: OTR

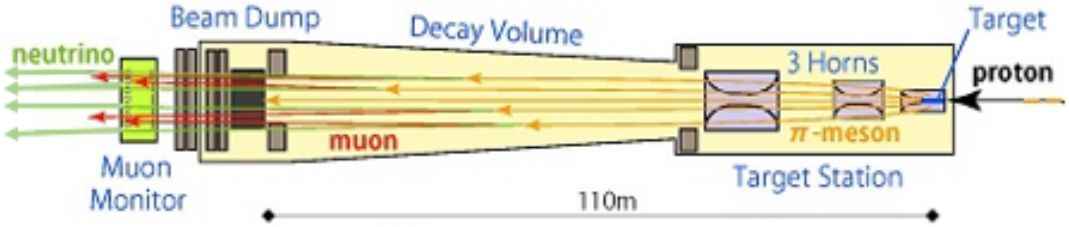

Figure 2.2.8: The secondary beam line

neutrino flux at SK. Each horn consists of two coaxial conductors, and the inside diameter is as small as possible to achieve the maximum magnetic field[4], 2.1 T for the current at 320kA[5]. When the polarity of the horn current is inverted, in turn negative pions are focused to SK and anti-neutrinos are produced. That is to say, we can change the beam mode by the horn current polarity.

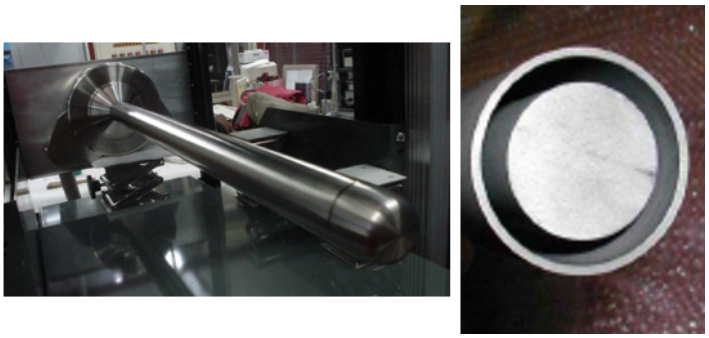

Figure 2.2.9: The neutrino beam target : It consists of graphite (inner) and titanium alloy (outer), and the helium gas flows between the layer for absorbing. During the beam operation, the temperature of the target center is about 700 C°

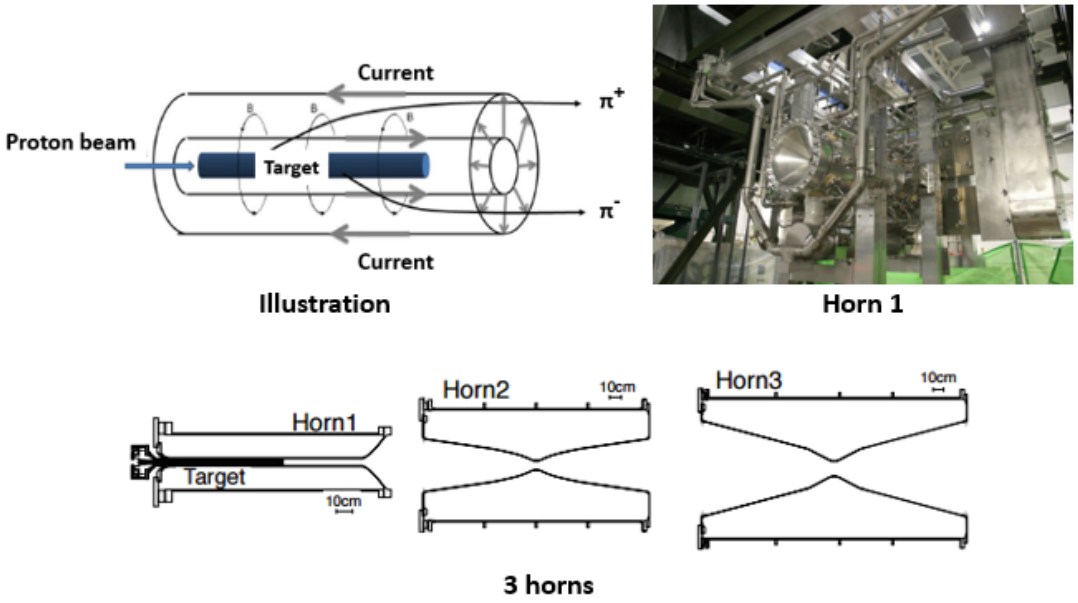

Figure 2.2.10: Electromagnetic horns

Decay volume and beam dump

Pions produced in the Horn decay to muon neutrinos and muons in the decay volume, 96m long steel tunnel, as shown in the left of Fig.2.2.11. There are a lot of water cooling tubes for cooig the heat from secondary particles. At the end of the decay volume, there is a beam dump (Fig.2.2.12) in order to stop low energy particles except for neutrinos, such as protons which did not interact with the target. The beam dump consists of graphite blocks (3.174 m long, 1.94 m wide, and the 4.69 m

[4]The magnetic field varies as 1 / r, where r is the diameter of the conductor.
[5]J-PARC horn current is 250kA as of Feb. 12, 2016.

high) and cooling aluminum modules.

Figure 2.2.11: Decay volume

Figure 2.2.12: Beam dump

Muon Monitor (MUMON)

The MUMON[17] (Fig.2.2.13) is positioned just behind the beam dump, and 118 m far away from the target. It indirectly measures the neutrino beam direction by monitoring the direction of muons which have more than 5 GeV/c momentum and penetrate the beam dump. It consists of silicon PIN photo-diodes array (upstream side) and ionization chambers array (downstream side). Each array has 7×7 sensors at 25 cm intervals, and covers 150×150 cm^2 area.

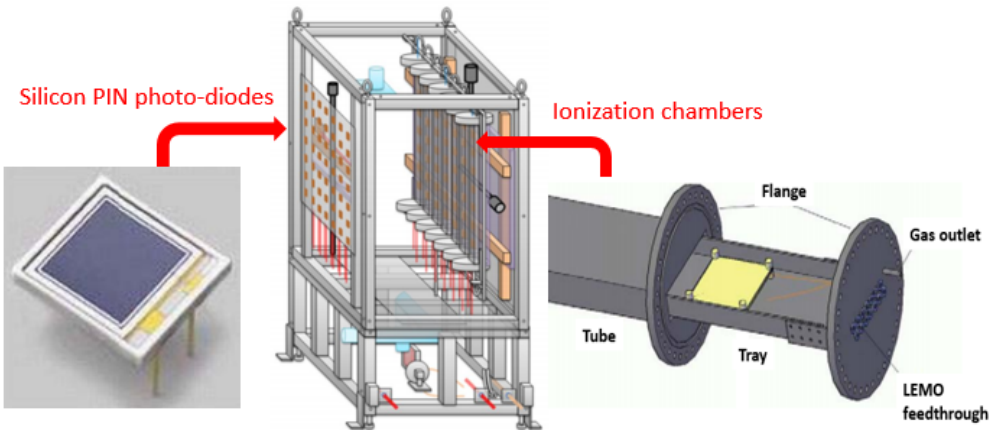

Figure 2.2.13: Muon monitor

2.3 Neutrino beam detector

Detectors for measuring the neutrino flux in the T2K experiment are broadly classified into two types : near-detectors and the far-detector.

2.3.1 Near-detectors

The T2K near-detectors consist of the neutrino spectrometer ND280 and the neutrino beam monitor INGRID, and they are located at the near-detector hall (Fig.2.3.1), 280 m downstream from the neutrino production target.

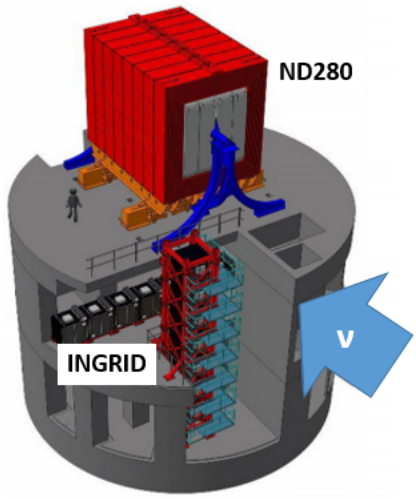

Figure 2.3.1: Near-detectors at the near-detector hall

Off-axis detector : ND280

ND280[18] (Fig.2.3.2) measures the neutrino flux, energy spectrum, and neutrino-nucleus cross sections before the neutrino oscillation. It is placed in the off-axis (2.5 degrees) direction. It is a complex detector containing several detectors in the magnet.

Magnet

The magnet of ND280 consists of aluminum coils which generate the 2 T dipole magnetic field to measure momenta and charges of charged particles produced in neutrino interactions. The inner size of the magnet is 3.5 m $\times$ 3.6 m $\times$ 7.0 m. It was originally used in the UA1 experiment[19] and the NOMAD experiment[20] at CERN, and then was donated to the T2K experiment.

Pi-zero detector (PØD)

PØD is located at the most upstream side in the magnet, and is composed of a sandwich structure of lead and plastic scintillators. It measures π^0 produced by NC interactions. As described below, events from NCπ^0 interactions could be background events for detecting signal events at SK.

Tracker

ND280 has two types of trackers : The time projection chamber (TPC) and fine grained detector (FGD).

- TPC

  This is the tracker for the long track, especially leptons in the final state of CC interactions[21]. There are three TPCs in ND280, and they use a gas mixture of Ar:CF_4:iC_4H_{10} (95%:3%:2%). They reconstruct the energy of neutrinos by measuring momenta of charged particles from the track curvature in the magnetic field. Moreover, they are used for the particle ($\mu^{\pm}$, $\pi^{\pm}$,and $e^{\pm}$) identification by measuring the energy loss of charged particles in the gas.

- FGD

  Two FGDs contain of layers of fine-grained plastic scintillator bars[22]. FGDs are used for the neutrino target, and they identify the types of neutrino interactions by detecting all short-ranged charged particles produced by neutrino interactions around the interaction vertex. The second FGD consists of not only scintillators but also the water[6], so we can measure neutrino interactions on water which is also the target in SK.

Electro magnetic calorimeter (ECAL)

ECAL surrounds PØD, TPCs, and FGDs, and is composed of plastic scintillator layers and lead foils. It measures the energy of γ-rays from π^0 decays and electrons produced by CC interactions in inner detectors, and then reconstructs π^0 and identifies electrons.

Side muon range detector (SMRD)

SMRDs consist of plastic scintillator pads, and they are inserted between each magnet iron yoke, and It measures the momentum of muons which go in the side way of FGDs and are not detected by TPCs.

On-axis detector

INGRID

INGRID[23] is a detector for monitoring the neutrino beam direction and intensity by measuring neutrino interactions. It consists of 14 modules each of which is composed of 9 ion plates and 11 tracking plates. 7 modules are placed horizontally, and other 7 modules are placed vertically, as shown in Fig.2.3.3. Details of this detector is mentioned in Chapter 3.

[6]The volume ratio between the scintillator and water is about 50 : 50.

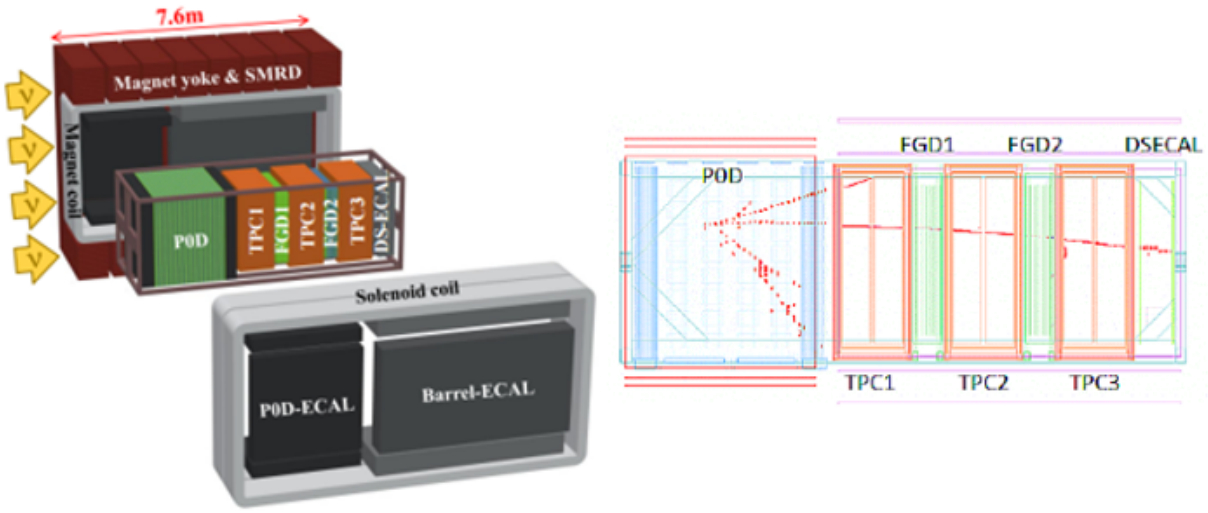

Figure 2.3.2: ND280

Proton Module

Proton Module (Fig.2.3.4) is an extra module located at the on-axis position between INGRID horizontal and vertical modules. It consists of only scintillator strips, so it is a fully-active tracking detector. It measures protons and pions produced by neutrino interactions to understand more details about neutrino interaction types, and also measures the neutrino cross section for each interaction type.

2.3.2 Far-detector : Super-Kamiokande

SK (Fig.2.3.5) is the 50 kton water Cherenkov detector with 22.5 kton fiducial volume, and is located at 295 km far away from J-PARC, 1000 m deep inside Kamioka mine. In the SK, there are two types of the cylindrical shaped water tank : the Inner Detector (ID) and the Outer Detector (OD). The ID, the size of which is 36.2 m high and 33.8 m in diameter, contains 11129 inward-facing 20-inch Photo-Multipliers (PMT) in its cylindrical wall. In the OD, there are 1885 outward-facing 8-inch PMTs for excluding backgrounds from the cosmic-ray. Neutrino events are detected with these PMTs in the ID by measuring with the 4 π acceptance the Cherenkov light[7] emitted by charged particles which are produced from the neutrino interaction in the water. Fig.2.3.6 shows rings of the Cherenkov light by the muon, electron, and π^0. From the timing and position of this lights, the vertex, energies, and directions of charged particles are reconstructed. The muon

[7] If the charged particle passes through a water at a speed greater than the phase velocity of light in the water, the Cherenkov light is emitted to the direction θ which is given by $\cos\theta = \frac{1}{n\beta}$, where n is the refractive index and $\beta = v/c$ is the velocity of the charged particle.

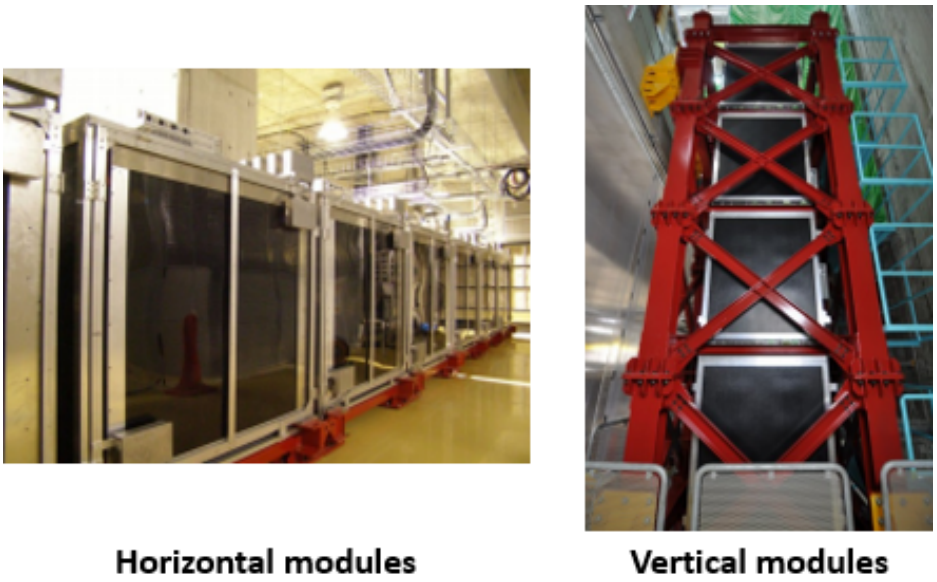

Figure 2.3.3: INGRID horizontal and vertical modules

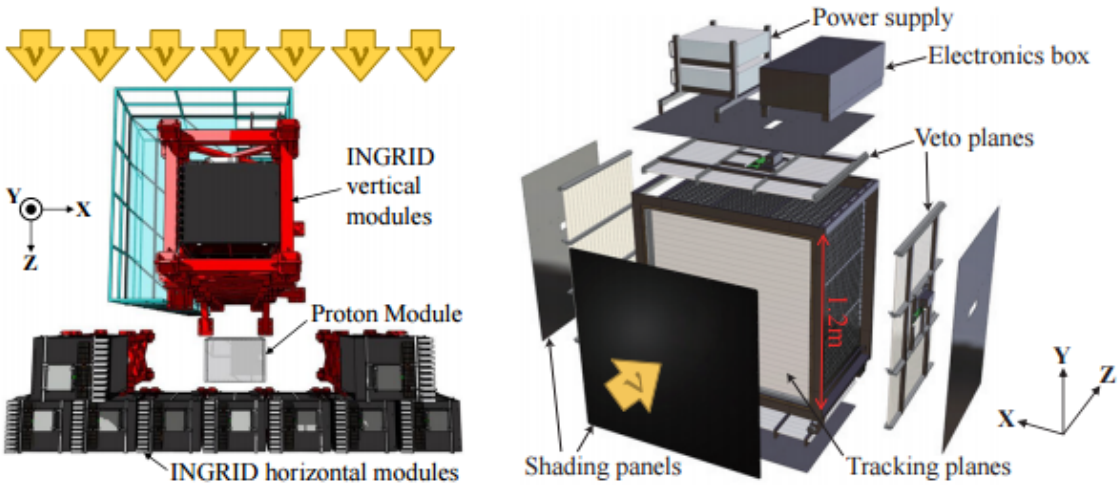

Figure 2.3.4: Proton Module

has relatively large mass, so it has a sharp ring edge. On the other hand, the electron produces a fussy ring edge due to electromagnetic showers. From that difference of the ring shape, we can distinguish the muon from the electron. Also, π^0 has a fussy ring pattern because it decays to 2γ and they induce electromagnetic showers, so it could be the background for identifying the electron. CCQE interaction is the signal event for the T2K experiment and this interaction does not produce π^0, but CC1π or NC1π interaction does. So, it is important to reduce such background events by the off-axis method, as mentioned in Sec.2.1.2.

GPS is used to identify neutrinos in SK with those produced at J-PARC[24]. The timings T_{SK} at which T2K events are observed by the SK is derived from

$$T_{SK} = T_{Trigger} + T_{Delay} + T_{TOF}, \tag{2.3.1}$$

where $T_{Trigger}$ is the beam timing measured by VME module, named Local-Time-Clock (LTC), as shown in Fig.2.3.7. T_{Delay} is the delay time until the proton beam hits the target, and is measured by the distance between the beam injection point and the target from the GPS information. T_{TOF} is the neutrino flight time to SK, and is also measured by GPS. There are two GPSs at both J-PARC and SK in case one of them is broken.

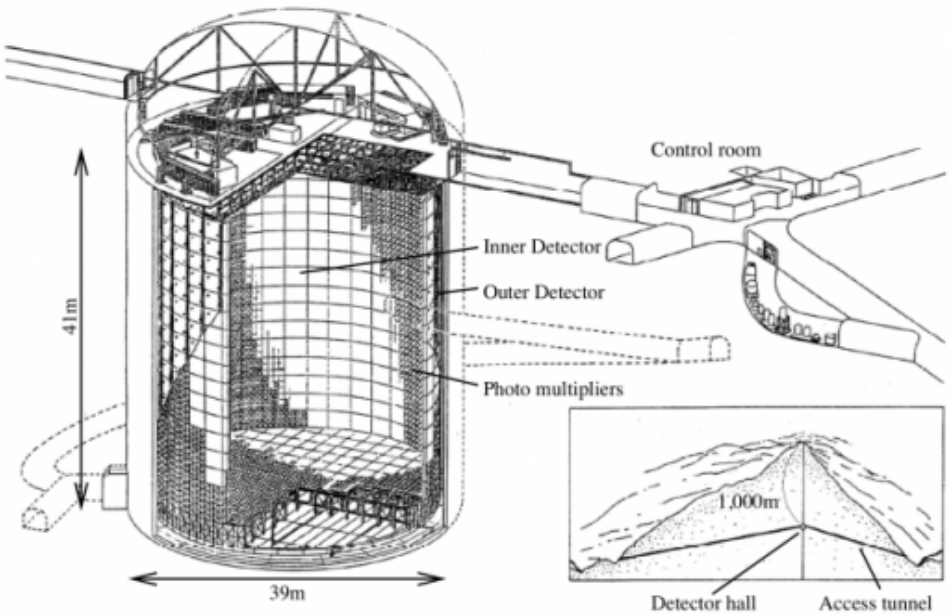

Figure 2.3.5: Super-Kamiokande

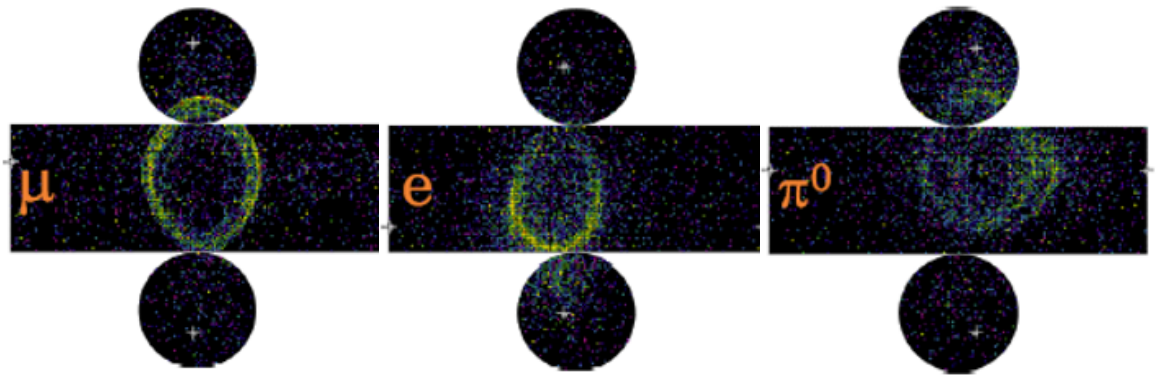

Figure 2.3.6: Ring of Cherenkov light by muon, electron, and π^0

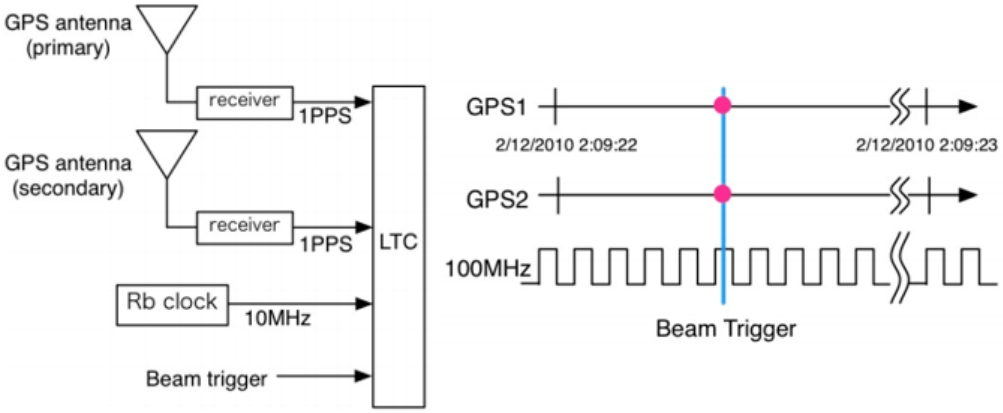

Figure 2.3.7: Measurement for the beam timing

Chapter 3

T2K on-axis near-detector : INGRID

3.1 Requirements for INGRID

There are mainly 3 requirements for the INGRID detector[25].

3.1.1 Beam direction

As mentioned in Sec.2.1.2, there is the correlation between the neutrino beam direction and the beam energy. Due to the beam direction displacement only by 1 mrad, the peak value of the neutrino energy spectrum and the flux varies 2% and 3% respectively. It is important to decrease these errors to suppress the systematic error of the neutrino oscillation parameter. Then, INGRID is required to measure the beam direction within 1 mrad. It is positioned 280 downstream from the beam production target, so the beam direction measurement within 280 m $\times$ 1 mrad = 0.28 m is needed.

3.1.2 Beam profile

Fig.3.1.1 shows the expected neutrino beam profile. The spatial width (1σ) of the neutrino beam at the location of INGRID is large, so it is necessary for INGRID to cover ± 5 m region to reconstruct the beam center.

3.1.3 Beam target

INGRID is required to measure the beam direction by using the 1 month data while the beam intensity is 1% of the nominal value[1]. The expected number of events in ± 5 m region from the beam center is about 2000 events/ton/month. Provided that the detection efficiency for the neutrino event is 20%, 25 to 50 ton mass is needed for the neutrino beam target to suppress the statistical error of the number of events by 2%.

[1]This period is called beam commissioning period. The beam commissioning is done between physics data taking periods.

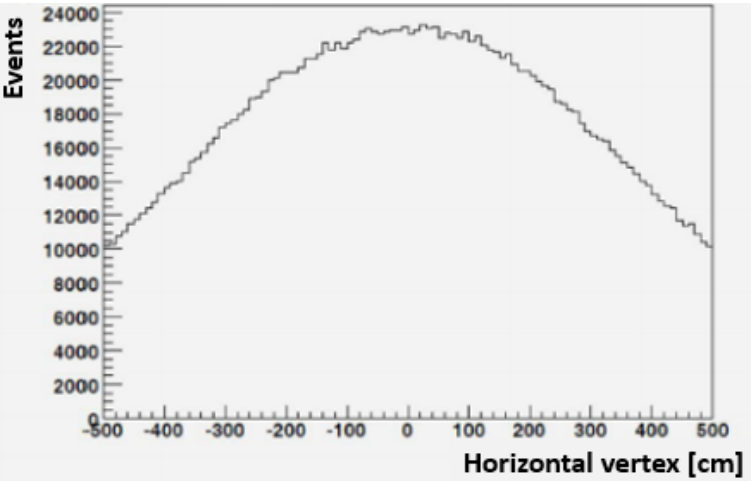

Figure 3.1.1: Expected profile of the neutrino beam at INGRID : 0 indicates the beam center position.

3.2 Overview of INGRID

INGRID detector is located at 280 m downstream from the neutrino production target. It consists of 14 modules arranged in horizontal and vertical arrays, as shown in Fig.3.2.1. It covers ±5 m around the beam axis, and detects neutrino interactions to monitor the initial neutrino beam intensity, direction, and stability. Two modules are placed at the shoulder position of vertical modules and they are used for measuring the distortion of the neutrino beam. As described more in detail in Chapter 5, one of these shoulder modules are moved to the different position to measure lower energy neutrino events. The size of each module is 1.2 m $\times$ 1.2 m $\times$ 0.9 m. The weight of each INGRID module is about 6.6 ton, and it is expected to detect 2600 events/ton/month. In this thesis, INGRID means 14 cruciform modules. Other 2 modules are called INGRID shoulder module and INGRID B2 module, respectively.

3.3 Detector components

There are mainly 3 components in INGRID : iron target planes, tracking planes, veto planes, as shown in Fig.3.3.1.

3.3.1 Iron target

95.2% of neutrino interactions in INGRID are generated in iron planes. Each plane has 6.5 cm thickness along the beam direction, and the size of it is 1.2 m $\times$ 1.2 m. There are 9 iron targets in each module of INGRID, and the total mass is about 7065 kg/module.

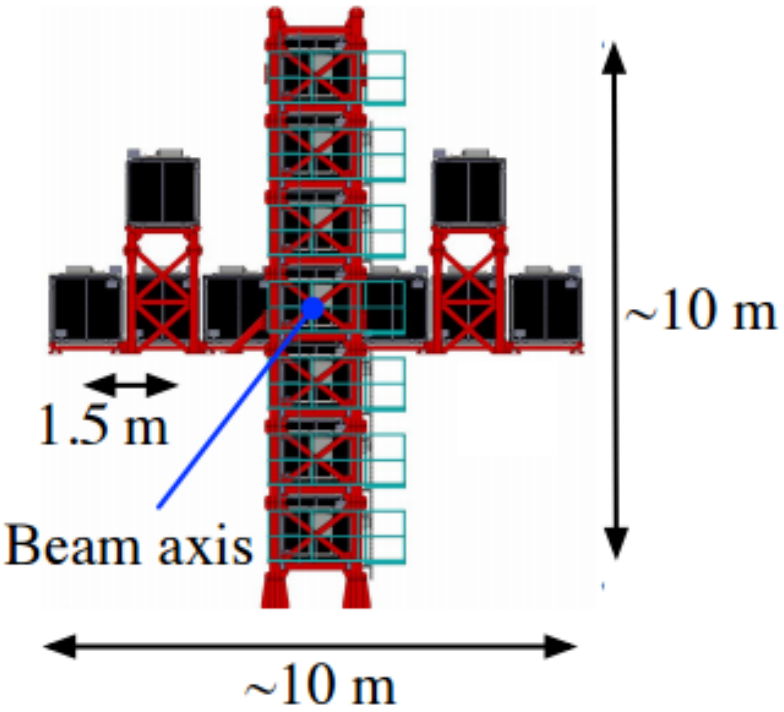

Figure 3.2.1: INGRID detector

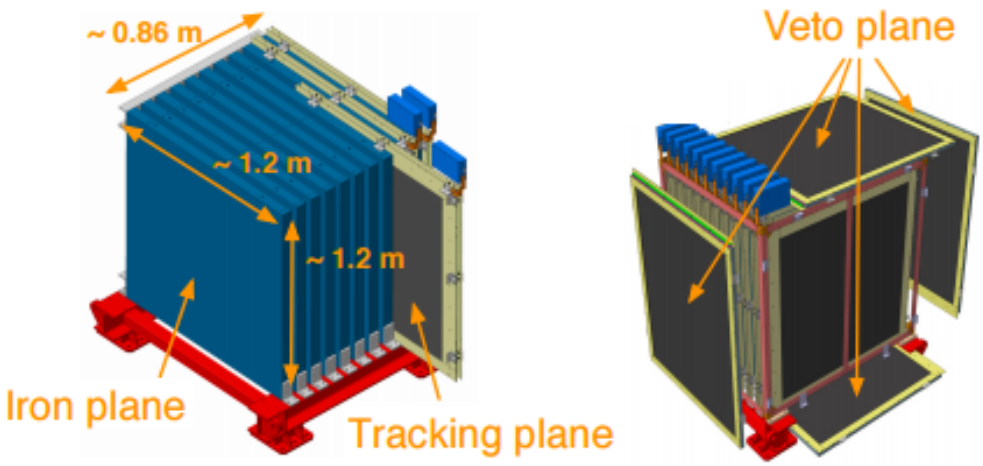

Figure 3.3.1: INGRID detector components

3.3.2 Tracking plane

Tracking planes mainly contain plastic scintillators, WLS fibers, and MPPCs. Scintillators emit lights when charged particles are produced in iron targets by neutrino interactions, and the light is absorbed and re-emitted by WLS fibers. After the emitted lights propagate in the WLS fiber, these lights are detected by MPPCs, and then converted to the electric signal. This mechanism is shown in Fig.3.3.2.

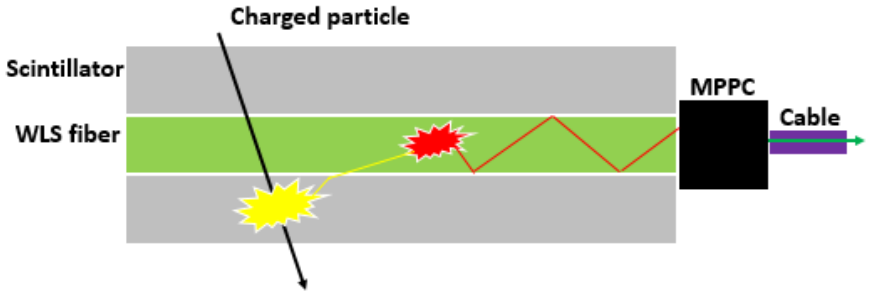

Figure 3.3.2: Illustration for how to detect the light by MPPC

- **Plastic scintillator**

  Each tracking plane consists of two scintillator layers. One of them has 12 scintillators in the horizontal directions (X layers) and the other has 12 scintillators in the vertical directions (Y layers). These scintillators (Fig.3.3.3) were produced at Fermilab, and they are made of polystyrene, infused with PPO[2] (1% by weight) and POPOP[3] (0.03% by weight), and are produced by extrusion in the shape of rectangular (1.0 cm $\times$ 5.0 cm), with the white reflective coating composed of TiO_2 infused in polystyrene (15% by weight). Measured parameters of scintillators are listed on Table.3.3.1.

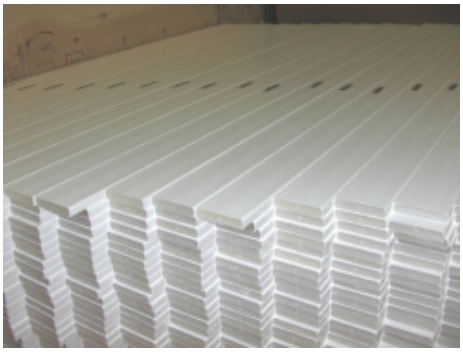

Figure 3.3.3: Scintillators produced at Fermilab (Dec. 2007 - Feb. 2008) : The total number is 10,272 and the total weight is about 6.2 ton.

[2] 2,5-diphenyloxazole ($C_{15}H_{11}NO$)
[3] 1,4-Bis-[2-(5-phenyloxazolyl)]-benzene ($C_{24}H_{16}N_2O_2$)

Table 3.3.1: Measured parameters of scintillators. In total, 349 scintillators were measured.

Parameter	Mean	RMS
Width	50.01 mm	0.062 mm
Thickness	9.921 mm	0.094 mm
Length	1203 mm	0.42 mm
Weight	602.1 g	2.8 g

The center of each scintillator bar has a hole to insert the WLS fiber. One side of the rectangular face, far from the light readout side, is painted with the white reflective coating[4].

- **WLS fiber**

For INGRID, Y11(200)MS fibers by Kuraray[26] are used for the light collection. Y-11, 200, and MS mean the type of the wave length shifting material, the product of the concentration of the WLS material and the diameter of the fiber (the unit is [ppm·mm]), and the multi-clad[5] S type, respectively. The spec of the fiber is listed in Table.3.3.2. The diameter of the fiber is 1 mm and this is well fitted to the size of the light receiving surface of MPPC (1.3×1.3 mm^2). Spectra of the absorption and emission of the fiber is shown in Fig.3.3.4. The peak wave length of the absorption is 430 nm, and this is almost overlapped with the emission peak wavelength of the scintillator (425 nm). The peak wavelength of the emission is 460 nm, so the self-absorption in the fiber is small and the light emission quantum efficiency in this region is about 70%.

One of edges of the fiber is polished by the diamond cutter[6] in order to prevent the light reflection, and it is glued with GOMI connector[7] (Fig.3.3.5) by the optical cement[8] to be connected to the MPPC. The other edge of the fiber is not polished and is painted with the reflective coating to increase the light yield.

Table 3.3.2: The spec of Y-11(200)MS

Parameter	Designed value
Diameter	1.0 mm
Refractive index of core	1.59
Refractive index of inner cladding	1.49
Refractive index of outer cladding	1.42
Peak wavelength of absorption	430 mm
Peak wavelength of emission	460 mm
Attenuation length	$\sim$ 3 m

- **MPPC**

MPPC[27] (Fig.3.3.6) is one of the new semi-conductor photodetectors, and is used in INGRID to read out the scintillation light as the electric signal. MPPC has 667 square regions of 1.3 mm^2, named

[4] EJ-500, made by ELJEN Technology

[5] The fiber core is surrounded by two clads each of which has different refractive index. Multi-clad type fiber has larger angle which meets the total reflection condition than single-clad type, and it means that the former can obtain more light yield.

[6] Fiberfin 4, made by Fiberfin Inc.

[7] GOMI (General Optical MPPC Injection) Connector was developed by Kyoto University High energy group, and is used to reduce the loss of the light yield.

[8] EJ-500, made by ELJEN Technology

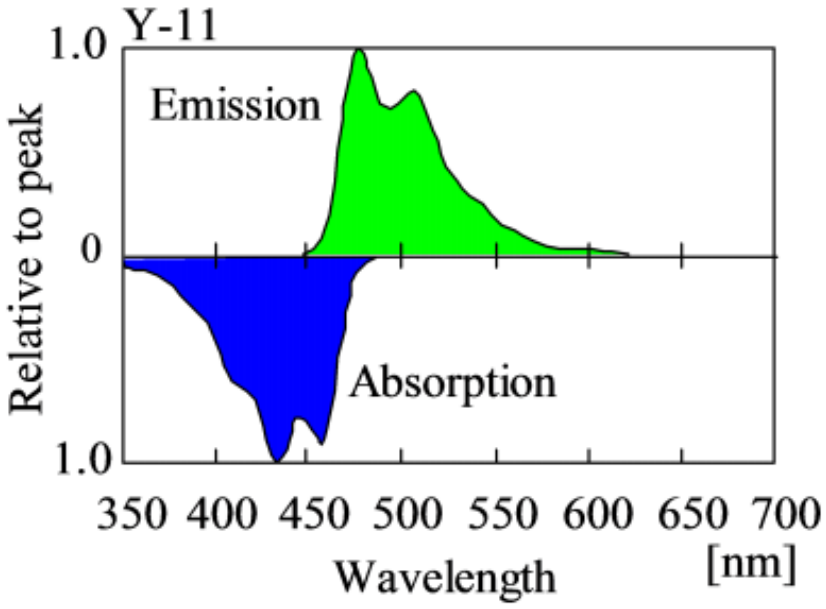

Figure 3.3.4: Absorption and emission spectra of WLS fiber, Y11(200)MS

Figure 3.3.5: GOMI connector

APD (Avalanche Photo Diode) pixels. If a photon is injected to an APD, a photoelectron is produced. Accelerating the photoelectron by the bias voltage applied to APD, electrons are generated in chains and the signal is amplified. In general, the electron charge is in proportion to the number of injected photons, and the gain in MPPC is less than 100. However, if the bias voltage is higher than a certain voltage, called breakdown voltage, the gain becomes 10^5 to 10^6 and the electron charge is constant. The former condition is referred to as the normal mode, and the latter as the Geiger mode. In the Geiger mode, the electron charge Q_{signal} per pixel can be calculated as follows :

$$\begin{aligned} Q_{signal} &= C(V_{bias} - V_{bd}) \\ &\equiv C\Delta V, \end{aligned} \tag{3.3.1}$$

where C is the capacitance of the APD pixel, V_{bias} is the bias voltage, V_{bd} is the breakdown voltage, and ΔV is called the over voltage. The gain is derived from Equation (3.3.1) :

$$\text{(Gain)} = \frac{Q_{signal}}{e} \tag{3.3.2}$$

$$= \frac{C}{e}\Delta V. \tag{3.3.3}$$

The breakdown voltage depends on the temperature, so it is important to keep it and set the appropriate bias voltage to maintain the constant gain.

MPPC has great features such as high photon detection efficiency (40% at 500 nm) high gain, the capability of photon counting, and it is not affected by the magnetic field. On the other hand, it has the disadvantage of noises.

- **Dark noise**

  The signal is generated not only by photoelectrons but also thermo electrons or the tunnel effect. Such noise cannot be distinguished from the true signal because the same magnityde of the signal is outputted corresponding to ΔV. The number of dark noises per second is called the noise rate. The larger the bias voltage is and the higher the temperature is, the higher the noise rate becomes. In the T2K detector, as mentioned later, the effect of the dark noise is suppressed by measuring the beam hit timing.

- **Crosstalk**

  When the photon is detected in a APD pixel and the electron avalanche happens, photons produced in the avalanche could be detected by anothe APD pixel and generate another avalanche

Table 3.3.3: The demand for T2K near-detectors to MPPC

	INGRID	ND280
Number of pixels	> 100	> 400
Gain	$> 5 \times 10^5$	$\sim 10^6$
Noise rate	< 1.5 MHz	< 1.5 MHz
Photon detection efficiency	> 10%	> 10%
Number of channels	10,000	50,000

Table 3.3.4: The spec of MPPC (S10362-13-050C)

Parameter	Designed value
Active region	1.3×1.3 mm^2
Size of pixel	50×50 μm^2
Number of pixels	667
Operating voltage	70 V
Gain	7.5×10^5
Photon detection efficiency	$\sim$ 30%
Dark noise (If the gain is 7.5×10^5)	< 1.35Mcps (0.5 p.e. threshold, 25 ℃) < 0.135 Mcps (1.5 p.e. threshold, 25 ℃)
Attenuation length	3m

and it causes the extra signal in MPPC. This phenomenon is called the crosstalk and is prevented by measuring the crosstalk in advance and remove from the detected signal.

MPPCs which satisfy the demand (Table.3.3.3) of T2K near-detectors have been developed. The spec of developed MPPC[9] is listed in Table.3.3.4. These MPPCs are connected to WLS fibers by GOMI connectors as shown in Fig.3.3.7.

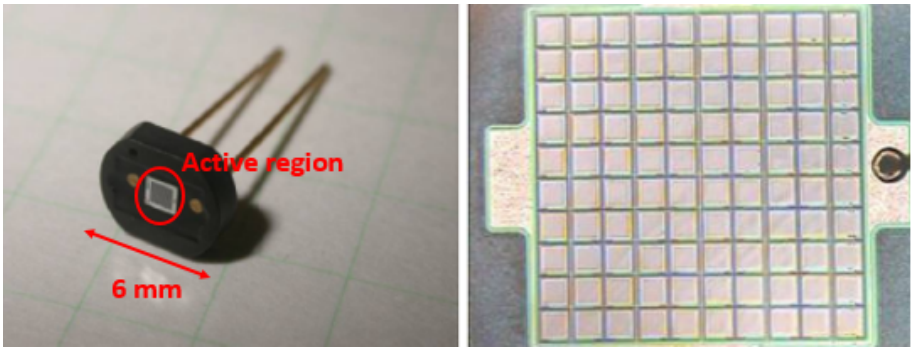

Figure 3.3.6: MPPC : The right figure shows pixels of MPPC.

These components are set in the tracking plane, as shown in Fig.3.3.8. The number of channels of 1 tracking plane is 48 and 11 planes are attached to 1 INGRID module, and the number of modules are 14, so the total channels of INGRID is $48 \times 11 \times 14 = 7392$. The readout electronics has co-axial cables and they are connected by PCB (Printed Current Board) connectors (Fig.3.3.9).

3.3.3 Veto planes

[9]The serial number of this MPPC is S10362-13-050C.

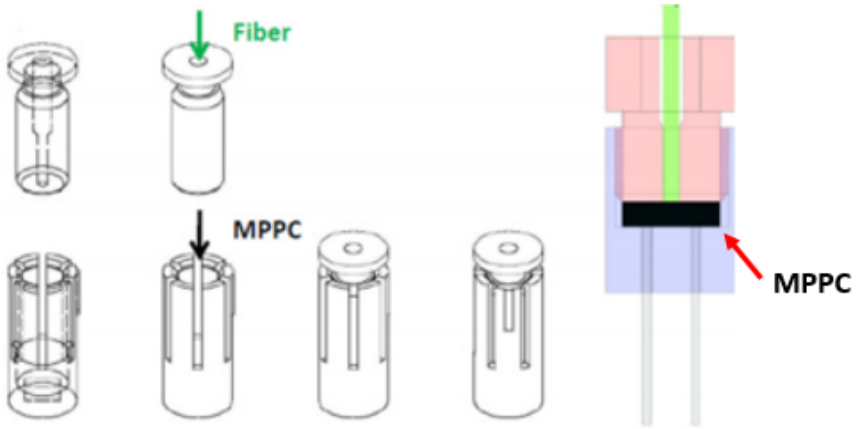

Figure 3.3.7: Illustration for how to connect MPPC with the WLS fiber

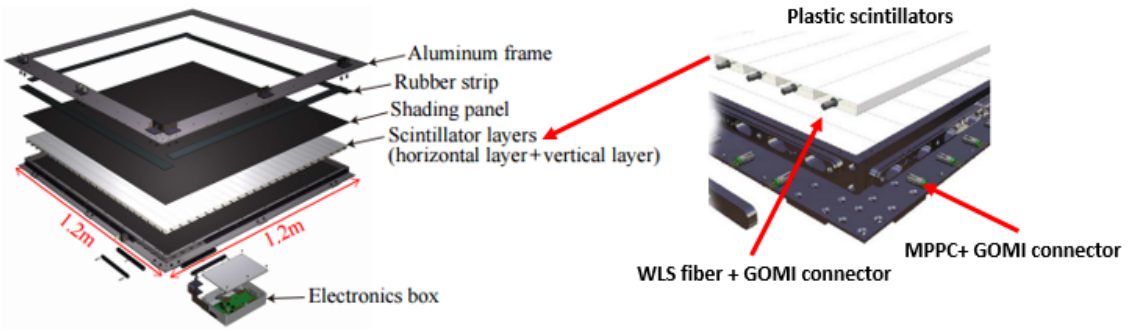

Figure 3.3.8: Exploded view of the tracking plane

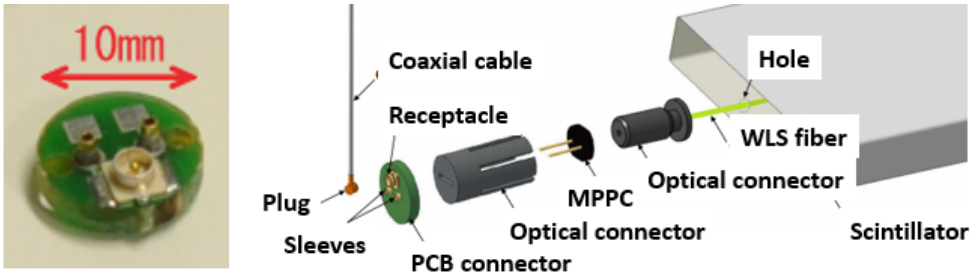

Figure 3.3.9: PCB connector

Veto planes are used for rejecting background events from the outside of the detector, for example cosmic-rays or charged particles from the neutrino interactions in the wall of the near-detector hall. They are set on the right, left, upstream, and downstream side of each INGRID module. The design of these planes are almost same as that of tracking planes, but they have only 1 scintillator layer and each layer consists of 22 scintillators[10]. In order to detect the position of charged particles, these scintillators are segmented along the beam direction. The plane between each module is in common, so the total number of planes are 44[11] and the total number of channels is $22 \times 44 = 968$. Then, the number of readout channels in INGRID is $7392 + 1144 = 8360$.

3.4 Data acquisition system

The electronics of the data acquisition (DAQ) system and the trigger for DAQ are explained in this section.

3.4.1 Electronics

DAQ system was developed by several institutes including Rutherford Appleton Laboratory, Imperial College London, and University of Oxford. Readout electronics is divided to two types : Front End Board (FEB) and Back End Board (BEB), as shown in Fig.3.4.1.

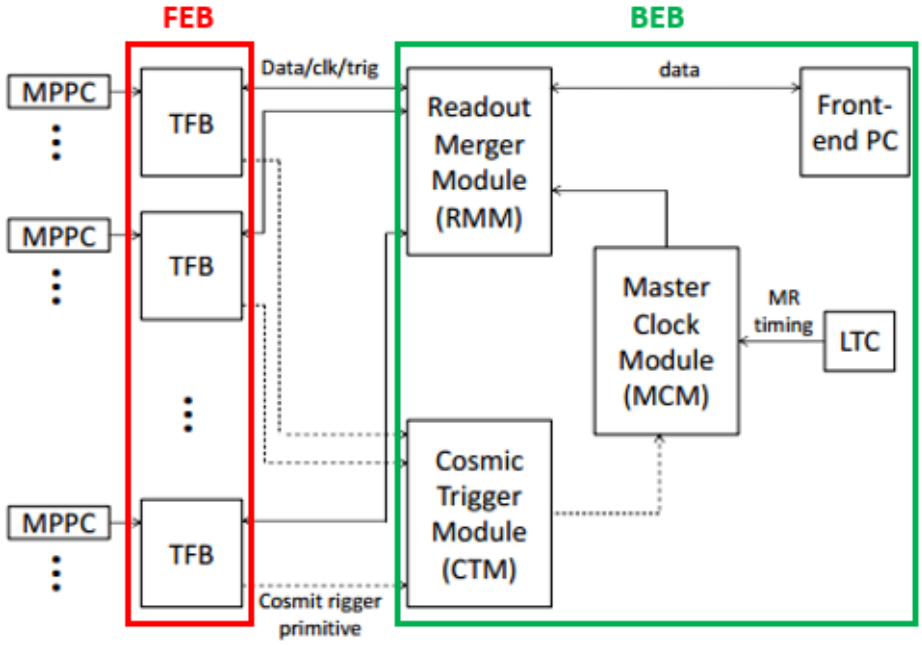

Figure 3.4.1: Overview of the electronics of INGRID

[10] The length of scintillators for the bottom side plane is 1119 mm, and that of other scintillators is 1299 mm.

[11] For horizontal modules, the number of side planes is 8 and that of top and bottom planes is 14 (7×2). For vertical modules, the number of side planes is 14 (7×2) and that of top and bottom planes is 8.

Table 3.4.1: The spec of TFB

	Designed value
Number of readout channels	64
ADC dynamic range	0~1000 p.e.
ADC noise level	< 0.21 p.e.
ADC non-linearity	< 5%
TDC resolution	2.5 ns
DAC range	0~5 V
DAC resolution	20 mV

- **FEB**

TFBs[12] (Fig.3.4.2) in FEB can readout a maximum of 64 MPPCs by using 4 ASIC chips (Trip-t chips). TFBs and MPPCs are connected by co-axial cables. The TFB also has 10-bit dual channel ADCs, 8 channel 8-bit DACs, FPGA, and so on. ADCs and TDCs are used to digitize the electron charge and the hit timing, respectively. DACs are used to calibrate the applied voltage to the MPPC channel-by-channel because each MPPC has different breakdown voltage. TFBs are controlled by the FPGA (Field Programmable Gate Arrays). The spec of the TFB is listed on Table3.4.1. TFBs are connected with BEB by STP (Shielded Twisted Pair) cables.

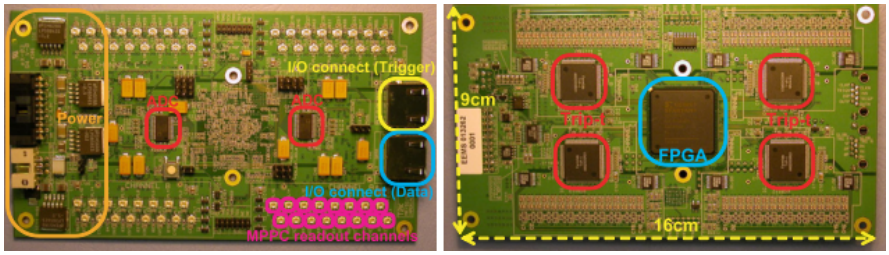

Figure 3.4.2: TFB : The right figure shows the top side and the left figure shows the bottom side

- **BEB**

BEB (Fig.3.4.3) has mainly 3 modules : Readout Merger Module (RMM), Cosmic Trigger Module (CTM), and Master Clock Module (MCM).

- **RMM**

RMMs send to the DAQ PC the merged data which is read by TFBs. Moreover, they provide TFBs with trigger signals, clock signals, and control signals. As to INGRID, 182 TFBs are controlled by 4 RMMs.

- **CTM**

CTMs generate the cosmic trigger from the hit information by TFBs, and send the trigger to MCMs.

[12]Trip-t Front end Board : Trip-t chip was developed by Fermilab.

- **MCM**

  MCMs get the information of the beam spill trigger from the beam line DAQ and that of the cosmic trigger from CTMs. Then, they send these trigger information to TFBs through RMMs.

The boards of RMMs, CTMs, and MCMs have the same structure, so they can replace each other by rewriting the firmware data of FPGA.

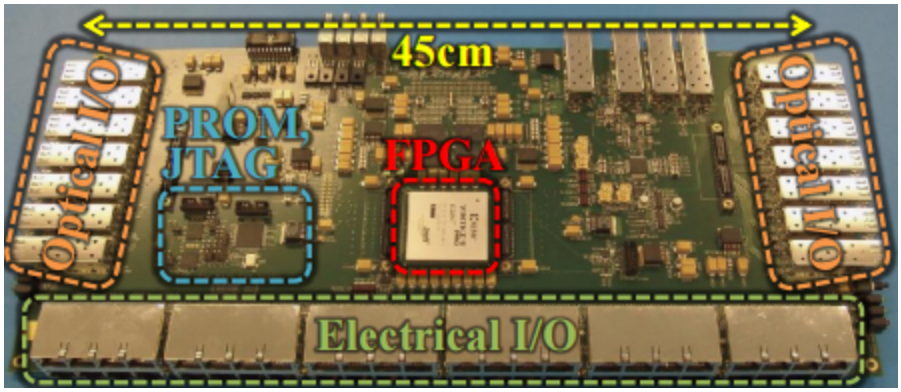

Figure 3.4.3: BEB

3.4.2 Trigger

There are 3 trigger modes for the data acquisition and we can take data with multitriggers by combining them.

- **Beam trigger**

  This trigger is for taking the beam data and is provided from the beam line DAQ.

- **Cosmic trigger**

  This trigger is for taking the cosmic data and is generated by CTMs from the hit information in TFBs.

- **Periodic trigger**

  This trigger is generated periodically and used for the calibration of the MPPC gain with the noise signal.

When the beam trigger is received by TFBs, the INGRID DAQ system starts taking data for 23 integration cycles, as shown in Fig.3.4.4. After taking 23 cycles data, the data is transported to BEBs. The time window of the reset is 50 ns, and this is the dead time. The beam-related events are not observed in the

first to the forth and the thirteenth to the twenty third cycles, and these cycles are used for studies of the accidental cosmic-ray backgrounds and MPPC dark counts.

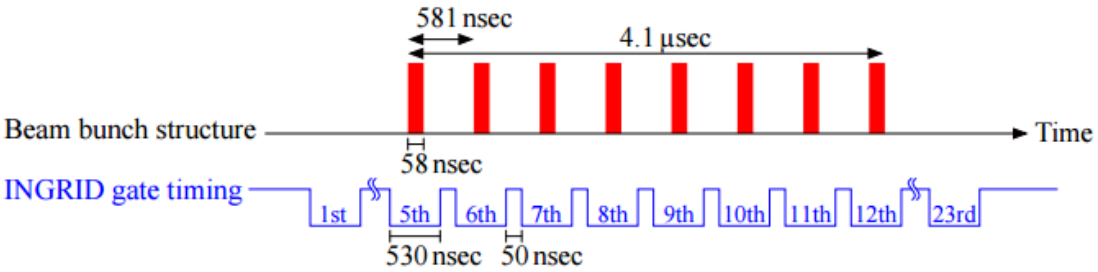

Figure 3.4.4: Image of data acquisition

Chapter 4

Analysis method of INGRID

4.1 MC simulation

The neutrino events in INGRID are predicted by a Monte Carlo (MC) simulation in following steps : the neutrino beam simulation, neutrino interaction simulation, and detector response simulation, as shown in Fig.4.1.1.

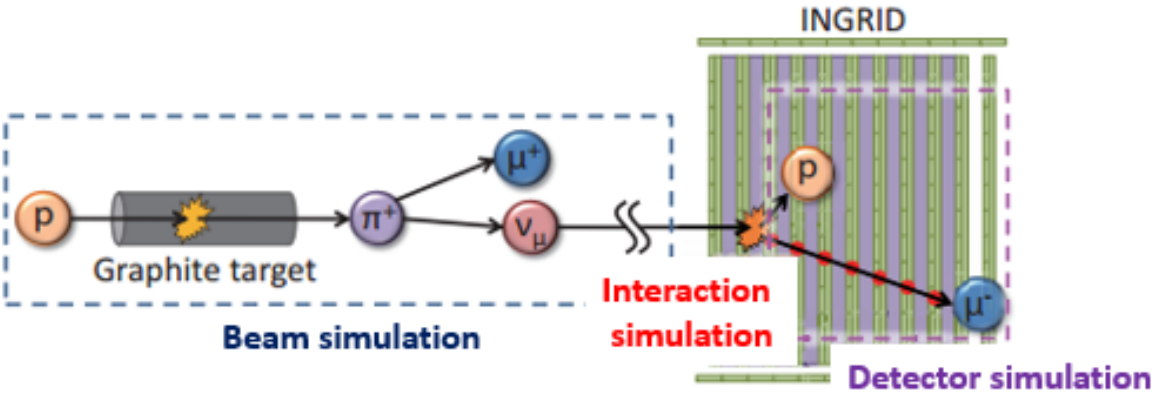

Figure 4.1.1: Overview of the Monte Carlo simulation

4.1.1 Beam simulation : JNUBEAM

JNUBEAM is the program for simulating the process of producing the neutrino beam, and is based on GEANT3. The information of the flux, energy spectrum, flavor of neutrinos, and so on can be obtained from this program. In JNUBEAM, at first the proton beam is injected to the graphite target and hadrons are produced. This process is simulated by the simulation program of the hadron production, named FLUKA[1]. Produced hadrons are focused by electromagnetic horns to the direction of SK, and hadrons decay to neutrinos in the decay volume. The simulation method after decaying to neutrinos is different between near-detectors and SK. As to the simulation of the neutrino flux in near-detectors, neutrinos are produced isotropically. These neutrinos are extrapolated to near-detectors, so neutrinos only which pass through detectors

[1]For particles which interact with something outside of the target, another program GCALOR is used.

are selected. On the other hand, in the SK case, neutrinos are always produced in the direction of SK. The probability of such decay case are calculated and that value is used as the weight of each event. In this method, all second particles are used for the calculation of the neutrino flux, so it is very efficient for the simulation. Moreover, the neutrino flux is tuned by the data of other experiments (NA61/SHINE[28], and so on).

4.1.2 Interaction simulation : NEUT

In the simulation of the interaction in INGRID, NEUT is used to simulate neutrino-nucleus interactions[2]. Neutrino interaction modes and the energy, momentum, position of second particles are added to JNUBEAM and NEUT files are generated. Neutrino interactions, in the 100 MeV to 100 TeV energy range, with nuclear targets such as protons, oxygen, carbon, and iron are simulated. INGRID has both iron planes and plastic scintillators as neutrino beam targets, but in NEUT, only iron is used as the target of the interaction simulation because iron mass occupies 95% of the INGRID mass. The vertex along the beam axis is uniformly generated both in iron planes and in scintillator trackers taking into account the mass ratio.

4.1.3 Detector response simulation : GEANT4

GEANT 4 is developed at CERN to simulate interactions and behaviors of particles in some material, and the simulation for INGRID is developed on the basis of GEANT 4. It enables us to model real INGRID structures and the geometry of the detector hall where INGRID is located, as shown in Fig.4.1.2. This simulation program reads the information of second particles from NEUT files, and simulates their interactions with the detector. Moreover, it can also simulate the light emission of scintillators and light detection of MPPC. Scintillators used in INGRID are painted with the reflective coating, so the shape of sides of them where there is the fiber inserting hole is not the complete rectangular. These region is not active, so it causes the inefficiency in the particle detection efficiency. Then, in order to reflect this effect, the scintillator shape is defined as shown in Fig.4.1.3. In this program, several physics lists are prepared to simulate a variety of hadron interactions[29]. Changing the physics list, different interactions of hadrons and nuclei for a certain energy region can be simulated.

4.2 Event reconstruction

After doing the MC simulation, events are shown only as the point which indicates the interaction vertex. So, it is necessary to draw tracks by connecting points to reconstruct charged particle events generated

[2]NEUT was originally developed to estimate neutrino backgrounds for the proton decay search in Kamiokande.

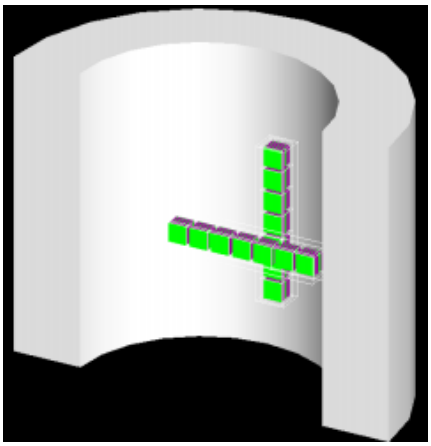

Figure 4.1.2: INGRID and the wall of the detector hall in GEANT4

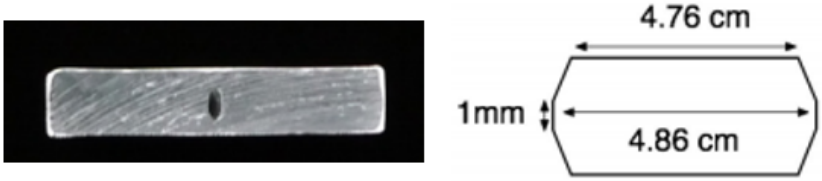

Figure 4.1.3: Sectioned picture and illustration of scintillator

by neutrino interactions. The event reconstruction is done by following 5 steps in sequence : the time clustering, active plane selection, two-dimensional track reconstruction, three-dimensional matching, and identification of the vertex.

4.2.1 Time clustering

In INGRID, one hit is recorded when more than 2.5 p.e. signals are outputted from MPPCs. In order to remove the effect of the dark noise of MPPCs, additional time clustering is needed. In case there are more than 5 hits in each INGRID module within 100 ns, all hits of events within ± 50 nsec from the average time are classified into a cluster.

4.2.2 Active plane selection

The active plane is defined as the tracking plane which has 1 or more hits both in the X layer and Y layer[3]. In order to remove background active planes by the random noise of MPPCs, events which have more than 2 active planes are selected.

4.2.3 Two-dimensional track reconstruction

[3]As described in Sec.3.3.2, each tracking plane has two types of layers : X layer is set along the direction corresponding to the X-axis and Y layer along the direction corresponding to the Y-axis.

The track reconstruction is done in the side view and the top view (Fig.4.2.1) independently. At first, for each tracking plane, adjacent hits are organized as a hit cluster, as shown in Fig.4.2.2. This is because the track at an angle for the beam axis has the possibility to hit adjacent scintillators in the same tracking plane, and we would like to treat it as a single hit. The cluster which is in the most downstream tracking plane is defined as a starting point. From the starting point, clusters are selected by tracking back to the upstream clusters layer by layer. In that process, the linear least square fit is applied to 3 neighboring clusters and $\chi^2 < 1.5$ is required. If there is no hit on the upstream plane, the selection of clusters are complete. Then, for selected clusters, the track is drawn. The track validity is also checked by the linear least square fit. Reconstructed track are shown in Fig,4.2.3.

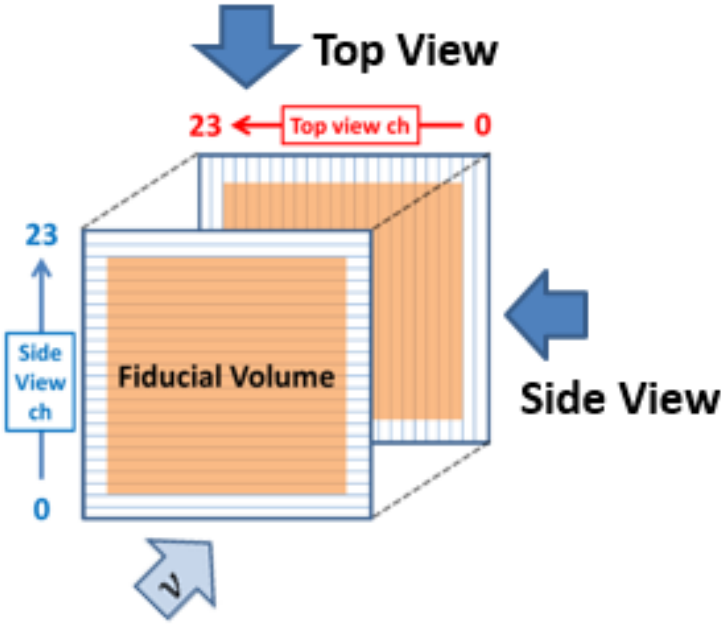

Figure 4.2.1: The illustration for the side (Y-Z) view and top (X-Z) view of INGRID : Z axis is matched with the beam direction

4.2.4 Three-dimensional track matching

After two-dimensional track reconstruction, it is necessary to check the combination of side view tracks and top view tracks. When the difference between the most upstream point of each track is smaller than 3 layers, they are combined into a three-dimensional track. If a two-dimensional track in X-Z plane (Y-Z plane) meets the above condition with more than one two-dimensional track in Y-Z plane (X-Z plane), the pair of tracks with the smallest difference of the upstream point is combined. If there is more than one pair of two-dimensional side view and top view tracks which have the same difference of the upstream point, the pair of tracks which has the smallest difference of the downstream point has a priority, and if it is also the same, the pair of tracks whose total light yield per track length is the closest has a priority.

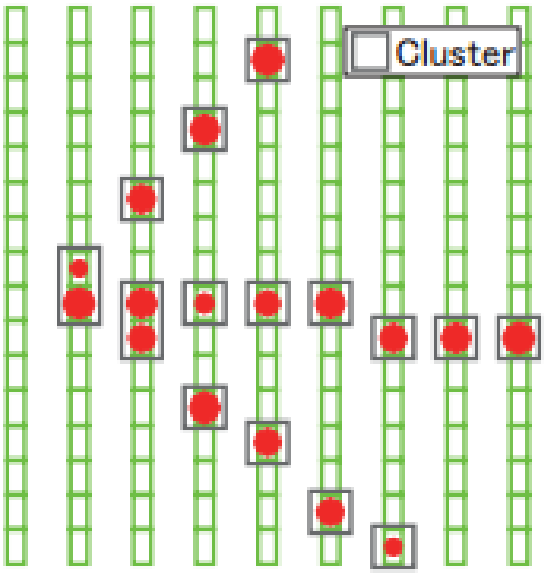

Figure 4.2.2: Hit clusters : red circles show hit points

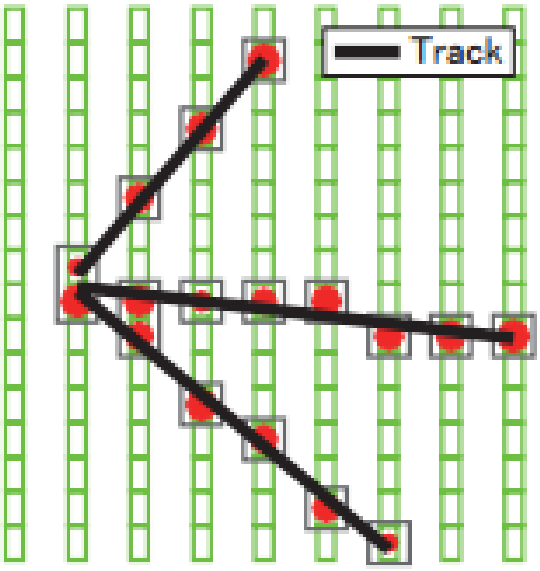

Figure 4.2.3: Reconstructed tracks

4.2.5 Identification of the vertex

Finally, the interaction vertex is searched. Basically, the most upstream point of the three-dimensional track is considered as the reconstructed vertex. If there are two tracks and meet both following conditions, they are identified as the tracks from a common vertex :

- Sum of Z position distance between the upstream edges of the two tracks in the side view and top view is zero or one plane

$$|\Delta Z_X| + |\Delta Z_Y| \leq 1\ (plane), \tag{4.2.1}$$

  where ΔZ_X and ΔZ_Y are Z position distance between the upstream edge of two tracks in the side view and top view.

- Distance between the upstream edges of two tracks in XY-plane is less than 150 mm

$$\sqrt{(\Delta X)^2 + (\Delta Y)^2} < 150\ mm, \tag{4.2.2}$$

  where ΔX and ΔY are the X and Y position between the upstream edge of two tracks.

If a pair of tracks are identified as the tracks from a common vertex, the upstream edge of the longer track is identified as the reconstructed vertex. If they have the equal track length, track whose number of photoelectrons per length is larger is adopted. This vertex identification is done for every combination of all reconstructed three-dimensional tracks. So even if there are more than two tracks from a vertex, they can be identified as the tracks from a common vertex.

4.3 Event selection

After the event reconstruction is complete, then the event selection is done in order to reject events caused by charged particles from outside of INGRID modules. There are 3 selections : the timing cut, veto cut, and fiducial volume cut.

4.3.1 Timing cut

In order to cut out background events such as cosmic-rays on the beam-off timing, events within ± 100 ns from the expected timing of each bunch are selected, as shown in Fig.4.3.1.

4.3.2 Veto cut

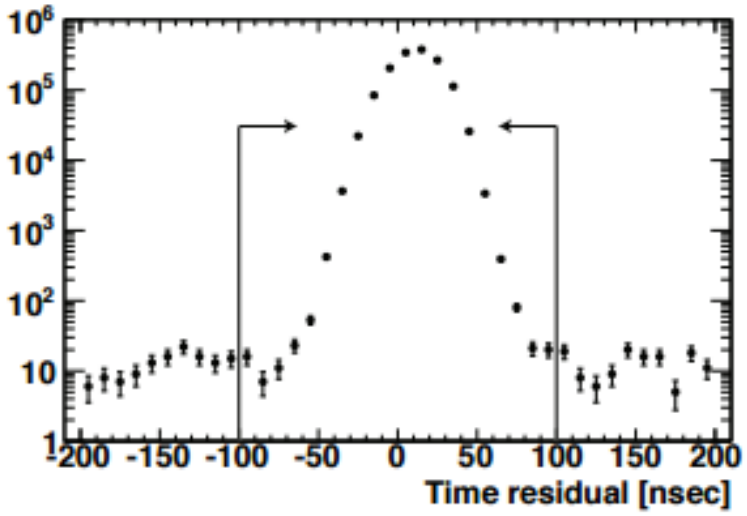

Figure 4.3.1: Time residual from the expected timing : 0 means the expected timing

The veto cut is imposed to events in order to remove those produced outside the INGRID. If there is a hit in the upstream veto plane, that event is rejected. Moreover, if there is a hit in the side veto plane and that hit is on the extended line of the reconstructed track (Fig.4.3.2), that event is also rejected. The criterion of this cut is that the difference between the hit on the side veto plane and on the extended reconstructed track is smaller than 80 mm[4].

4.3.3 Fiducial volume cut

The fiducial volume cut is imposed to events after the veto cut, and the definition of the fiducial volume is shown in Fig.4.3.3. Only vertexes in this fiducial volume is selected as events. The track reconstruction requires more than 2 active planes, so 2 tracking planes and 1 iron plane in the downstream side are not included in the fiducial volume.

4.4 Qualifications for real data

In the T2K experiment, real data which meet following qualifications are used for the analysis.

- **Physics data acquisition**

  Data are taken in the physics data acquisition period, not during the adjustment of the beam path or the DAQ test. All horns are required to be ON.

- **Beam trigger**

  Events are recorded when the beam trigger from the accelerator is on.

[4]If that difference is larger, the hit on the veto plane could be the accidental hit due to MPPC noises.

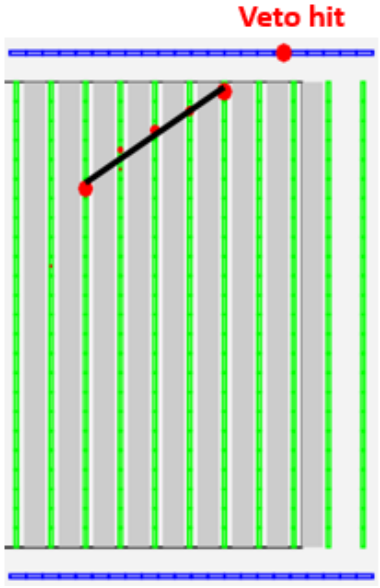

Figure 4.3.2: Event display of INGRID MC : Blue regions show side veto planes, and there is a hit on one of veto planes.

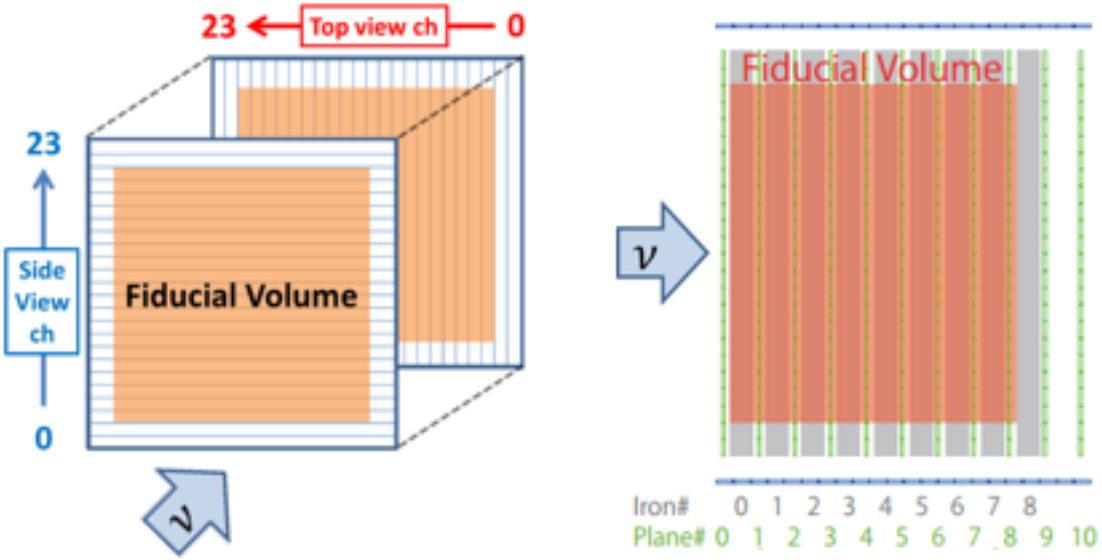

Figure 4.3.3: Definition of the fiducial volume : The left figure shows the fiducial volume of each tracking plane ($(\pm 50) \times (\pm 50)$ cm^2), and the right figure shows the fiducial volume along the beam axis (iron# 0-7, tracking plane# 1-8).

- **Good GPS status**

  There are 2 GPSs both in J-PARC and SK to check the beam timing, so they enable us to calculate the timing in two ways. If the residual of timings which are recorded in these GPSs is smaller than 200 ns, GPSs behave properly.

- **Number of protons**

  The number of protons are monitored by CT, as mentioned in Sec.2.2.2, and CT5 is placed most nearby the proton beam target. More than 10^{11} protons/spill observed at CT5 is required. Just after the MPS and PPS[5] in J-PARC is fired, there is the possibility that there is no beam even if the beam trigger from the accelerator is on. This qualification is needed to avoid such kind of events.

- **Normal condition**

  If there are some problems, recorded events are rejected.

- **Current of horns**

  The fluctuation of current from setting values of 3 electromagnetic horns should be within 2%. The uncertainty of the neutrino flux in the energy of 0.5-0.7 GeV[6] is permitted within 2% in the T2K experiment, so the current fluctuation is required to be smaller than the flux uncertainty.

- **MUMON cut**

  The fluctuation of the beam direction along the X-axis and Y-axis should be within 1 mrad, and that of the muon yield observed in silicon PIN photo-diodes are 5%. The 5% fluctuation is much larger than the resolution of MUMON, so if the fluctuation is more than 5%, there could be some troubles.

Data which satisfy these qualifications are called Good spill data.

[5] MPS : Machine Protection System, to protect equipment from beam-induced damage by stopping the beam immediately
PPS : Personal Protection System, to protect persons from any hazards due to beam

[6] In this energy region, the probability of the neutrino oscillation is maximized, as mentioned in Sec.1.2.2

Chapter 5

Measurements for neutrino interactions at an off-axis angle 1.6 degrees

5.1 Motivation

INGRID detector is monitoring the neutrino beam, and it is essential to understand the neutrino interaction cross section in iron. However, INGRID mainly measures neutrinos for more than 1 GeV neutrino interactions, so there is little data for sub-GeV (< 1 GeV) region. That is why as mentioned in Sec.3.2, one of INGRID modules is moved to the the B2 floor in the detector hall, as shown in Fig.5.1.1, in order to study neutrino interactions at sub-GeV regions[30]. The off-axis angle at the B2 module position is about 1.6 degrees[1], so the neutrino flux has lower energy than the on-axis position, as shown in Fig.5.1.2. Moreover, we are planning to locate a new neutrino detector at the B2 floor, as described in Chapter 6, so we can estimate neutrino interactions at the candidate position in advance. In this chapter, the comparison between neutrino events in the real data and in the MC simulation data at the B2 floor is mainly described.

5.2 Data set

5.2.1 Real data

For the real data, 3 periods in the $\bar{\nu}_\mu$ mode (Table.5.2.1) are used. The total POT is 1.81×10^{20}. Fig.5.2.1 shows event rates during this period at the INGRID center module, bottom module, and the B2 module.

Table 5.2.1: Period of real data

	Period	Integrated POT
①	Jun. 4, 2014 - Jun. 24, 2014	5.09×10^{19}
②	Oct. 30, 2014 - Nov. 25, 2014	5.38×10^{19}
③	Nov. 29, 2014 - Dec. 22, 2014	7.61×10^{19}

[1] This is the maximum off-axis angle in INGRID modules.

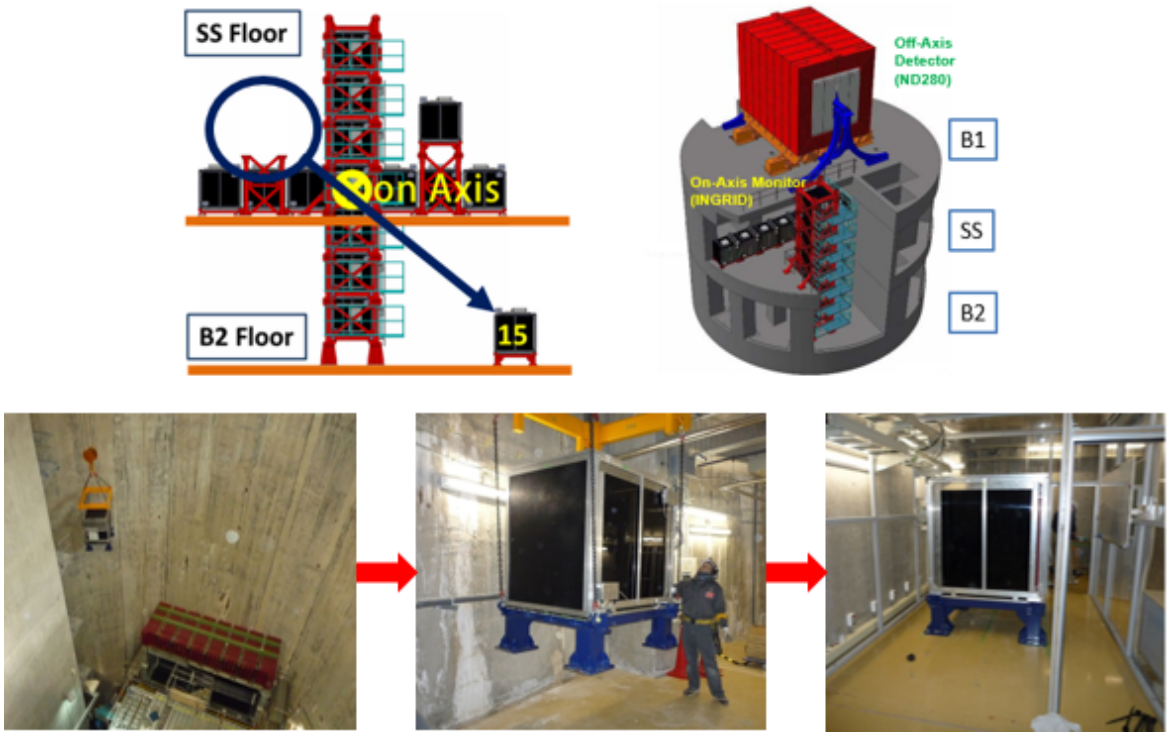

Figure 5.1.1: Overview of the the B2 module : Pictures show the movement work on Mar. 2011.

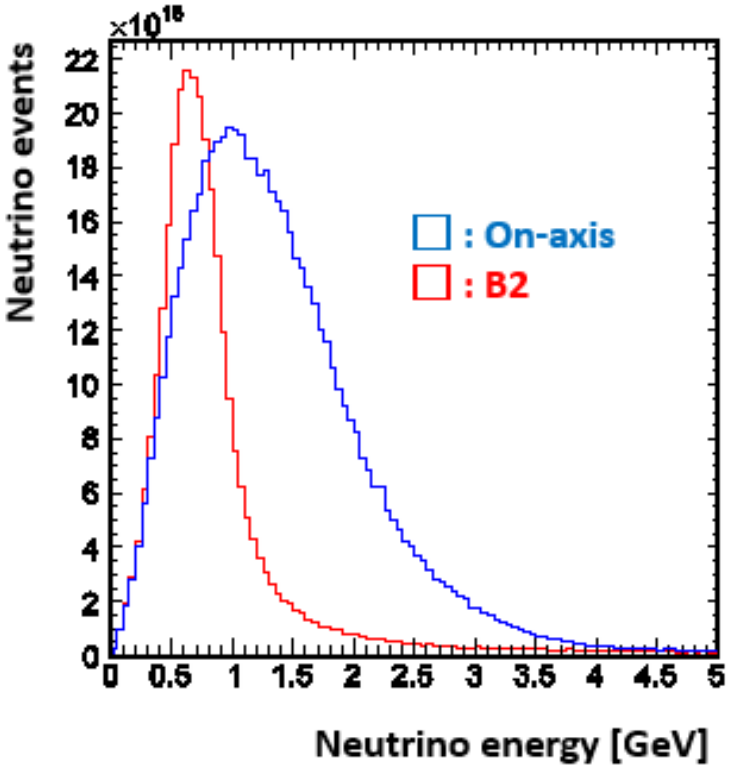

Figure 5.1.2: Neutrino flux at the on-axis and the B2 module position

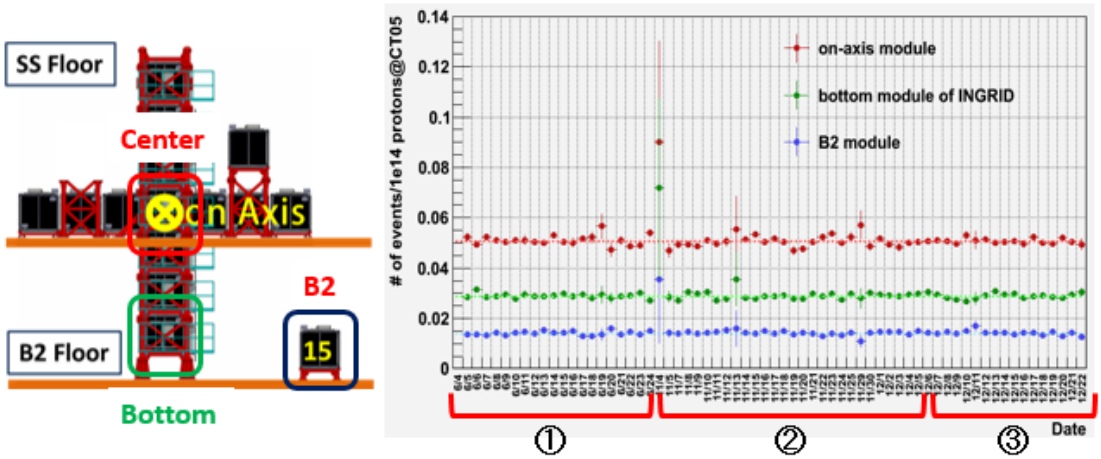

Figure 5.2.1: Event rate : Although the error bar is relatively large at the begging of each period due to the shortage of statistics, the event rate is very stale within the error range during 3 periods.

5.2.2 Data in the MC simulation

For the neutrino beam simulation, neutrino interaction simulation, and detector response simulation, programs listed on Table.5.2.2 are used.

Table 5.2.2: Program versions in the MC simulation : JNUBEAM version 13a is only used for the wall background events

Simulation type	Program	Version
Neutrino beam	JNUBEAM	11b ver.3.2, 13a ver 1.1
Neutrino interaction	NEUT	5.1.4.2
Detector response	GEANT4	v9r2p01n00, Physics list : QGSP_BERT

$\bar{\nu}_\mu$ flux at the B2 module generated by these programs is shown in Fig.5.2.2. The ratio of $\bar{\nu}_\mu$ and ν_μ in the injected neutrino beam is 92% : 8%, and that of $\bar{\nu}_\mu$ and ν_μ which interact in the B2 module is 64% : 36%. The interaction cross section of ν_μ is larger than that of $\bar{\nu}_\mu$, so the ν_μ occupies a relatively large ratio in the latter case.

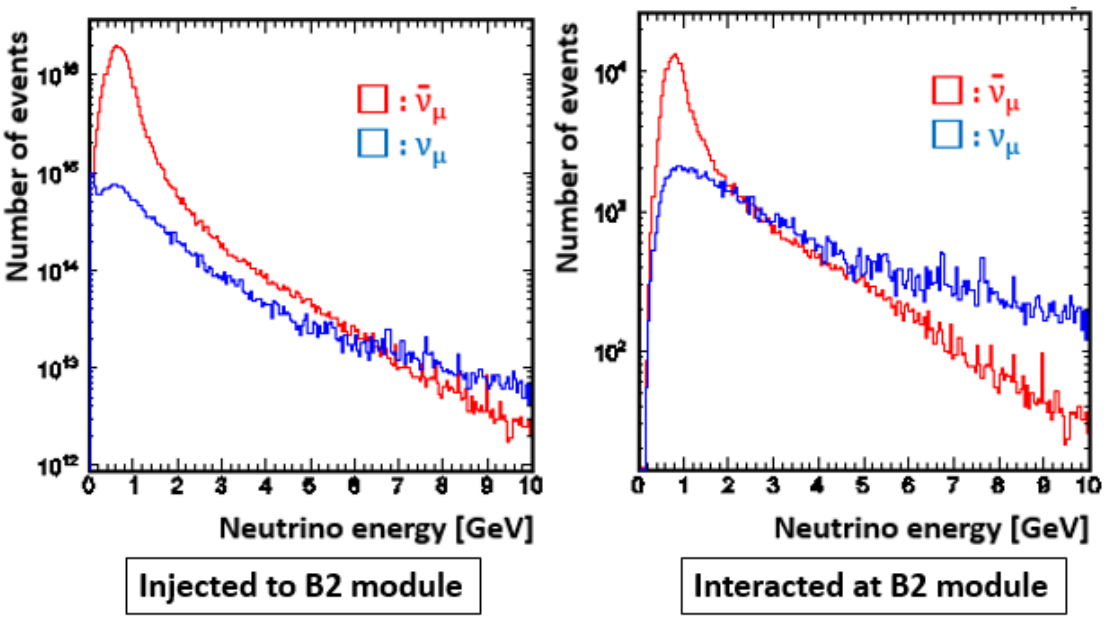

Figure 5.2.2: Neutrino flux generated in the MC simulation

5.3 Background source

5.3.1 Overview

The detector hall from the top view is shown in Fig.5.3.1, and the yellow box indicates the B2 module. The coordinates of the center of the B2 module is (X, Y, Z) = (-623.9 cm, -481.9 cm, 233.5 cm). There are background sources around the B2 module, such as wall or pillars, and in the detector simulation these sources are taken into account of. The top view of the position of these sources are shown in Fig.5.3.2. In

addition, the ceiling and floor at the B2 floor is also taken into consideration. The relative position relation between the detector and them are shown in Fig.5.3.3.

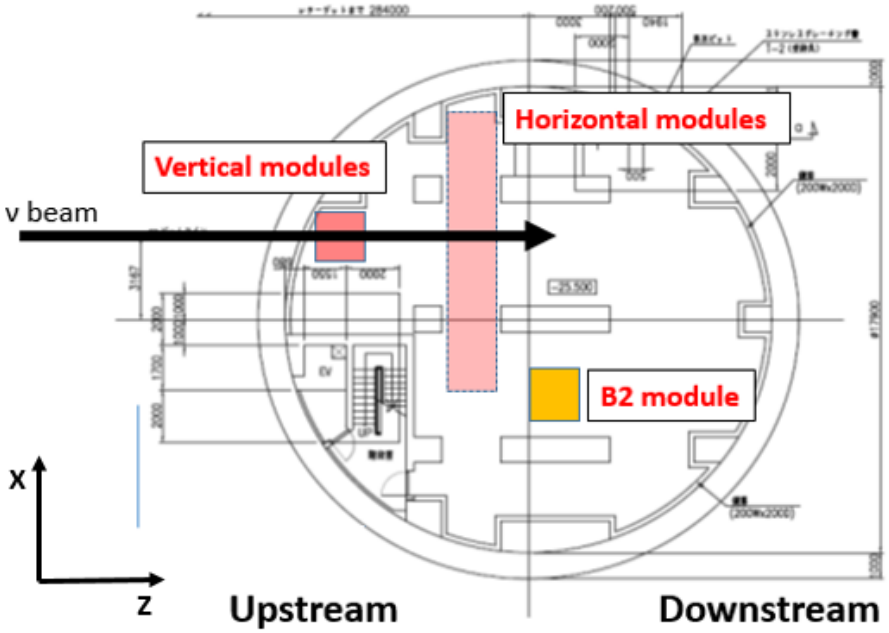

Figure 5.3.1: Top view of the detector hall

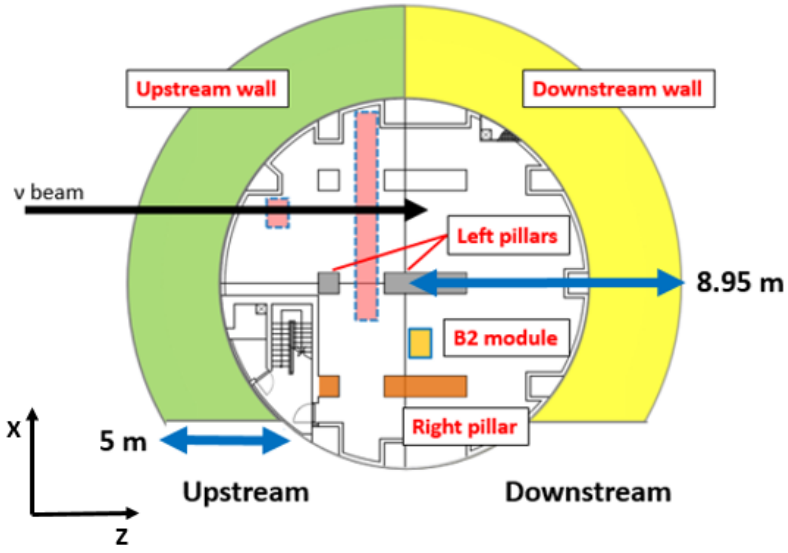

Figure 5.3.2: Top view of the background sources

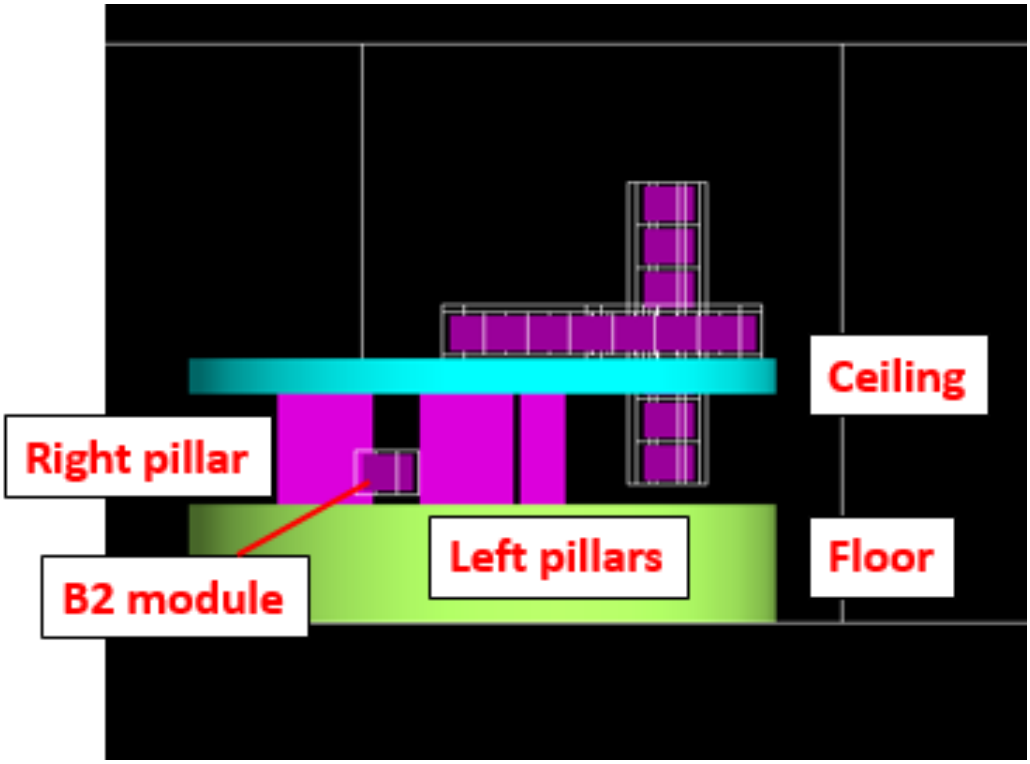

Figure 5.3.3: Background sources in the detector simulation program

5.3.2 Neutrino interactions in background sources

After background sources are placed in the detector simulation program, it is necessary to confirm that neutrinos are properly interacted with nucleus in these sources. Background sources are as follows :

1. **Upstream wall** (Fig.5.3.4)
2. **Downstream wall** (Fig.5.3.5)
3. **Left pillars** (Fig.5.3.6)
4. **Right pillar** (Fig.5.3.7)
5. **Ceiling** (Fig.5.3.8)
6. **Floor** (Fig.5.3.9)

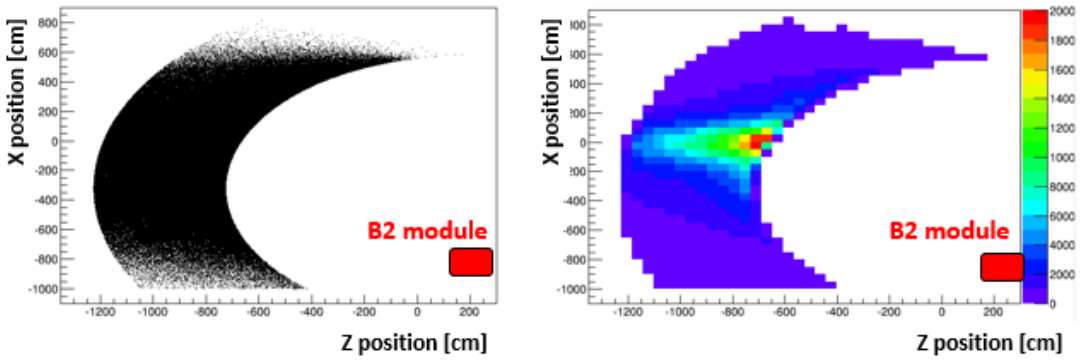

Figure 5.3.4: Neutrino interaction vertex in the upstream wall

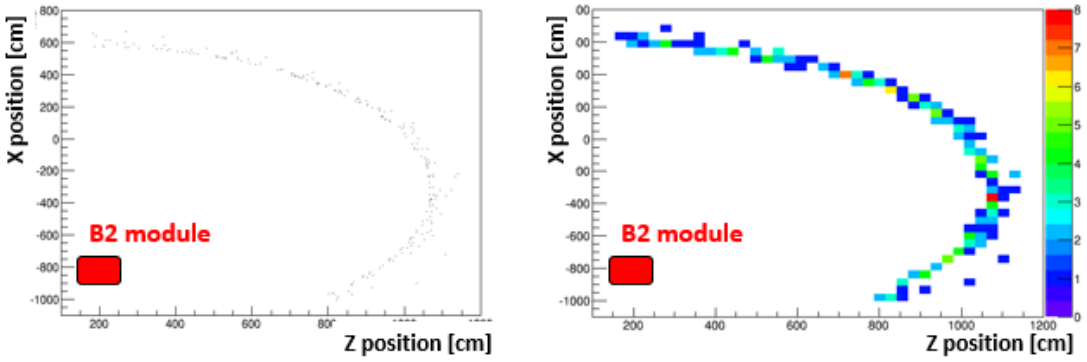

Figure 5.3.5: Neutrino interaction vertex in the downstream wall

where X position and Z position is the interaction vertex along X and Z axis, respectively.

From above figures, neutrino vertexes exist at positions where we set sources in the detector simulation

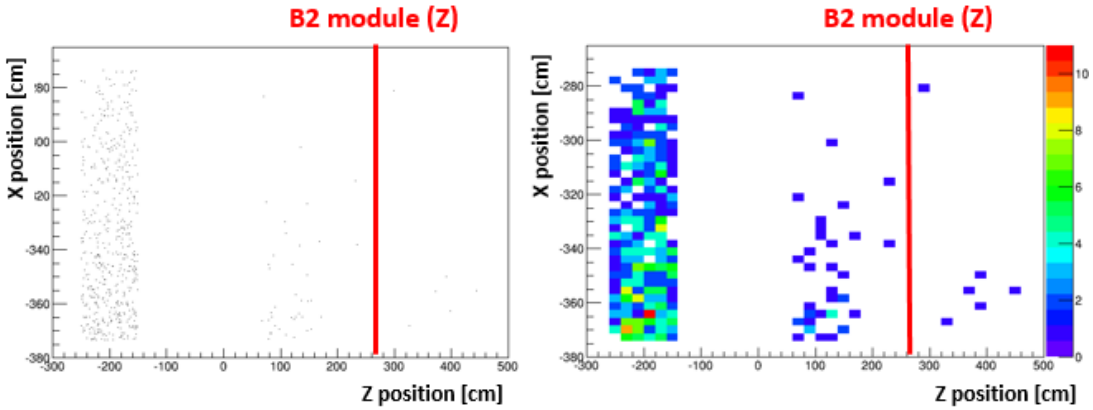

Figure 5.3.6: Neutrino interaction vertex in the left pillars

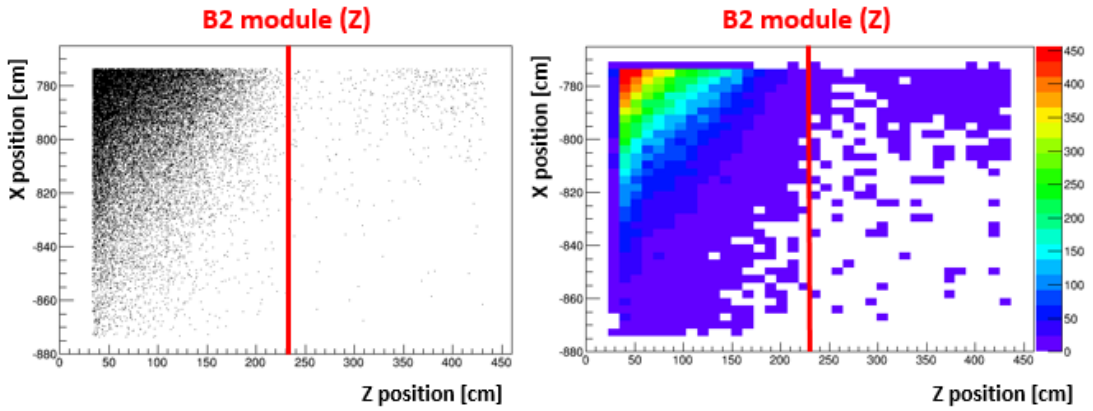

Figure 5.3.7: Neutrino interaction vertex in the right pillar

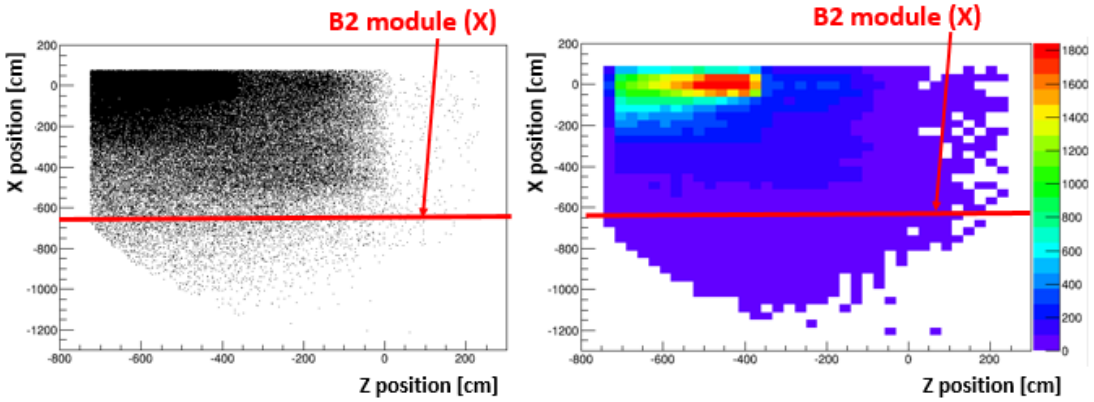

Figure 5.3.8: Neutrino interaction vertex in the ceiling

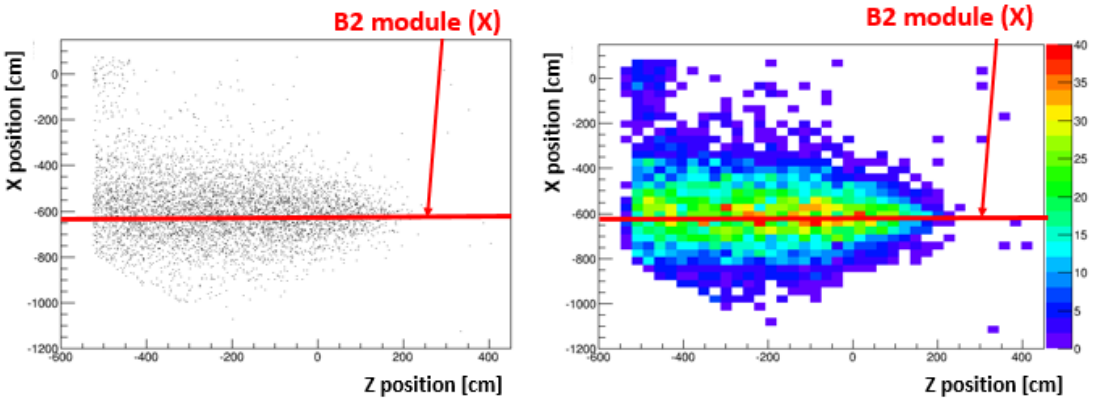

Figure 5.3.9: Neutrino interaction vertex in the floor

program. In conclusion, the generation of background neutrino events is succeeded. Moreover, Fig.5.3.5 indicates that there are few back scattering neutrino events. So, as to right side pillars, only one of them which is the most nearby the B2 module is taken into consideration.

5.3.3 Shielding effect by the ceiling

The ceiling is located between the beam axis and the B2 module, so we assume that neutrinos directing to the B2 module would be shielded by it. Fig.5.3.10 shows the neutrino flux with and without the ceiling in GEANT4, where xnu and ynu is the vertex position along the X and Y axis, respectively. This figure indicates that neutrino events produced by neutrinos from the upper side of the ceiling is decreased. So, our assumption turned out to be correct.

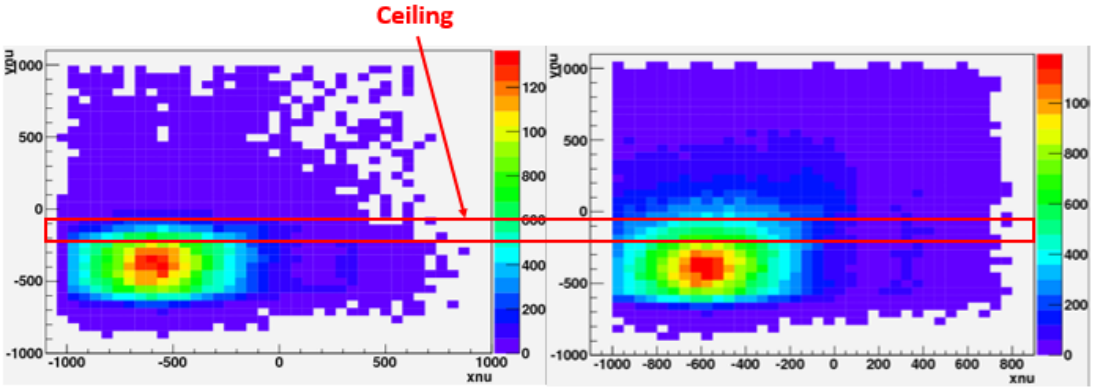

Figure 5.3.10: Neutrino flux : The left figure shows the flux with the ceiling, and the right shows without it.

5.3.4 Normalization of background events

There are other background sources around the B2 module, such as other pillars. So, when we estimate background events in the MC simulation, the normalization constant is multiplied. The constant C can be derived from Equation (5.3.1)

$$C = \frac{N^{veto}_{Real} - N^{veto}_{MC(signal)}}{N^{veto}_{MC(BG)}}, \tag{5.3.1}$$

where N^{veto}_{Real}, $N^{veto}_{MC(signal)}$, and $N^{veto}_{MC(BG)}$ are the number of charged particles that hit the veto plane in the real data, signal flux MC simulation, and background MC simulation, respectively. Veto planes are placed in front and at both sides of the B2 module, as shown in Fig,5.3.11, and tracks which leave the hit on at least one plane are taken into account. Then, let's evaluate the value of C. Table.5.3.1 shows the number of events in the veto plane. Data set is as same as Sec.5.2, so the accumulated POT is 1.81×10^{20}. From Table.5.3.1, the constant C can be calculated as follows :

$$
\begin{aligned}
C &= \frac{N^{veto}_{Real} - N^{veto}_{MC(signal)}}{N^{veto}_{MC(BG)}} \\
&= \frac{75111 - (1096.3 + 1434.7)}{49316.1} \\
&= 1.47173. \qquad (5.3.2)
\end{aligned}
$$

In the next section (Sec.5.4), this value is multiplied to the number of background events.

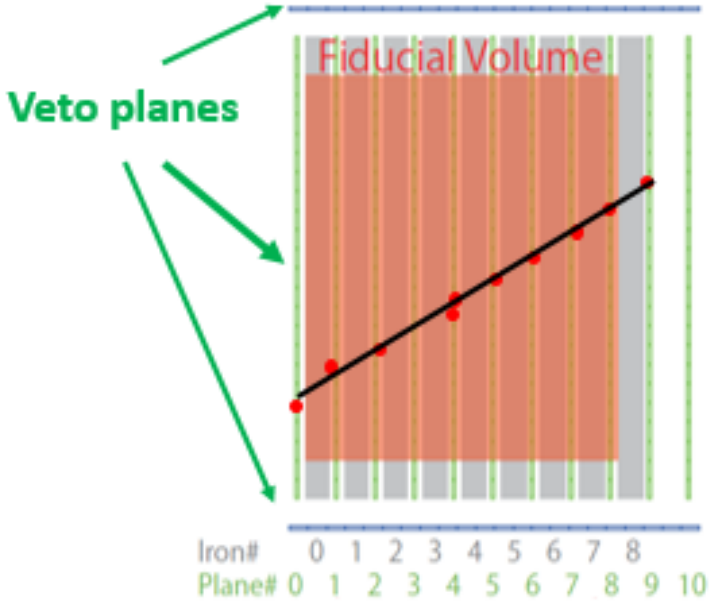

Figure 5.3.11: Veto planes surrounding the B2 module

Table 5.3.1: Number of events remain the hit on the veto plane

	Number of events
Real data	75111
All MC simulation	49316.1
$\bar{\nu}_\mu$ background simulation	1096.3
ν_μ background simulation	1434.7

5.4 Comparison between the real data and the Monte Carlo simulation

Using the B2 module, real data and simulation data are compared for reconstructed events and selected events. Conditions of event reconstruction and event selection are explained in Sec.4.2 and Sec.4.3.

5.4.1 Convention

In the following sections, there are two technical terms.

- **Vertex**

  The illustration of the inside of the B2 module is shown in Fig.5.4.1, and three types of vertex are also drawn. Vertex X and Vertex Y indicate the channel number of the scintillator in the most upstream tracking plane which has the hit. It should be noted that X layer and Y layer measure the Y coordinates and X coordinates, respectively. On the other hand, Vertex Z indicates the number of the most upstream tracking plane including the hit.

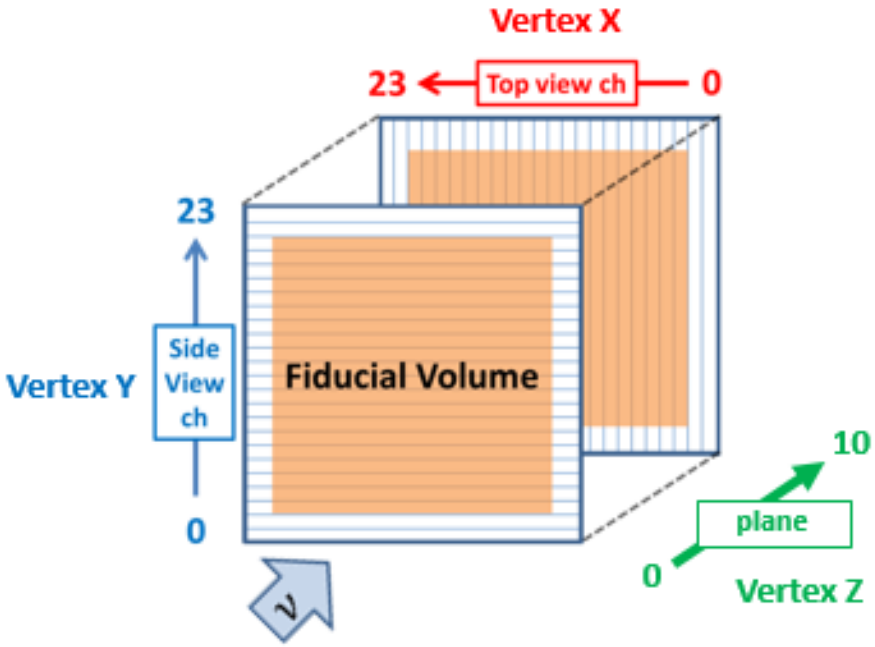

Figure 5.4.1: Illustration of inside the B2 module

- **Angle**

  Fig.5.4.2 shows 3 types of angles. As the name suggests, Top view angle and Side view angle indicates the angle from the top view and side view of the module. They are two dimensional angles. Combining the angle information of them, three-dimensional angles, named 3Drecon angle, can be displayed.

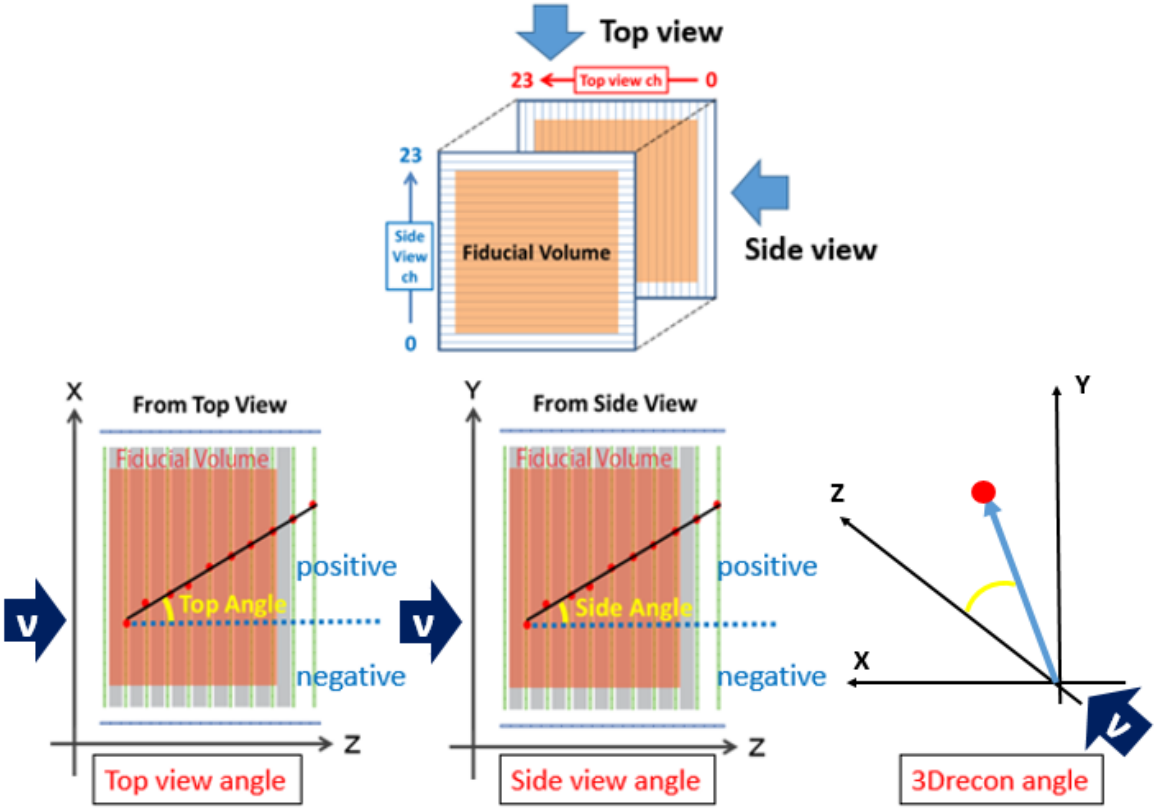

Figure 5.4.2: Overview of 3 types of angles

5.4.2 Reconstructed events

Basic distributions for reconstructed events are shown below.

- **Vertex plots**

  Plots for the vertex are shown in Fig.5.4.3, Fig.5.4.4, Fig.5.4.5. The ratio between the data and simulation is found to be within 10% from unity for each plot, but as to ch 0 and ch 23 in the Vertex X and Vertex Y plots, the difference is relatively large. For Vertex X, ch 0 and ch 23 indicate the side of the B2 module. So, the effect from the wall and pillar might not be estimated properly. Events from the wall populated more in the region nearby the beam axis, so we don't estimate them form the omitted wall shown in Fig.5.3.2. Although there are few events from that region as shown in Fig.5.4.6, it should be taken into consideration in the simulation. Pillars around the B2 module are also not fully considered in the simulation, so we should duplicate the environment at the B2 floor more precisely. For Vertex Y, ch 0 and ch 23 indicates the bottom and top of the B2 module. Fig.5.4.7 shows the events from the B2 floor, and the red square indicates the floor region in the CAD data. The floor we place in the detector simulation is a little thicker, so it could cause the overestimated result in ch 0. On the other hand, for the distribution of Vertex Z, the tendency is well matched between the data and simulation.

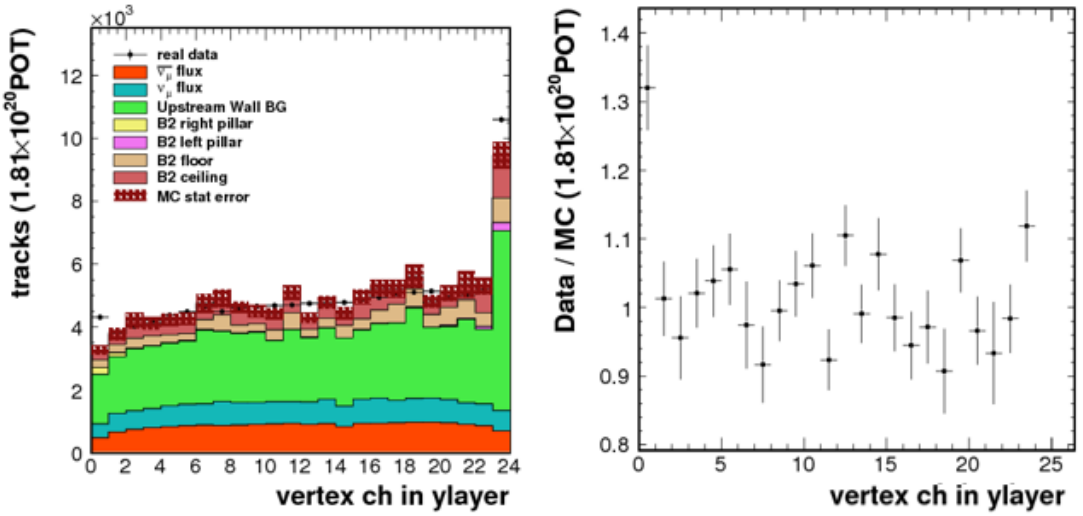

Figure 5.4.3: Basic distribution for Vertex X : The right figure shows the ratio between the data and simulation.

- **Angle plots**

  Plots for the angle are shown in Fig.5.4.8, Fig.5.4.9, Fig.5.4.10. For Top view angle, simulated events in the negative region are more than data events. It might be because the shortage of the positive region estimation. As shown in Fig.5.4.2, events with the positive angle come from the missing wall.

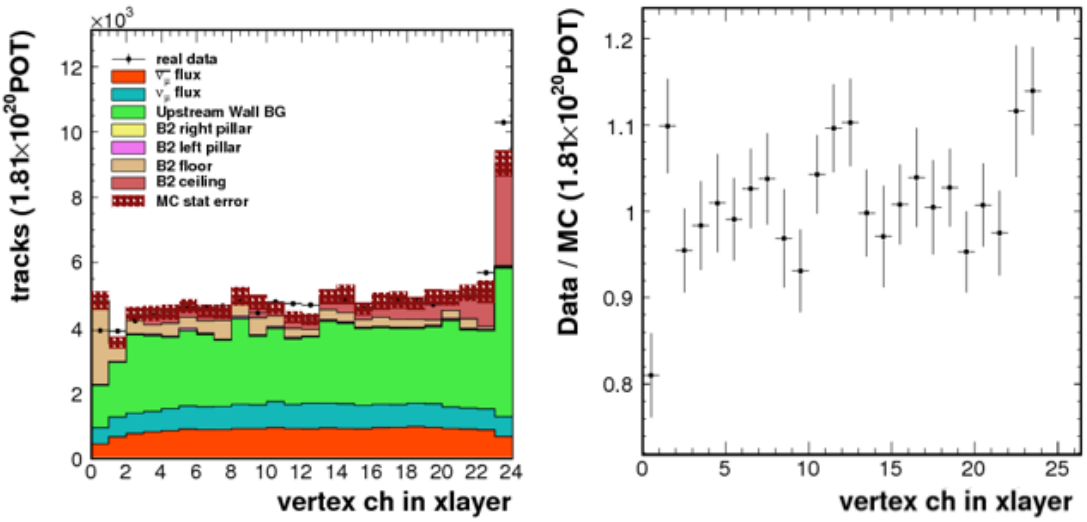

Figure 5.4.4: Basic distribution for Vertex Y and the ratio between the data and simulation

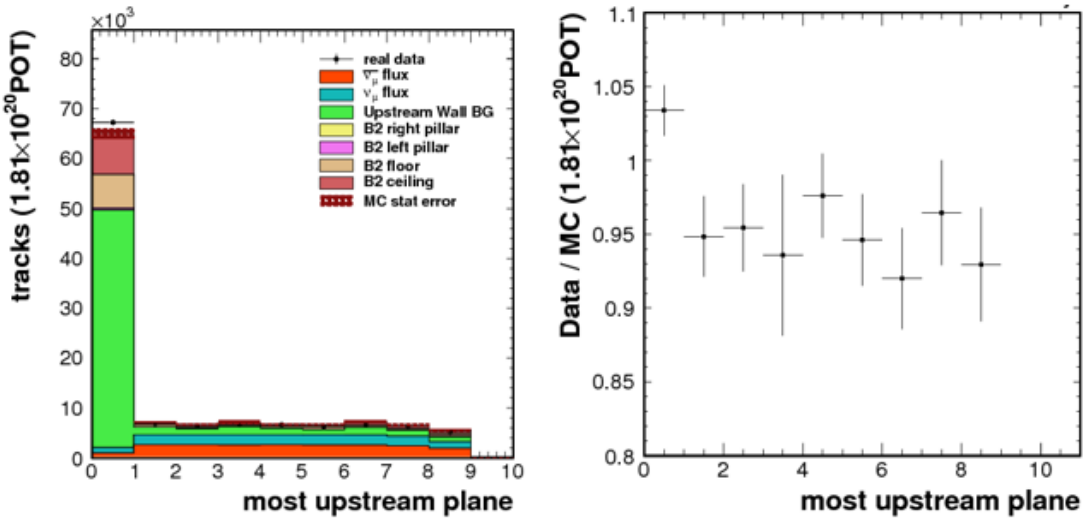

Figure 5.4.5: Basic distribution for Vertex Z and the ratio between the data and simulation

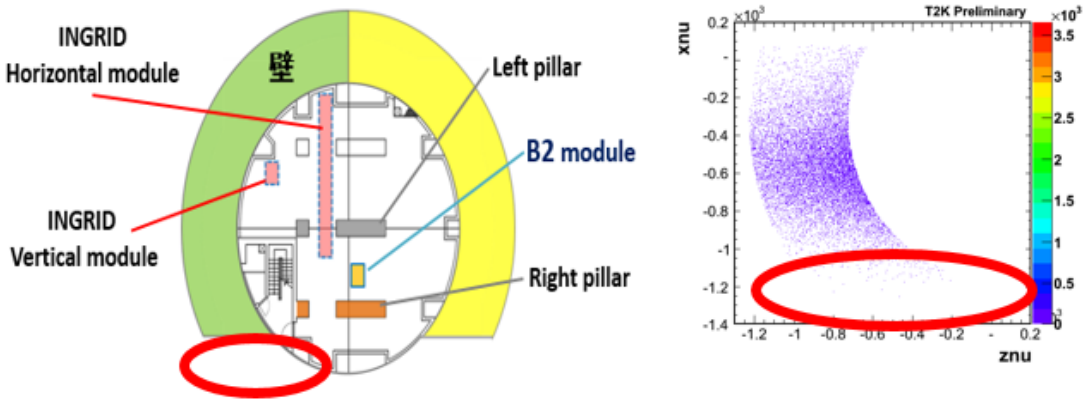

Figure 5.4.6: Events from the red circle region are very few : In the simulation, that region is omitted.

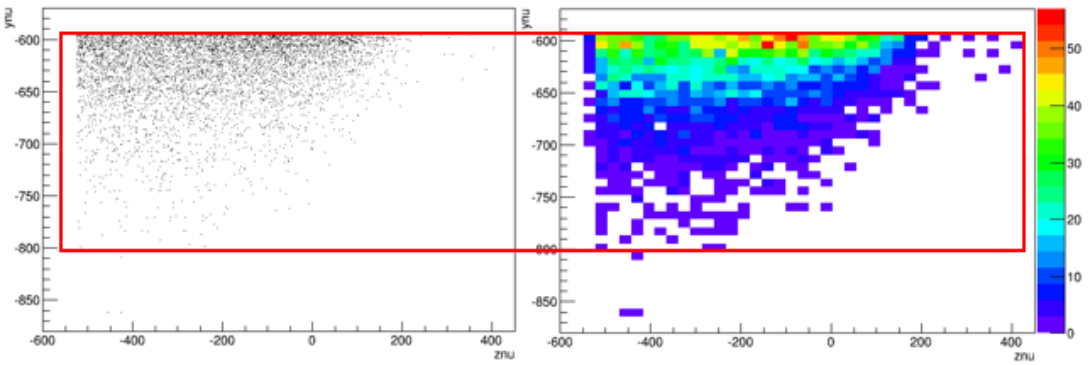

Figure 5.4.7: Events from the floor : The red square region indicates the floor.

So, the normalization constant could be overestimated. From this result, a more precisely duplication of the B2floor is important, as mentioned above. For Side view angle, more simulated events in the negative region might be due to the overestimation of events from the floor, as we discussed for the Vertex Y. It also causes the large normalization constant. In the 3Drecon angle plot, the number of events is decreased as the angle becomes large. Scintillators in the tracking plane is aligned in parallel, so it is difficult to reconstruct events which have large angle, as shown in Fig.5.4.11.

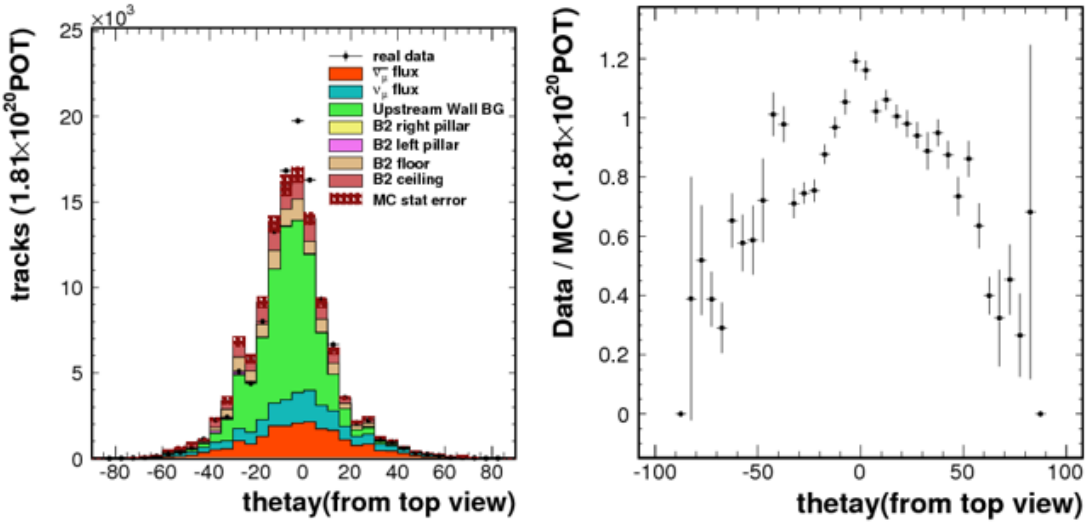

Figure 5.4.8: Angle distribution from the top view

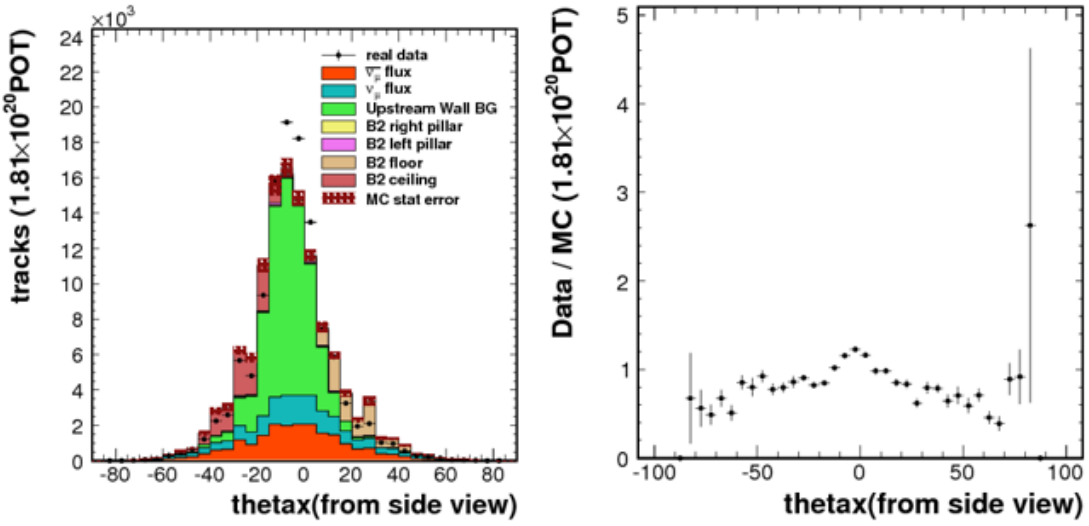

Figure 5.4.9: Angle distribution from the side view

- **Number of events**

Table.5.4.1 shows the number of reconstructed events in the simulation. The number of events in

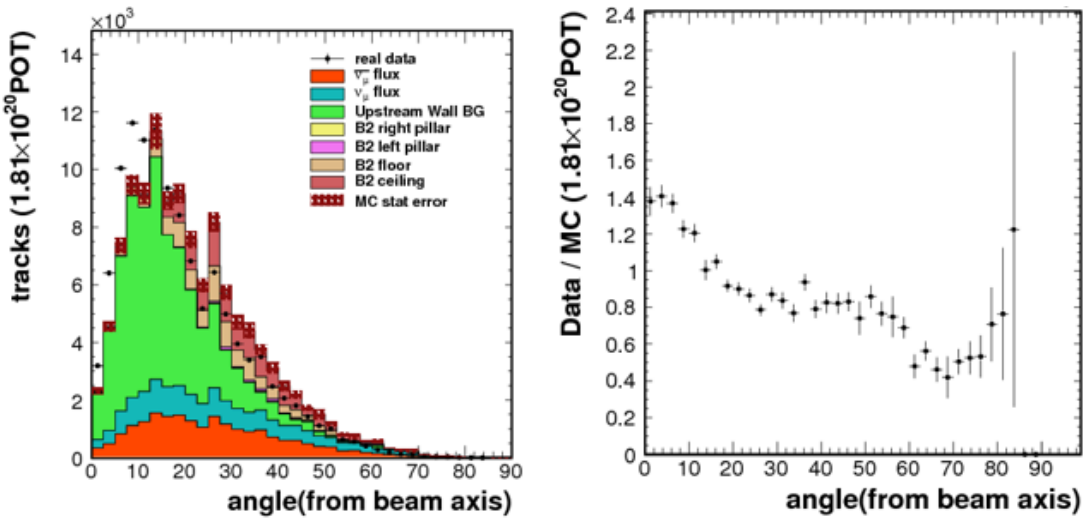

Figure 5.4.10: Three-dimensional angle distribution

Table 5.4.1: Number of reconstructed events in the MC simulation

	Number of events (Statistical error)	Ratio
Signal flux	37226.3 (± 94.2)	31.4%
$\bar{\nu}_\mu$ signal	20621.1 (± 42.6)	17.4%
ν_μ signal	16605.2 (± 84.0)	14.0%
Background	81493.1 (± 1254.9)	68.6%
Upstream wall	57689.2 (± 1063.0)	48.6%
Downstream wall	4.5 (± 3.2)	0.004%
Left pillars	714.7 (± 70.6)	0.6%
Right pillar	466.8 (± 8.4)	0.39%
Ceiling	12993.7 (± 515.0)	10.9%
Floor	9624.2 (± 417.7)	8.1%
Total	118719.0 (± 1258.4)	100%

the real data is 118084, so there is a good agreement between the data and simulation within the statistical error range. In this simulation, background events occupy about 70% of the simulated number of events. From this table, it can be said that back scattering events from the downstream wall are very rare.

5.4.3 Selected events

- **Basic plots**

In turn, basic distributions for selected events are shown in Fig.5.4.12–5.4.17. For each vertex plot, the ratio between the data and simulation is within 10% from unity. However, as to the Vertex Z plot, the plane number 8 has a large gap between the data and simulation. As shown in Fig.5.4.18, from the No.8 tracking plane, there are only 3 downstream planes. So, if the track is started from the No.8

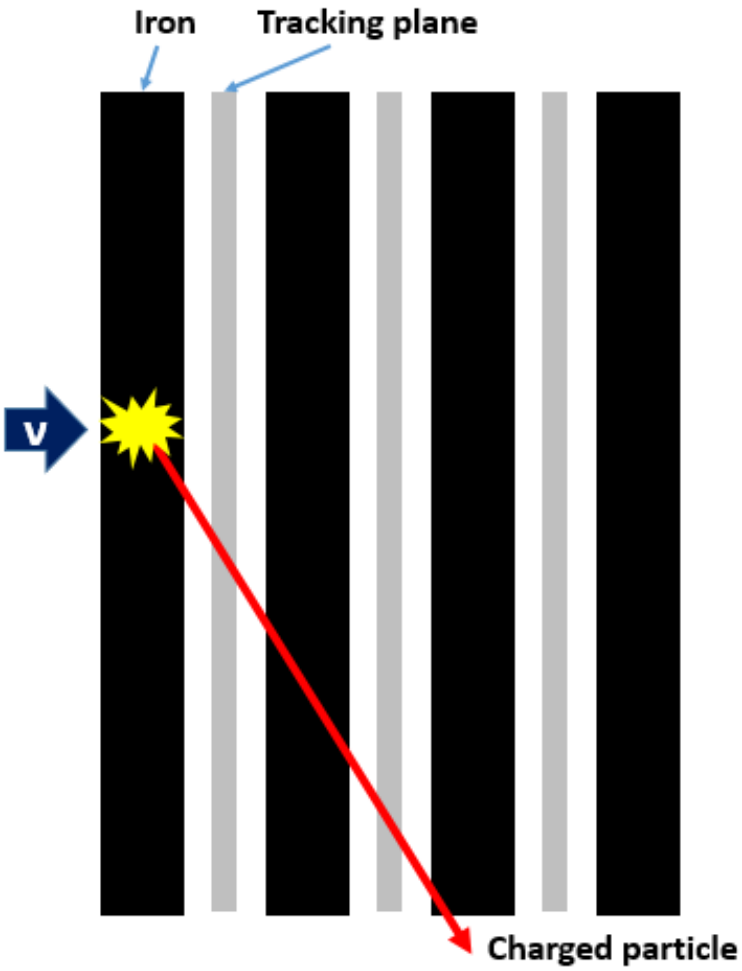

Figure 5.4.11: Illustration of the track of the charged particle which have the large angle to the beam axis

plane, the number of active plane is only 3, because of the event selection condition. However, due to the accidental hit from the MPPC noise in the more upstream side of plane, the number would be more than 3. In this simulation, the correction for the MPPC noise is not taken into consideration, so it would cause the decrease in the number of events of which the track is started from No.8 plane.

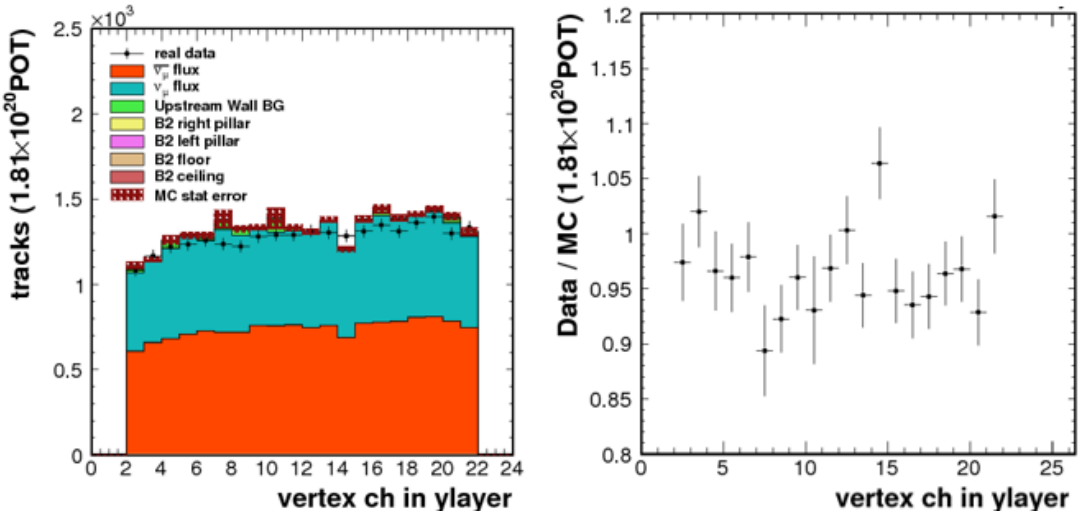

Figure 5.4.12: Basic distribution for Vertex X : The right figure shows the ratio between the data and simulation.

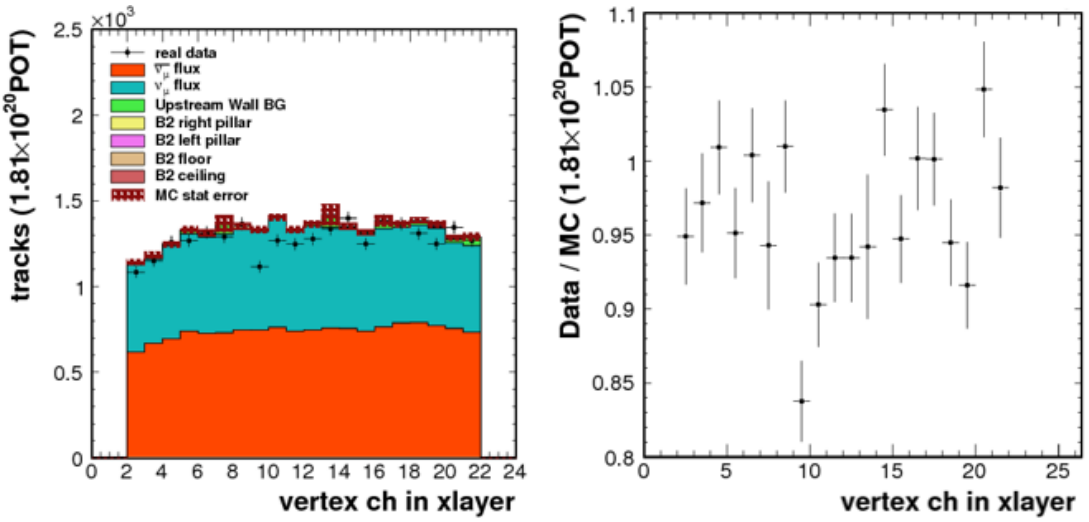

Figure 5.4.13: Basic distribution for Vertex Y and the ratio between the data and simulation

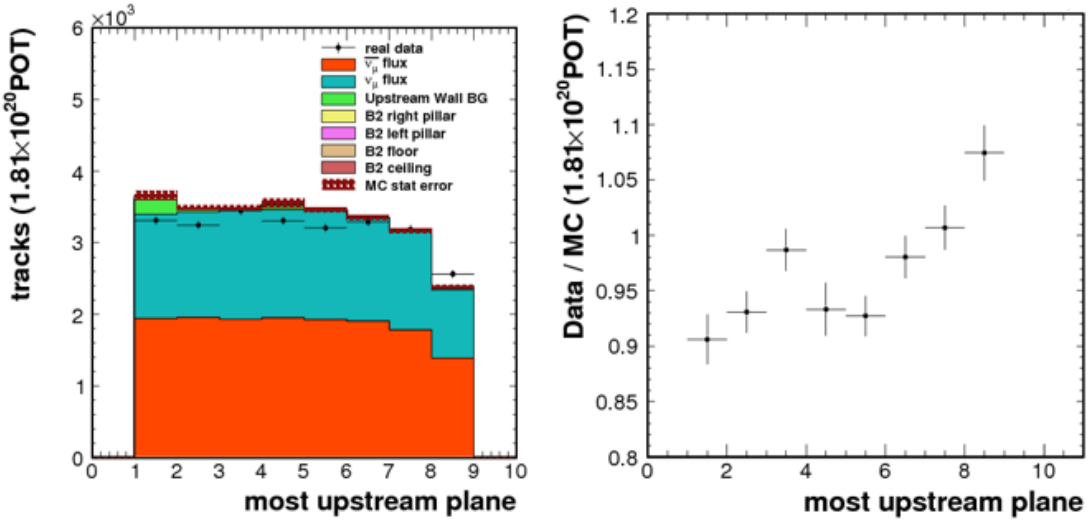

Figure 5.4.14: Basic distribution for Vertex Z and the ratio between the data and simulation

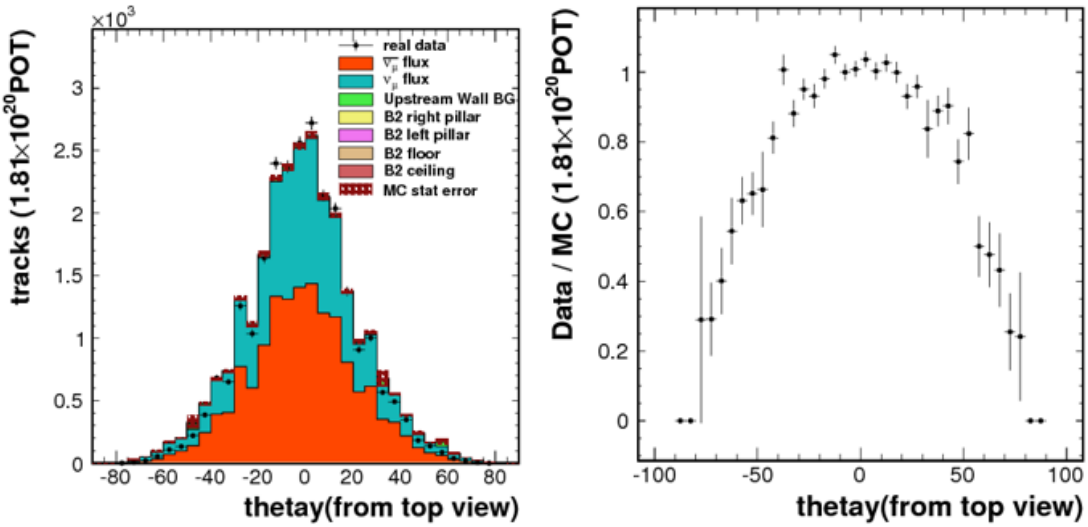

Figure 5.4.15: Angle distribution from the top view

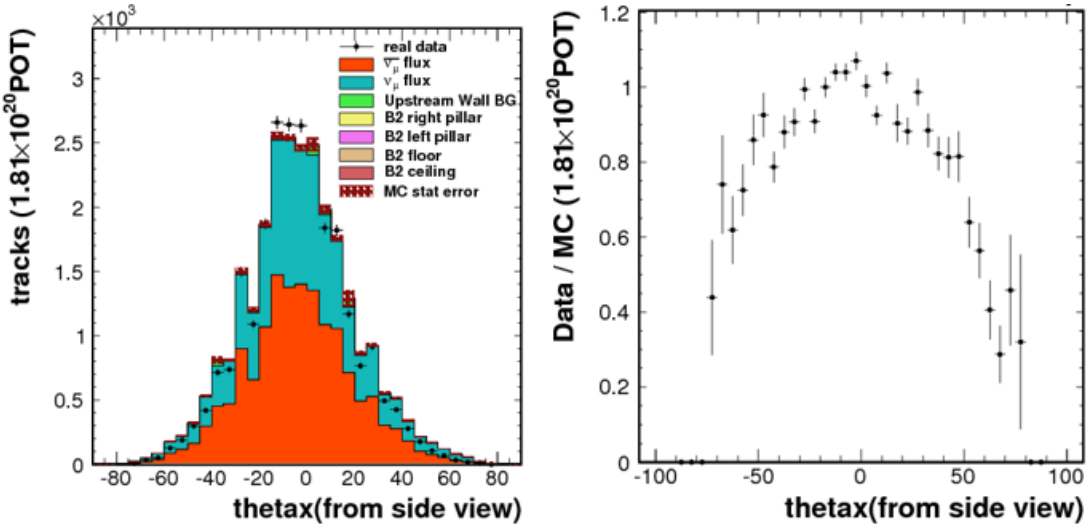

Figure 5.4.16: Angle distribution from the side view

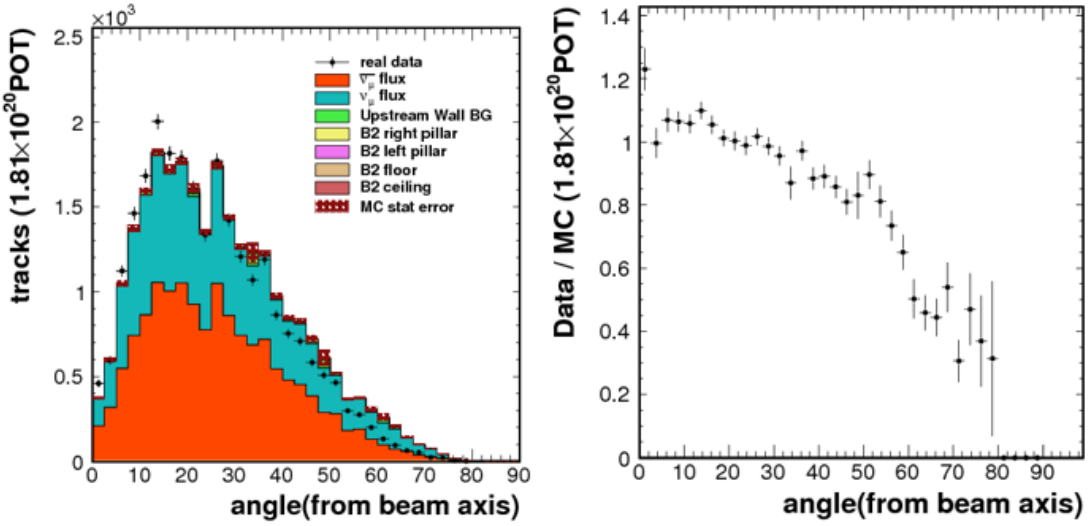

Figure 5.4.17: Three-dimensional angle distribution

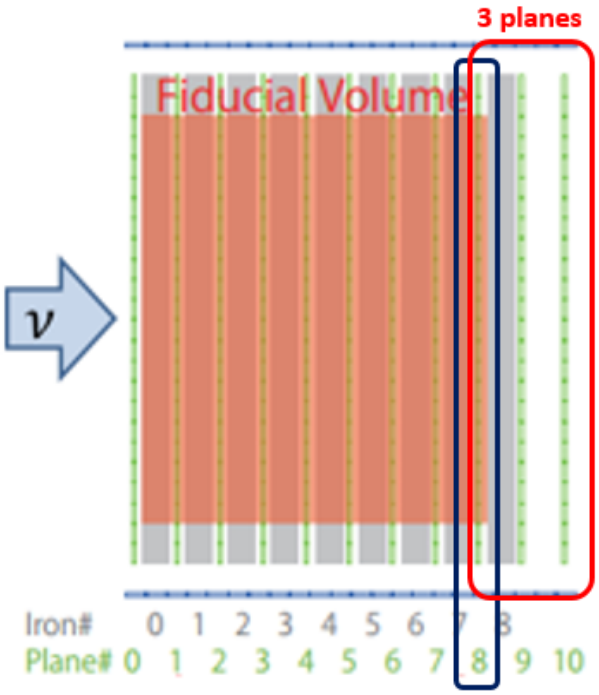

Figure 5.4.18: Illustration of inside of the B2 module : Only 3 planes exist downstream from the plane No.8.

- **Number of events**

Table.5.4.2 shows the number of selected events in the simulation. The total number of events in the real data is 26574, so there is a good agreement between the data and simulation within the error range. The table indicates that the estimated background fraction in the real data is 1.97 ± 0.34%. Especially, the upstream wall background events contribute about 70% to all background events.

Table 5.4.2: Number of selected events in the Monte Carlo simulation

	Number of events (Statistical error)	Ratio
Signal flux	26033.4 (± 77.7)	98.0%
$\bar{\nu}_\mu$ signal	14780.4 (± 35.8)	55.7%
ν_μ signal	11253.0 (± 69.0)	42.3%
Background	525.7 (± 90.4)	1.97%
Upstream wall	360.6 (± 85.2)	1.41%
Downstream wall	0.44 (± 0.26)	0.002%
Left pillars	29.4 (± 12.3)	0.11%
Right pillar	17.1 (± 1.6)	0.064%
Ceiling	51.8 (± 13.1)	0.20%
Floor	66.4 (± 24.3)	0.25%
Total	26559.1 (± 78.9)	100%

5.5 Conclusions and future prospects

Neutrino events are measured at an off-axis angle of 1.6 degrees. From plots of reconstructed and selected events, we find that there is a good agreement between the real data and simulated data, and there seems to be no strange flux in the B2 floor. The fraction of background events at the B2 module is about 2%, and especially, events from the upstream wall in the detector hall are dominant, about 70% in background events. Moreover, the event rate at the B2 module is very stable, so it is no problem to locate a new neutrino detector there. In the near future, this background study will be applied to the analysis of the new detector.

Chapter 6

WAGASCI experiment

This is a new experiment at the J-PARC neutrino beam line to measure the neutrino cross section ratio between water and hydrocarbon targets for charged current interactions with a large angular acceptance[31].

6.1 Motivation

6.1.1 Physical motivation

As described in Chapter 2, ND280 measures the neutrino flux, energy spectrum, and neutrino-nucleus cross sections before the neutrino oscillation and reduce uncertainties of them. However, the target nucleus is different from the far-detector SK, the ND280 target is mainly hydrocarbon and SK is water. Table.6.1.1 shows systematic errors in the T2K neutrino oscillation analysis. In this table, the systematic error due to the nuclear targets difference between detectors has largest value. This uncertainty affects precise measurements of the neutrino oscillation, so it is necessary to reduce it. Moreover, ND280 can measure mainly forward scattering events, on the other hand, SK has 4π angular acceptance. The difference in acceptance is also contributes to systematic errors. That is why we propose a new experiment using the detector which can measure the relation of neutrino interaction cross section between water and hydrocarbon with a large angular acceptance.

6.1.2 Technical motivation

Table 6.1.1: Systematic errors in the T2K neutrino oscillation analysis : ND indicates ND280

Systematic error source		ν_μ sample	ν_e sample	$\bar{\nu}_\mu$ sample	$\bar{\nu}_e$ sample
ν flux and cross section	w/o ND measurement	21.8%	26.0%	9.2%	9.4%
	w/ ND measurement	2.7%	3.1%	3.4%	3.0%
ν cross section due to difference of nuclear target btw near and far		5.0%	4.7%	10%	9.8%
Final or secondary hadronic interaction		3.0%	2.4%	2.1%	2.2%
SK		4.0%	2.7%	3.8%	3.0%
total	w/o ND measurement	23.5%	26.8%	14.4%	13.5%
	w/ ND measurement	7.7%	6.8%	11.6%	11.0%

The uncertainty of the neutrino flux is more than 10%[1], so the absolute cross section measurement has also large value. To reduce this uncertainty is essential, and there is a previous research which has resolved this difficulty. In that research, the Proton Module (PM) and INGRID are used for measuring the neutrino interaction cross section ratio between hydrocarbon and iron with a 3% accuracy[32]. The research paid attention to the relation of the position of PM and the center module of INGRID (Fig.6.1.1). The INGRID central module is on the same beam axis as PM. So, as to the measurement of the cross section ratio, many of the large systematic errors from uncertainties on the neutrino flux are canceled between two detectors. Referring to this uncertainty cancellation method, 2 water target modules and 2 hydrocarbon target modules are placed alternately in the WAGASCI detector, as described in Sec.6.3.

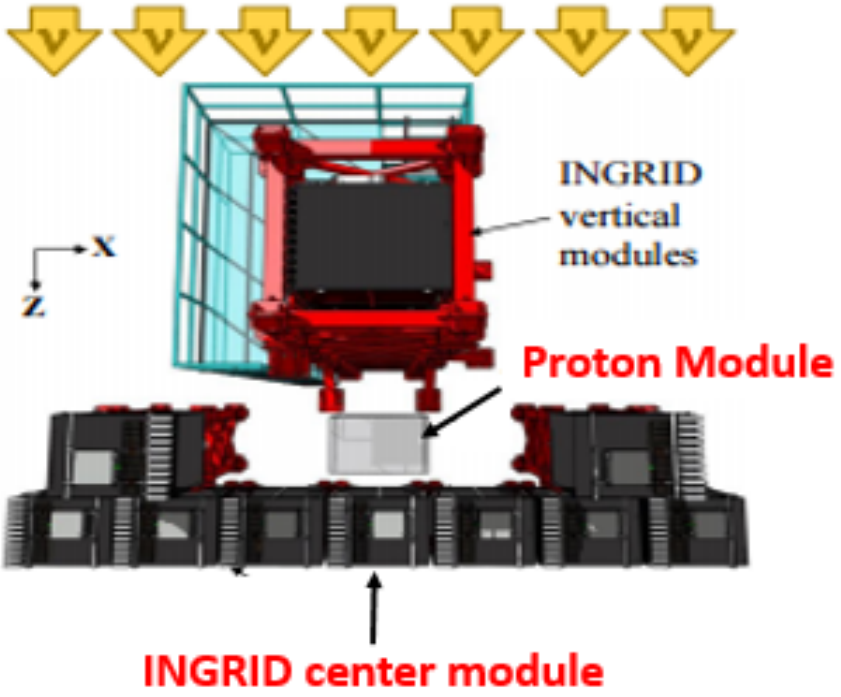

Figure 6.1.1: The position relation between Proton Module and INGRID

6.2 Candidate site of the WAGASCI detector

In order to reduce the uncertainty related to ND280, the neutrino flux in the WAGASCI detector is required to be as similar as possible in that in ND280. Although it is best to locate the detector at the same place as ND280, there is no space around ND280 to place the detector. For that reason, we plan to place the detector where the B2 module is now placed (Fig.6.2.2) and the difference in the flux between ND280 and

[1]The neutrino flux uncertainty sources are hadron production uncertainties and T2K beam line uncertainties.

B2 module is very small, as shown in Fig.6.2.1.

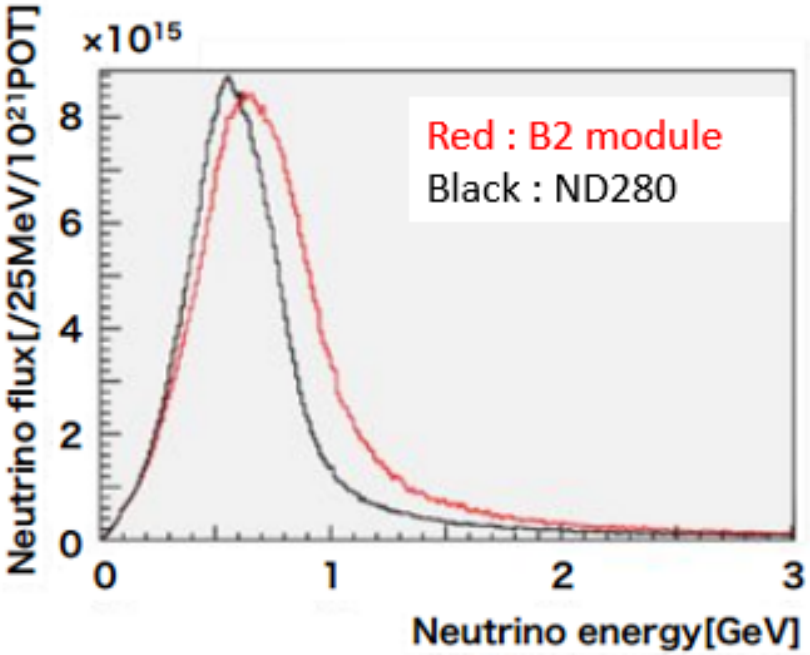

Figure 6.2.1: Energy spectra of the neutrino flux in ND280 and B2 module

6.3 Detector components

Fig.6.3.1 shows the detector of the WAGASCI experiment. This detector mainly consists of the central detector and Muon Range Detectors (MRD). Electronics and water system are also explained in this section.

6.3.1 Central detector

The central detector is composed of 2 water target modules and 2 hydrocarbon target modules and they are located alternately. The size of each module is 1 m × 1 m × 0.5 m, as shown in Fig.6.3.2, and each module consists of 4 sub-modules each of which has 4 scintillator layers. The mass of each module is 0.5 ton, that is to say, each target mass is 1 ton. Each module has a characteristic structure, 3D grid-like plastic scintillators, as shown in Fig.6.3.3. Thanks to this 3D structure, the WAGASCI detector has almost 4 π angular acceptance, as shown in Fig.6.3.4. The size of each scintillator is 0.3 cm × 2.5 cm × 100 cm, and that of the space between scintillators is 5.0 cm × 5.0 cm × 2.5 cm, and water or hydrocarbon targets are put in each space. The space between scintillators is very short, so it is expected to reconstruct the short track produced by particles such as the proton or pion. The signal readout method is almost same as the INGRID case, with WLS fibers and MPPCs. On each scintillator, there is a groove (ϕ=1.0 mm) to set the WLS

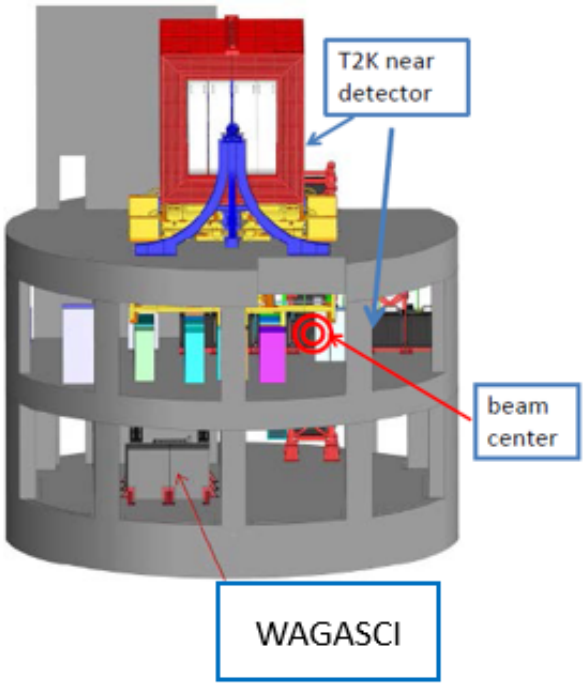

Figure 6.2.2: Candidate site of WAGASCI detector : In this position, off-axis angle is 1.6 degrees.

fiber, as shown in Fig.6.3.5. The fiber is glued with each scintillator by the optical cement, EJ-500. After gluing, the white reflective coating, Avian-D[2][33] is painted on the groove to protect the crosstalk between grid-like scintillators. The reflectance of Avian-D is shown in Fig.6.3.6, and in the WAGASCI scintillator case, the emission wavelength peak of 4.25 nm, it is about 97%. Fibers are connected with MPPCs by optical connectors. There are 1280 scintillators in each module, so the central detector has 1280 ch $\times$ 4 = 5120 ch.

[2]Produced by Avian Technologies LLC

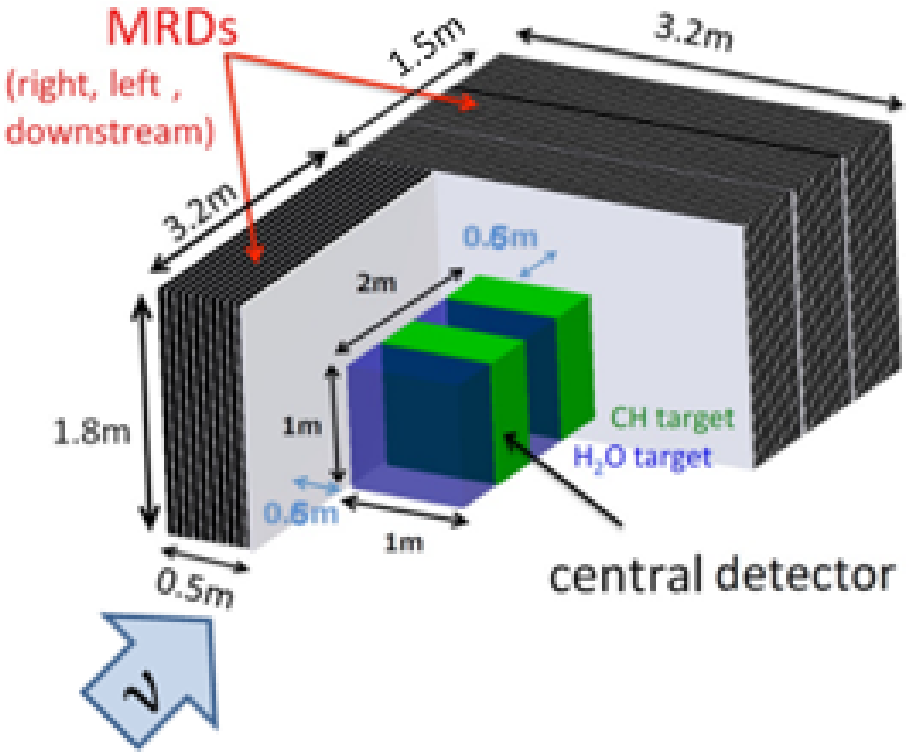

Figure 6.3.1: Illustration of the WAGASCI detector : Scintillators and the right side MRD are omitted.

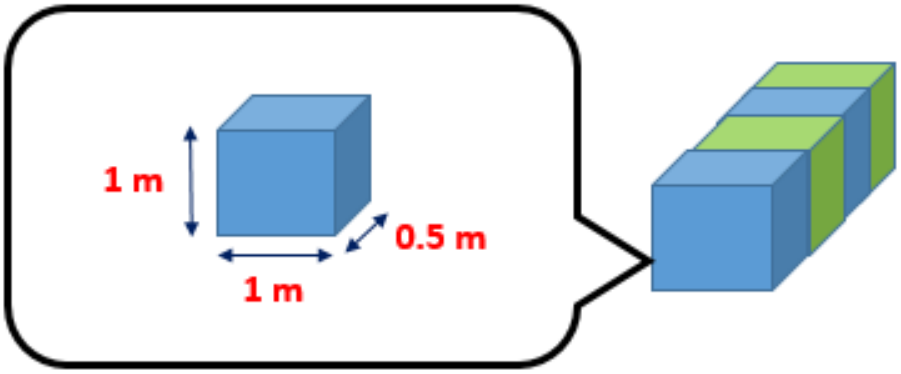

Figure 6.3.2: Illustration of the WAGASCI central detector

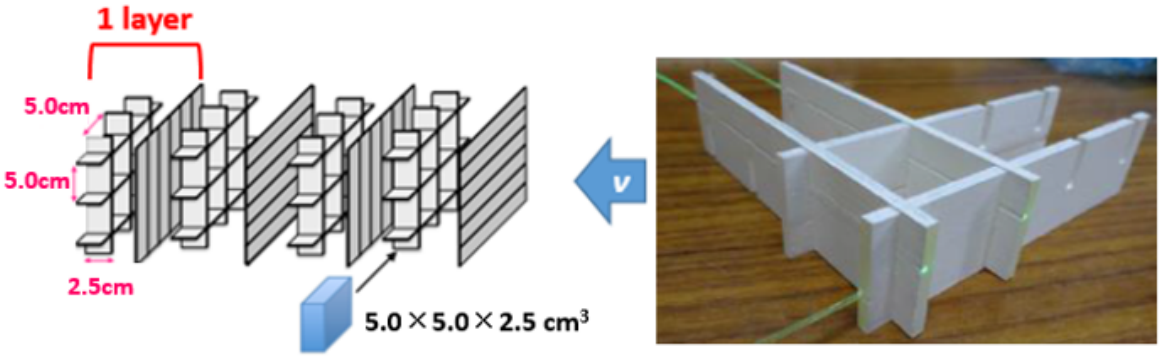

Figure 6.3.3: 3D grid-like scintillators

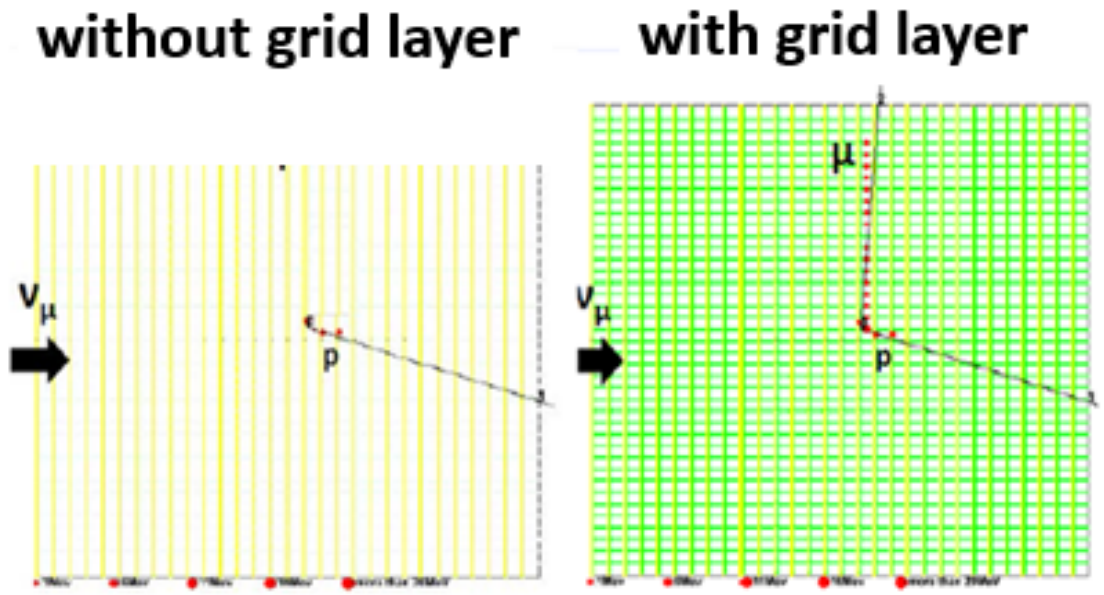

Figure 6.3.4: Event display in the MC simulation : The right figure shows that the track which has a large angle is well reconstructed.

Figure 6.3.5: WAGASCI scintillator : There is a groove on the scintillator.

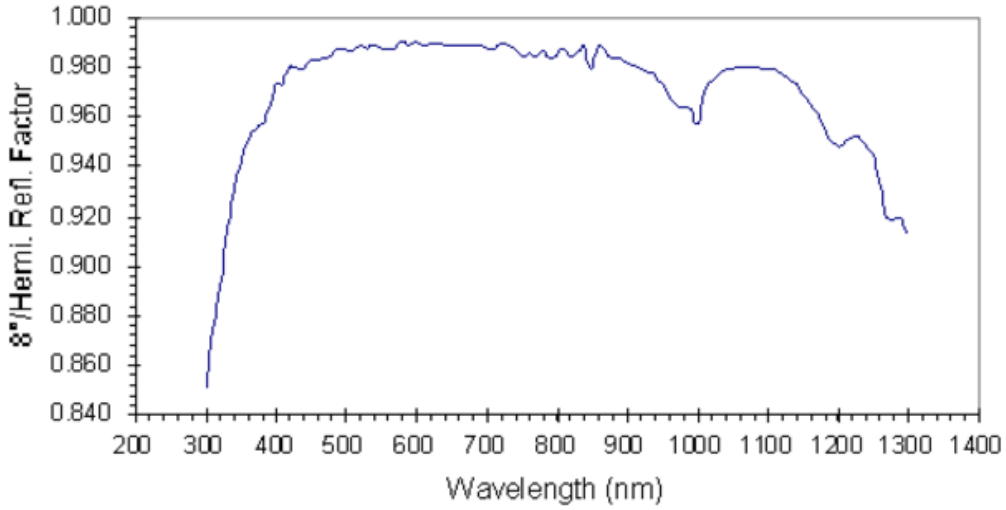

Figure 6.3.6: Reflectance of Avian-D

Components of the central detector

The central detector mainly consists of plastic scintillators, WLS fibers, and MPPCs, as mentioned in Sec6.3.1.

- **Scintillator**

  The material and production method of WAGASCI scintillators are the same as that of the T2K near-detectors, but the size is slightly different. The thickness of each scintillator is as thin as possible, 3 mm, to have the target volume as much as possible. In the central detector, the targets to scintillators ratio is 79% : 21%. However, it is concerned that the thickness of scintillators causes the very low light yield. Moreover, WAGASCI scintillators have slits and it would lead to a low particle detection efficiency. That is the reason why the performance test of scintillators has been done using 589 MeV positron beam at Tohoku University. In the test, we confirmed that the light yield of each scintillator is more than 10 p.e.[3] and the detection efficiency is more than 99% in the whole area. Result plots are shown in Fig.6.3.7 and Fig.6.3.8, and we could obtain satisfactory results. Moreover, these scintillators are put in the water to check the stability of the quality of scintillators. Fig.6.3.9 shows the result of the stability test, and the fluctuation of the light yield turned out to be within 2.5% (1 p.e.). Based on these results, we concluded that these scintillators can be used in the WAGASCI detector.

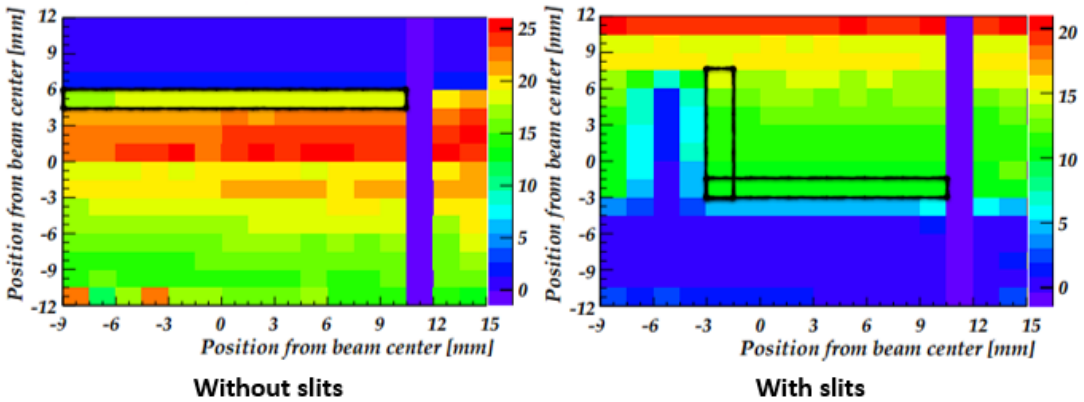

Figure 6.3.7: Light yield test results : Considering only the black box region where is expected to have the low light yield, the light yield of the scintillator is enough, more than 10 p.e.. The purple region shows the dead channel.

- **WLS fiber**

  The Y-11(200)MS is used, as same as the T2K near-detectors. In the water, the light yield of scin-

[3]The threshold of the light yield of scintillators is 1.5 p.e. in the WAGASCI experiment

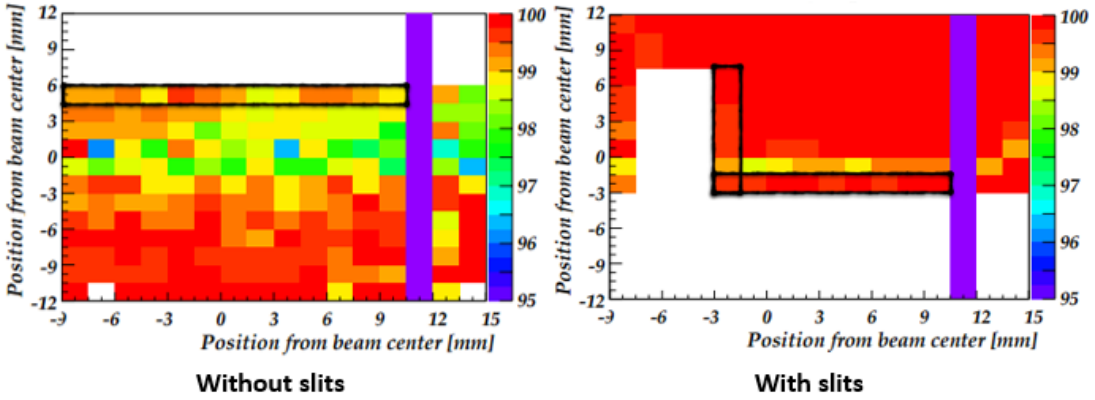

Figure 6.3.8: Detection efficiency results : Considering only the black box region, the detection efficiency is enough, more than 99%.

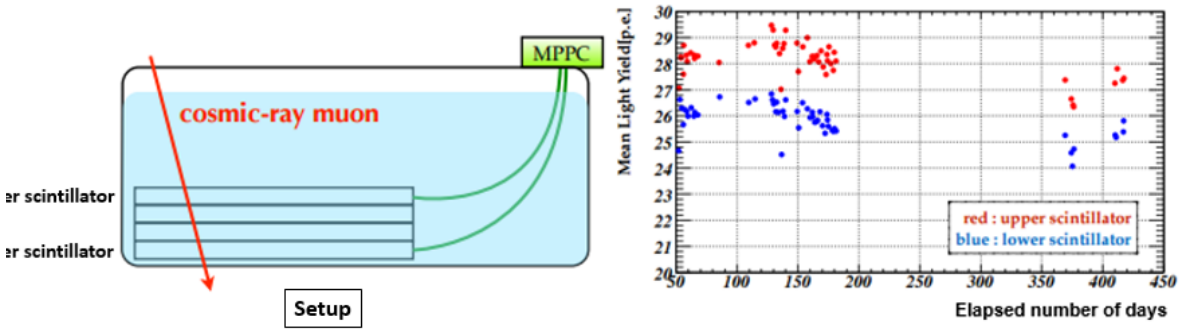

Figure 6.3.9: Stability test of scintillators by cosmic-rays : The temperature in the water was kept in 30 degrees.

tillator is increased in comparison with the case in the air[34], as shown in Fig.6.3.10. The reason is that the light collection efficiency is changed in the water. As shown in Fig.6.3.11, the refractive index is different between in the air and in the water. In the water, the angle the total reflection occurs is larger than that in the air, so fibers can get more light and it results in the increase of the light yield. By the way, as shown in Chapter 7, the fiber is bent for the detector construction to be inserted into the fiber bundle, so it is necessary to check the light yield corresponding to a variety of the radius of curvature of the fiber. The result is shown in Fig.6.3.12, and there is only a few fluctuation of the light yield, so there is no problem to bend the fiber to some extent.

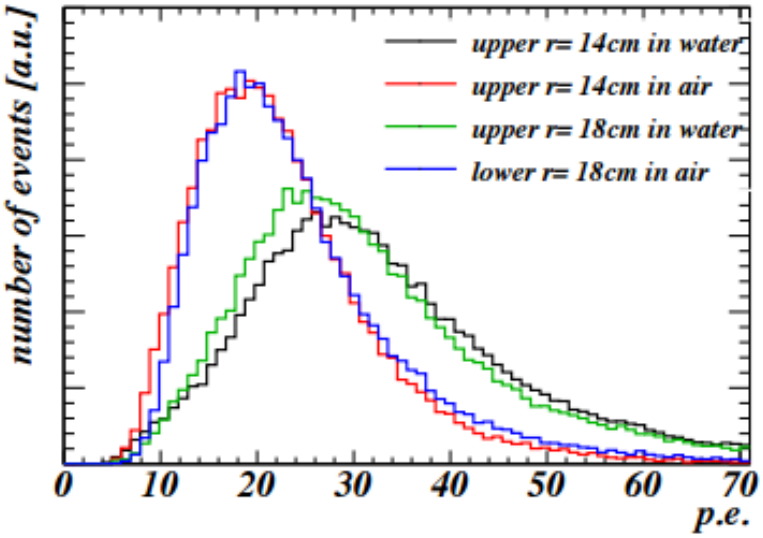

Figure 6.3.10: Light yield measurement by cosmic-rays : The setup is as same as Fig.6.3.9, and r means the radius of curvature of the fiber.

- **MPPC**

In the WAGASCI central detector, 32ch array-type MPPCs are used[4]. The drawing plan and picture of this type of MPPC is shown in Fig.6.3.13. The MPPC has 716 pixels at the 50 μm intervals and the diameter of each pixel is 1.5 mm. In MRDs, single-type MPPCs which have 667 pixels (1.3 mm $\times$ 1.3 mm) are used[5]. These MPPCs are new crosstalk suppression types, and different from MPPCs

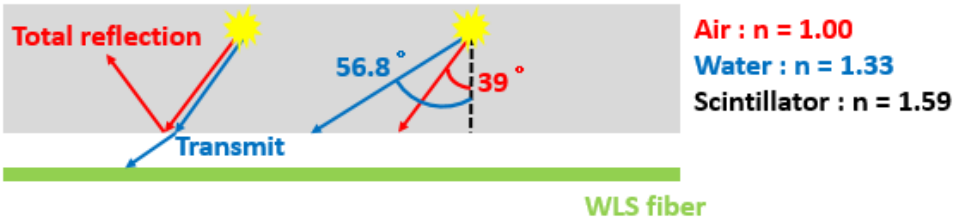

Figure 6.3.11: Illustration of the difference in the refractive index between in the air and in the water

[4] 168 MPPCs are used : 5376 ch
[5] 2750 MPPCs are used

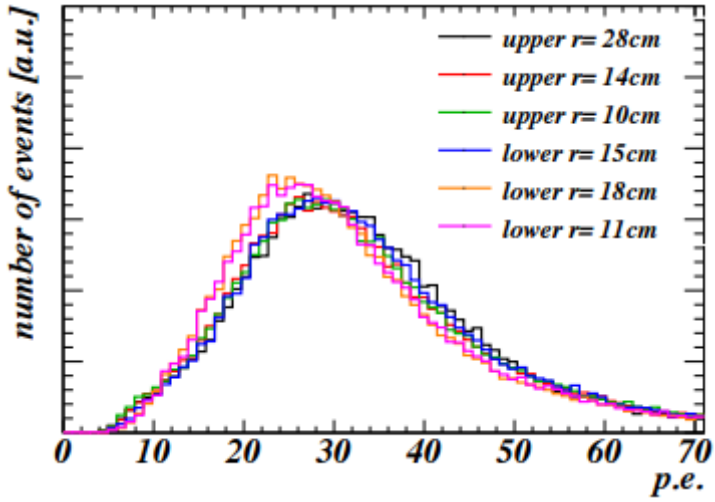

Figure 6.3.12: Light yield measurement by cosmic-rays for a variety of the radius of fiber curvature

in the T2K near-detectors. WAGASCI scintillators are very thin, and the light yield is lower than T2K scintillators, so the noise could have a large ratio. That is why it is important to reduce noises in MPPCs and for MPPCs to have the high detection efficiency for the precise measurement. The noise rate of older MPPC and new MPPCs are shown in Fig.6.3.14, and you can see that the noise of new MPPCs is dramatically suppressed. In Fig.6.3.15, the photon detection efficiency of the new MPPC is lower than that of the old type. However, new type MPPCs can be applied higher over voltage than older types, so in the high over voltage region, they can get the high photon detection efficiency. Before the construction of the WAGASCI detector, the performance of all new MPPCs should be evaluated, and the mass test of them is planed to do. Thermoelectric coolers are proposed to mount to the detector in order to prevent MPPCs from the heat problem. For example, the breakdown voltage of them is fluctuated by the ambient temperature, so we should take any countermeasure for the heat.

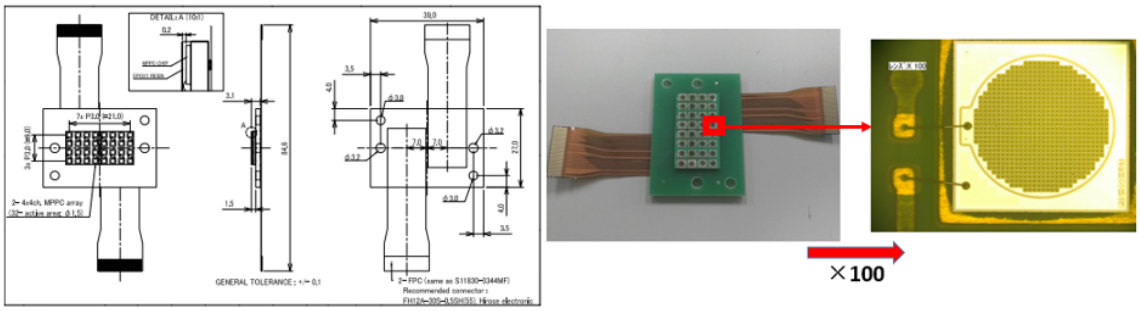

Figure 6.3.13: 32 ch array-type MPPC

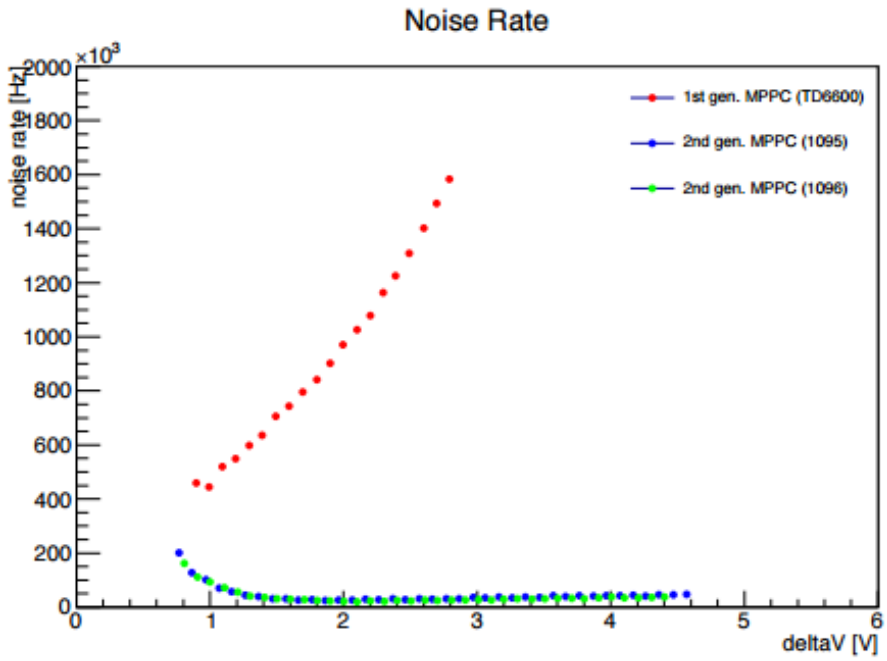

Figure 6.3.14: Noise rate of MPPCs : 1st gen. MPPC is the T2K type, and 2nd gen. MPPC is the WAGASCI type.

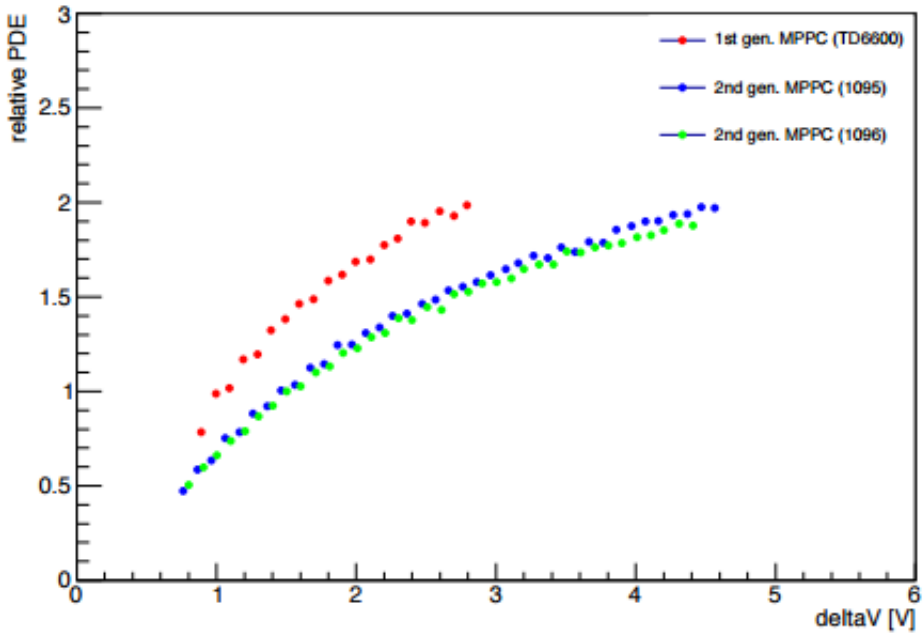

Figure 6.3.15: Photon detection efficiency of MPPCs

- **Fiber bundle**

In order to connect WLS fibers to MPPCs, the fiber bundle (Fig.6.3.16) is used. It has 32 holes (ϕ=1.0 mm), and in each hole the fiber is inserted. Each hole corresponds to the position of the active region of 32 ch array-type MPPC, and the distance between the fiber and the MPPC is several mm. After fibers are inserted to fiber bundles, the surface of the fiber bundle is polished, as shown in Fig.6.3.17. This polishing process is necessary to make the distance between all the fiber edges and MPPCs the same. If the distance is not constant, the light yield of scintillators could fluctuate and it affects the track reconstruction, the particle identification, and so on. The polishing work is described in Chapter 7.

Figure 6.3.16: Picture of the fiber bundle

Figure 6.3.17: Polished fiber bundle

6.3.2 Muon Range Detector

MRD has the sandwich structure of the iron and scintillator, and is used in order to detect muons and measure their momentum, like the T2K INGRID detector. MRDs surrounds the central detector at a distance of 50 cm, as shown in Fig.6.3.18. The size of each side MRD is 1.8 m $\times$ 3.2 m $\times$ 0.5 m, and that of the downstream MRD (dMRD) is 1.8 m $\times$ 3.2 m $\times$ 1.5 m. The thickness of dMRD is larger than that of side MRDs because the track of the high energy muon has a small angle to the beam axis, and that muon has to stop in the dMRD in order to measure its momentum[6]. The signal readout method is almost same as the INGRID, WLS fibers and MPPCs are used. Scintillators in MRDs have relatively large width (20 cm[7]), so in order to get enough light yield by WLS fibers, these fibers are putted in a zigzag shape, as shown in Fig.6.3.19. Two MPPCs are connected to both edge of a WLS fiber, and the hit position is measured by the hit timing difference between two MPPCs. Fig.6.3.20 shows the result of the light yield measurement by cosmic-rays, and it indicates that it is better to read out signals from both sides of the scintillator.

MRDs are also used for rejecting background events coming from the outside of the central detector. Both the central detector and MRDs are surrounded by scintillators[8], and we detect backgrounds using the time of flight information. Measuring the residual of hit timings T_{MRD} - $T_{central}$, the direction of charged particles produced can be measured. Then, requiring the residual to be more than 0, the background events generated outside of the central detector, such as MRDs or the wall of the detector hall, are removed, as shown in Fig.6.3.21. For these scintillators, single-type MPPCs are used, as same as MRDs.

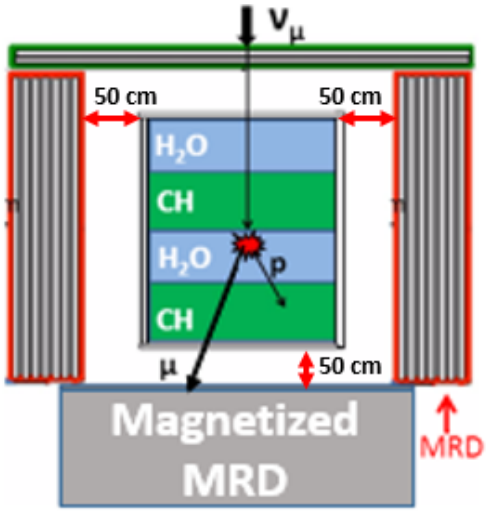

Figure 6.3.18: Muon range detectors surrounding the central detector at 50 cm intervals

[6]Side MRD can measure the muon momentum up to 1 GeV, and dMRD can up to 2 GeV.
[7]The width of scintillators in the INGRID detector is 5.0 cm, and in the WAGASCI detector is 2.5 cm
[8]The size of scintillators is 180 cm $\times$ 50 cm $\times$ 1 cm, and they have good time resolution, 1ns.

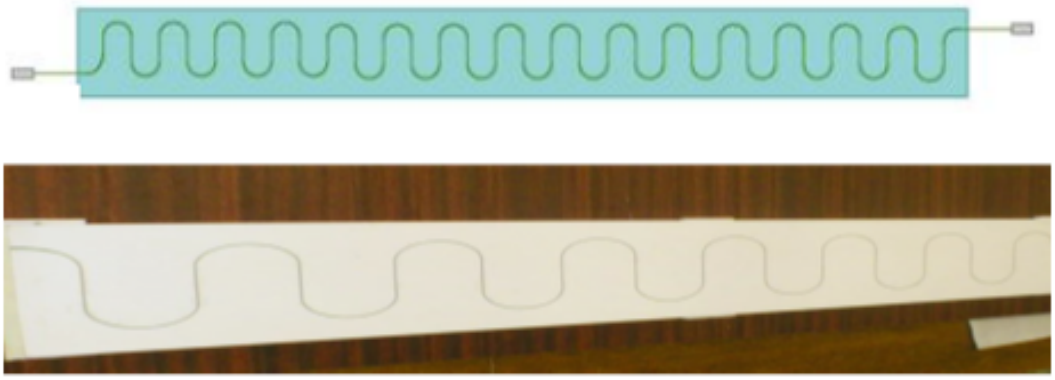

Figure 6.3.19: Illustration and picture of the scintillator in MRDs

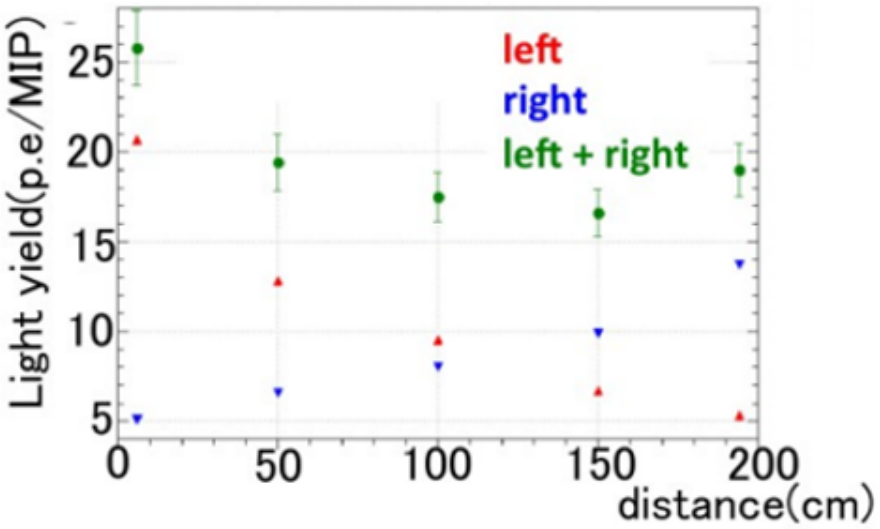

Figure 6.3.20: Light yield of the MRD scintillator measured with cosmic-rays

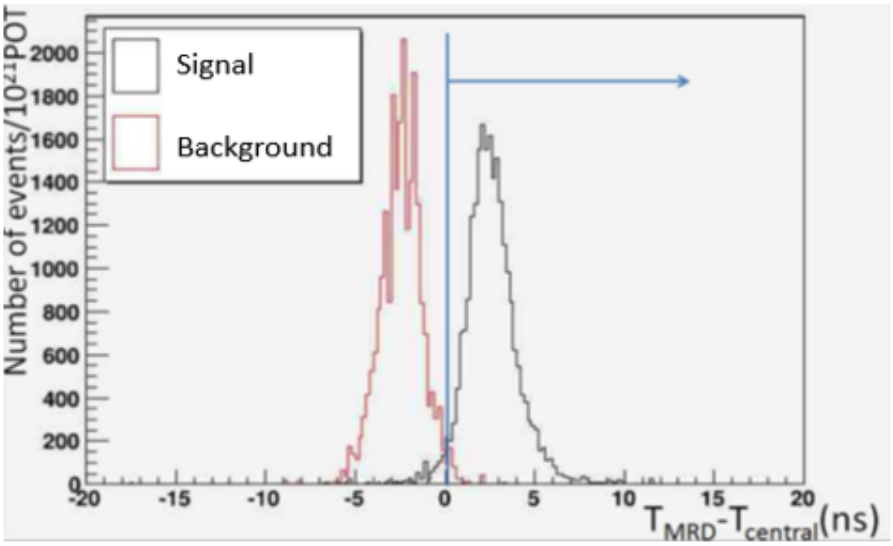

Figure 6.3.21: The time residual of hit timings between MRDs and the central detector

Magnetized downstream MRD

The anti-muon neutrino beam mainly contains $\bar{\nu}_\mu$, and ν_μ is also contained, about 10%. On the other hand, the fraction of events from ν_μ interactions (Fig.6.3.22) is about 30% because $\bar{\nu}_\mu$ has smaller cross section than ν_μ. That is why we decided to use the magnet with the dMRD to distinguish between μ^- from the ν_μ interaction and μ^+ from the $\bar{\nu}_\mu$ interaction. For the WAGASCI experiment, MIND (Magnetized iron neutrino detector) will be used. It is developed by Geneva University and has already been tested at CERN. The magnet consists of steel and coils, and the overview is shown in Fig.6.3.23. The generated magnetic field is uniformly 1.5 T for the whole region. Using such kind of magnet, iron planes are magnetized, and they enable the WAGASCI detector to identify the charge of muons and reject ν_μ interaction backgrounds. The identification efficiency is expected to be 89% for the anti neutrino mode and 87% for the neutrino mode, and the ν_μ contaminations in the all interactions are reduced down to 2.9% in the MC simulation. The development of the dMRD is now on-going.

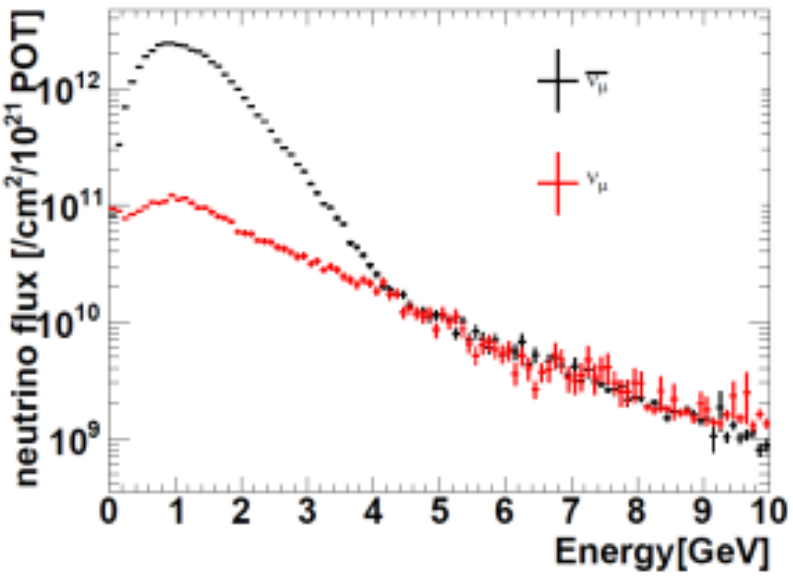

Figure 6.3.22: The energy spectrum for $\bar{\nu}_{mu}$ and ν_μ in the anti muon neutrino mode

6.3.3 Electronics

The electronics design is now ongoing by LLR[9] in France, and it is based on the SPIROC2[35] (Silicon PM integrated Read-Out Chip)[10]. The circuit in SPIROC2 is shown in Fig.6.3.24. It is an auto-triggered, bi-gain, and 36 channel ASIC which allows to measure on each channel the charge from 1 to 2000 p.e. and the signal timing by TDC with a 100 ps accuracy. The overview of the data acquisition system for the WAGASCI central detector is shown in Fig.6.3.25. Each ASU (Active Sensor Unit) has SPIROC2 chip, as

[9] Laboratorie Leprince-Ringuet, Ecole Polytechnique
[10] The SPIROC[36] is developed by the OMEGA group in France for an ILC hadronic calorimeter technical prototype.

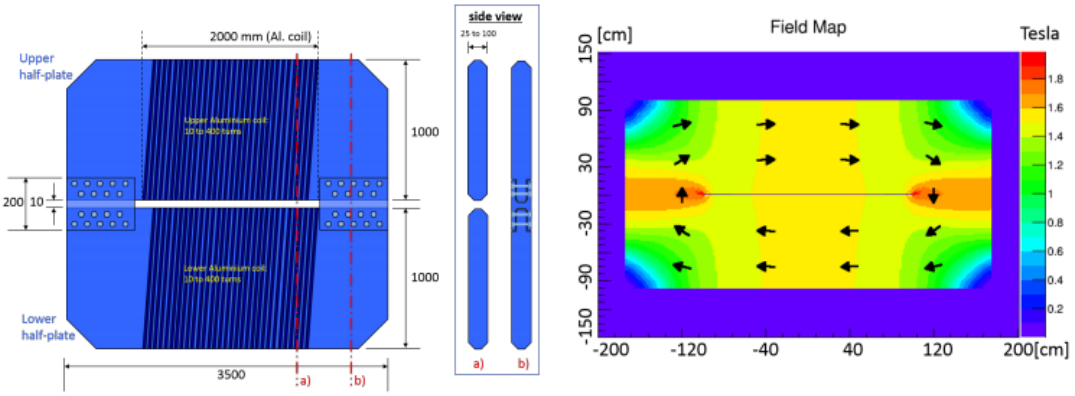

Figure 6.3.23: Configuration and field map of the magnet for the MIND : The field map is with 2.5 kA current in 400 turns aluminum coils.

shown in Fig.6.3.26, and is connected to a 32 ch array-type MPPC. Interface contains a NIM connection for the MPPC bias voltage supply. DIF (Detector Interface) gives and takes data between ASU, and its firmware is controlled by the GDCC (Giga Data Concentrator Card) which has an FPGA. GDCC is connected with DAQ PC and sends readout data to it with an Ethernet. GDCC also connects with CCC (Clock & Control Card), and receives clock signals and fast controls from it. MRDs and veto planes have similar electronics, and in total, there are 226 ASUs, 26 Interfaces, 26 DIFs, 5 GDCCs, and 1 CCC[11]. Using such kind of electronics, 7760 channels of MPPCs are read out.

Now, the electronics is evaluated in LLR. Fig.6.3.27 shows a setup for the test operation. As a SPIROC chip, SPIROC2B and SPIROC2D are tested. SPIROC2B is an older version, and is found a problem of TDC. It has a large dead time due to the multiplexer, as shown in Fig.6.3.28. This problem is solved in the newer version, SPIROC2D by implementing a rising and a falling ramp. SPIROC2B chips are used in the test just because it has already been confirmed the operation. In the WAGASCI detector, only SPIROC2D chips will be applied.

6.3.4 Water system

In order to fill gaps in grid-like scintillators with the water[12], water modules are installed to the water tank, as shown in Fig.6.3.29. The water system now under preparation is shown in Fig.6.3.30. The water would not circulate in this system, and the compound is used as the antiseptic to keep the purity of the water.

[11] CCC is in common with the central detector, MRDs, and veto planes.
[12] Hydrocarbon target would be a solid matter, so it is not necessary to prepare tanks for hydrocarbon target modules

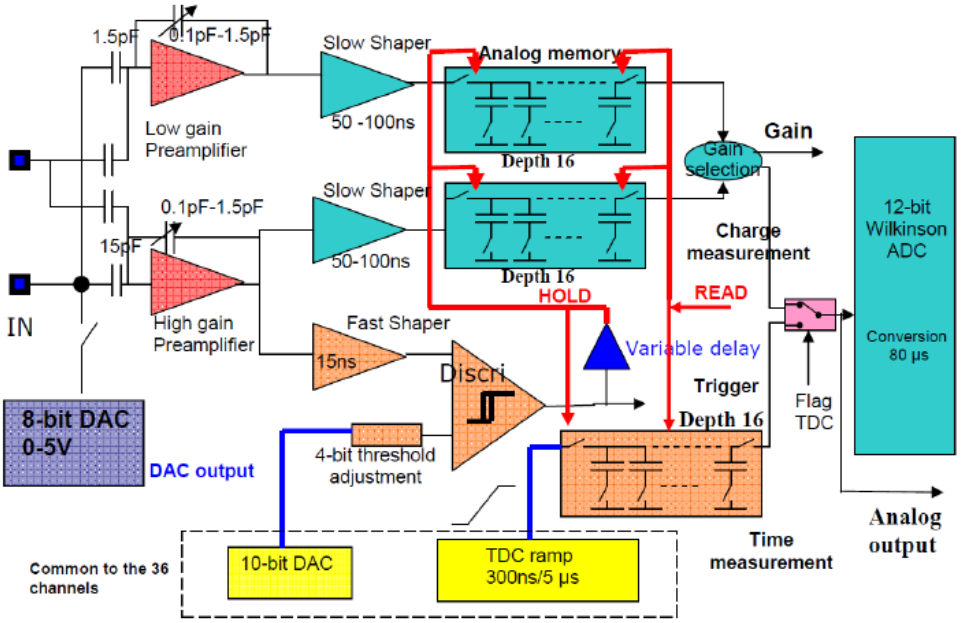

Figure 6.3.24: Illustration of the circuit in SPIROC2

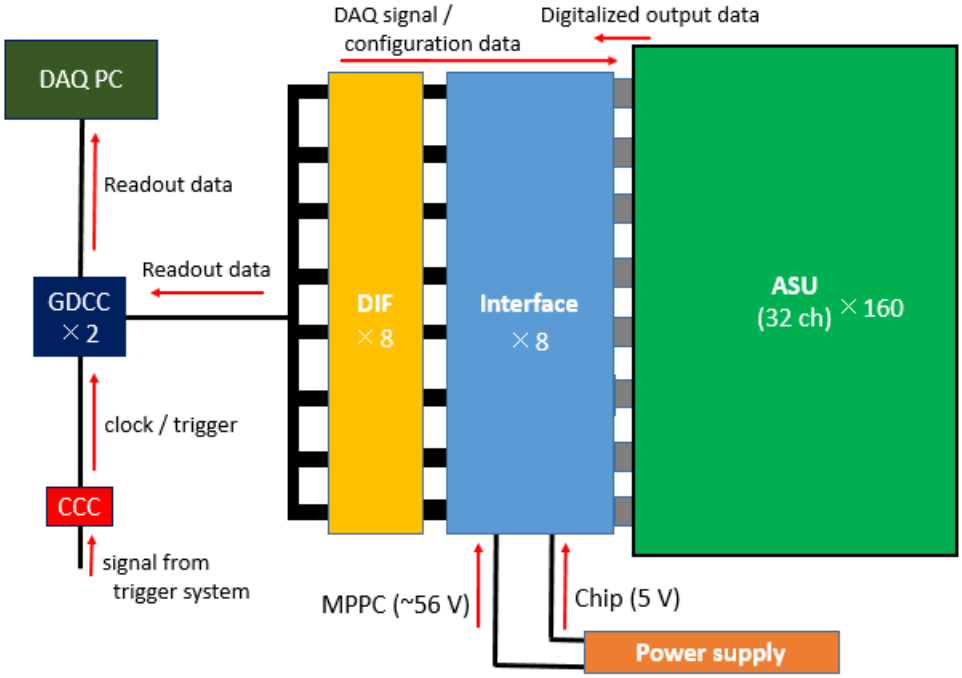

Figure 6.3.25: Illustration of DAQ for the WAGASCI central detector

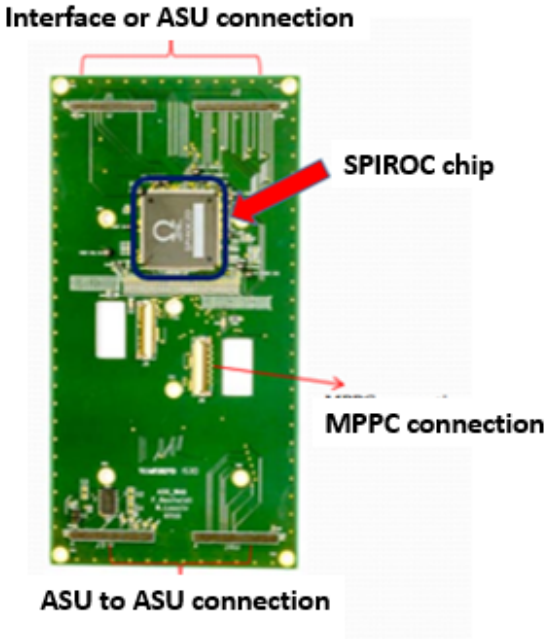

Figure 6.3.26: Picture of the ASU board

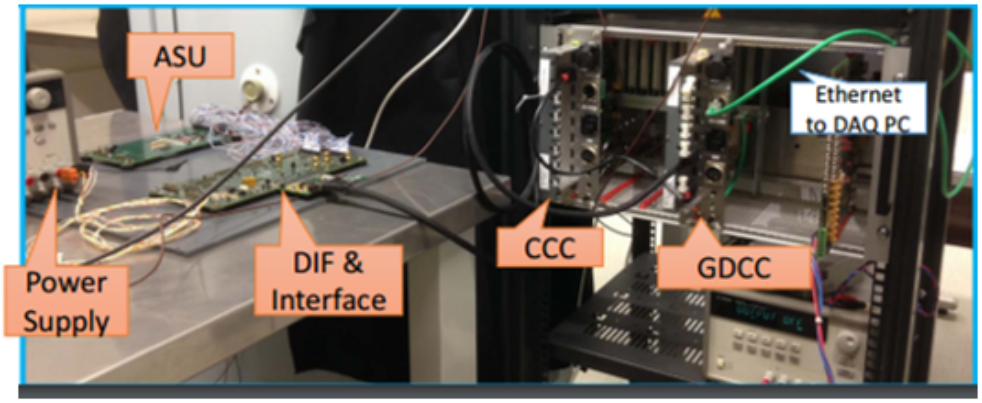

Figure 6.3.27: Setup for the SPIROC performance test

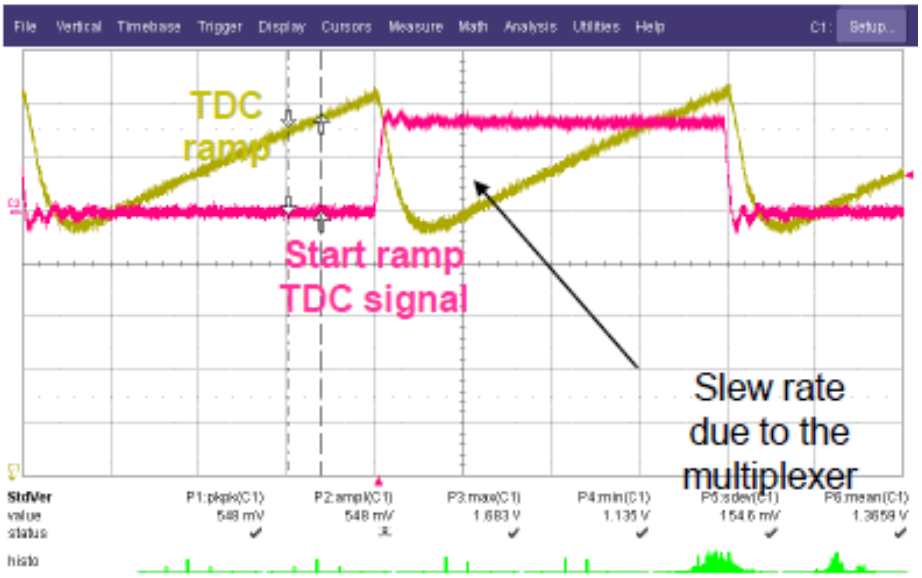

Figure 6.3.28: SPIROC2B TDC

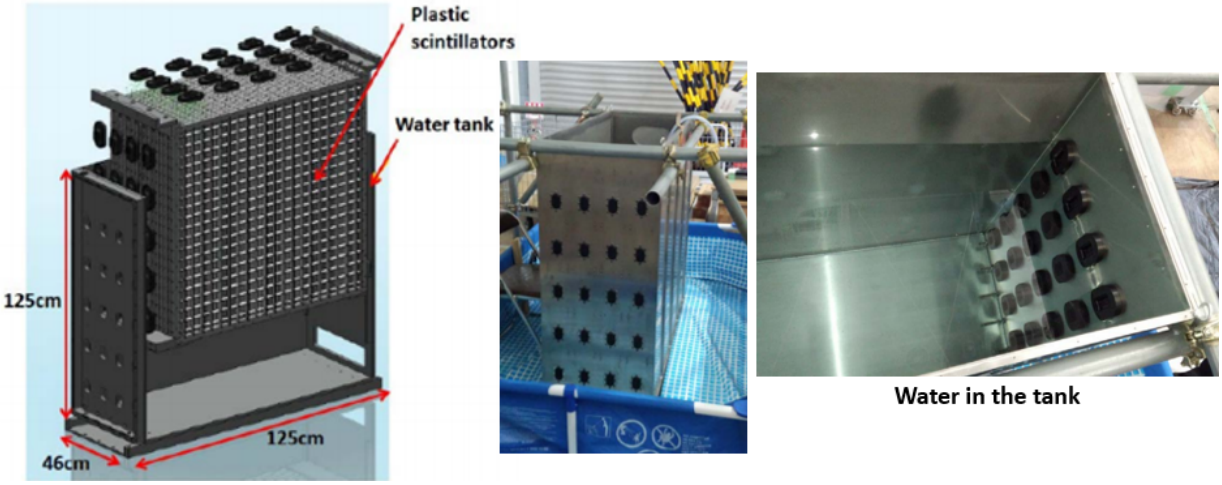

Figure 6.3.29: Illustration and picture of the water tank

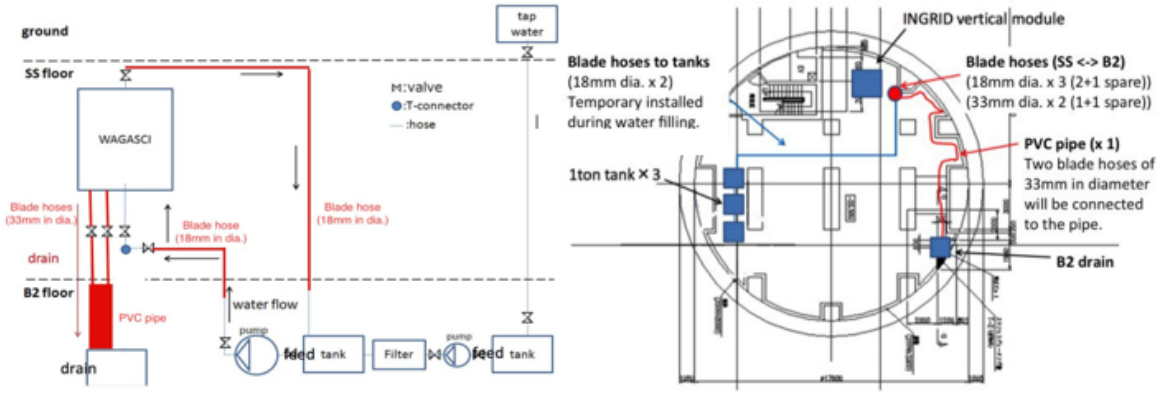

Figure 6.3.30: Water system

6.4 Prototype detector : INGRID Water Module

Now, we in the WAGASCI group are constructing the 1 central water module as a prototype of the WAGASCI detector, named INGRID Water Module. The construction work is described in Chapter 7. This detector will be placed on the beam axis where now the Proton Module is located, as shown in Fig.6.4.1. Compared with the candidate site of the WAGASCI detector, the on-axis position has the advantage of the efficiency to accumulate the statistics. So, we can quickly evaluate the performance of the INGRID Water Module. By this performance test, we will confirm the particle reconstruction efficiency, the ability to identify the particle, and so on. Around this detector, there will be no MRDs because there is no space to set them. So, in order to identify whether detected charged particles produced from ν_μ interactions or $\bar{\nu}_\mu$ interactions, only 1 reconstructed track is required. As shown in Fig.6.4.2, for example in the case of the CCQE interaction, ν_μ interaction produces a proton but $\bar{\nu}_\mu$ interaction doesn't, that is to say, only μ^+ track can be seen in the $\bar{\nu}_\mu$ CCQE interaction. Moreover, the electronics for reading out the signal of MPPCs is different from the WAGASCI detector. We will use TFBs for the T2K INGRID detector[13], and EASIROC (Extended Analogue Silicon-pm Integrated Read Out Cip) modules[37]. The EASIROC (Fig.6.4.3) was developed by OMEGA in France, and is the ASIC for reading out the MPPC signal. It can readout 32 MPPC signals at once. The EASIROC module, as shown in Fig.6.4.4, consists of 2 EASIROCs, so it can read out 64 signals. It also includes the AMP, shaper, and discriminator, so the gain and signal shaping time of each MPPC can be controlled. MPPCs are connected to TFBs and EASIROCs with PCBs (Fig.6.4.5). The INGRID Water Module will be ready to install in the detector hall by the end of Mar. 2015 and then we will take the beam data for 1 month.

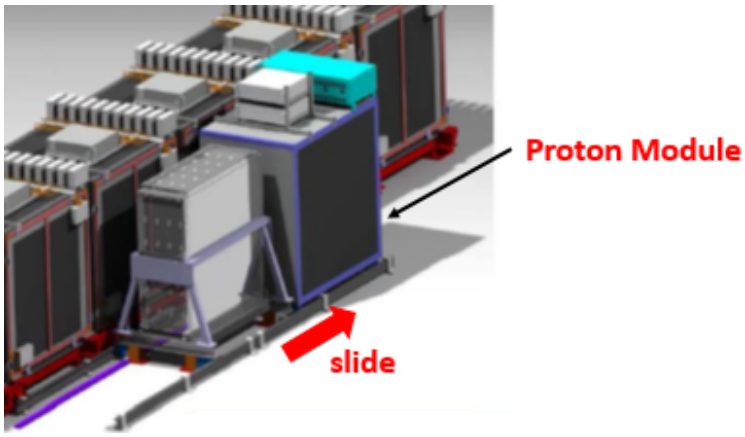

Figure 6.4.1: Candidate site of the prototype detector : The Proton Module will be slided for one INGRID module with the rail.

[13] They are spares for INGRID. The test operation has been done.

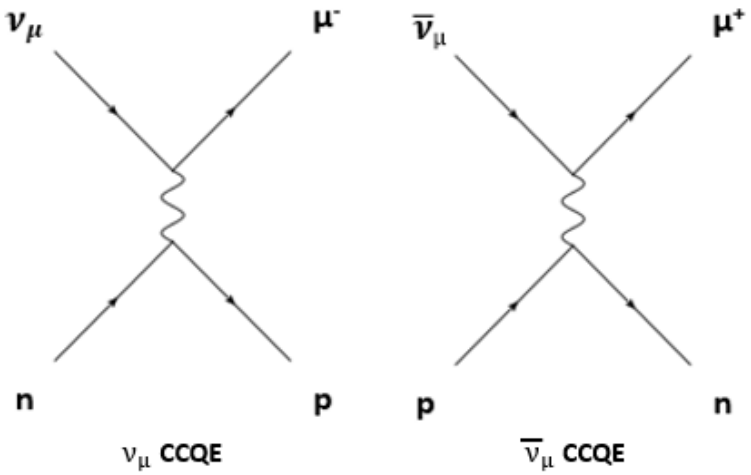

Figure 6.4.2: Diagram of ν_μ and $\overline{\nu}_\mu$ CCQE interaction

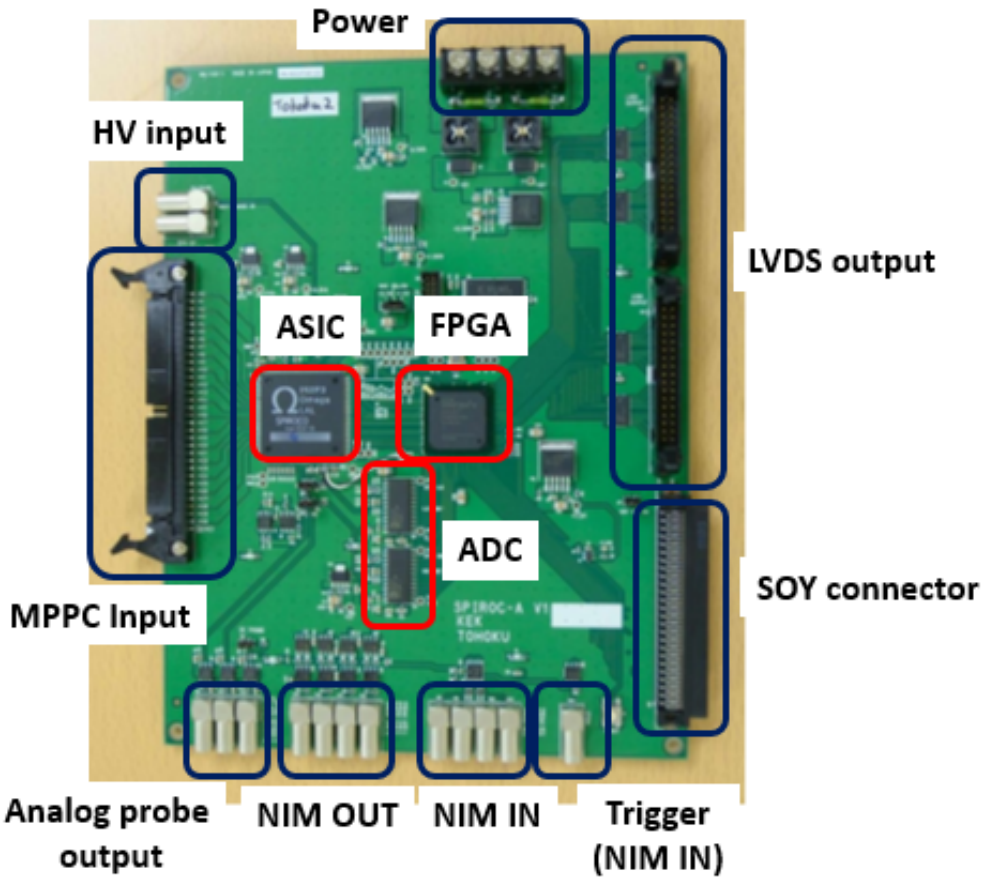

Figure 6.4.3: Overview of EASIROC

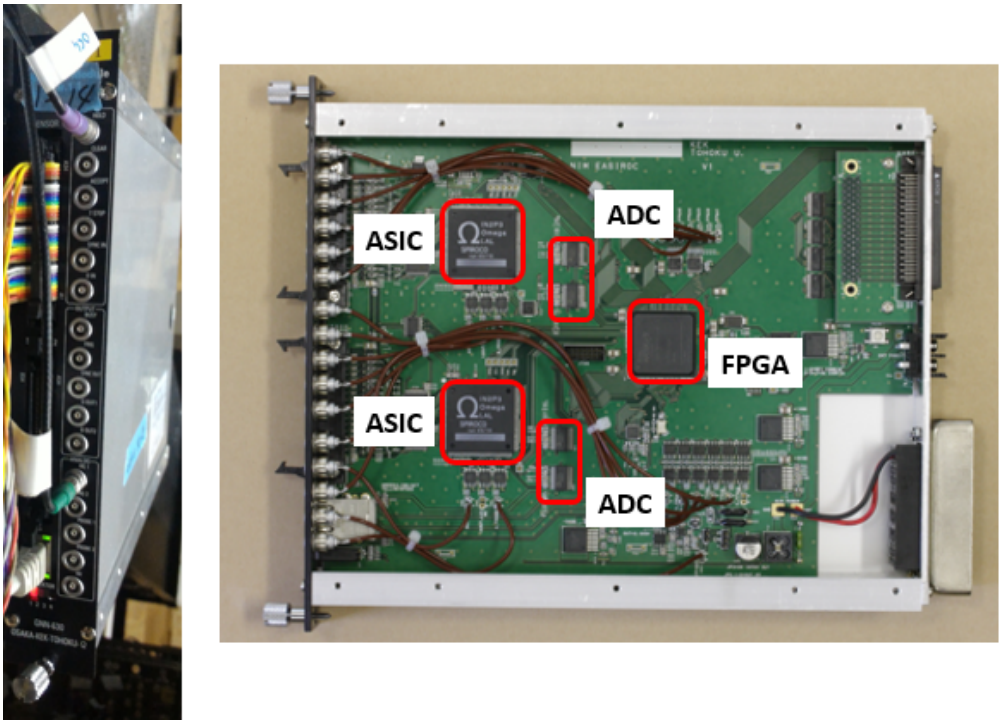

Figure 6.4.4: EASIROC module : The right picture shows the inside of the module.

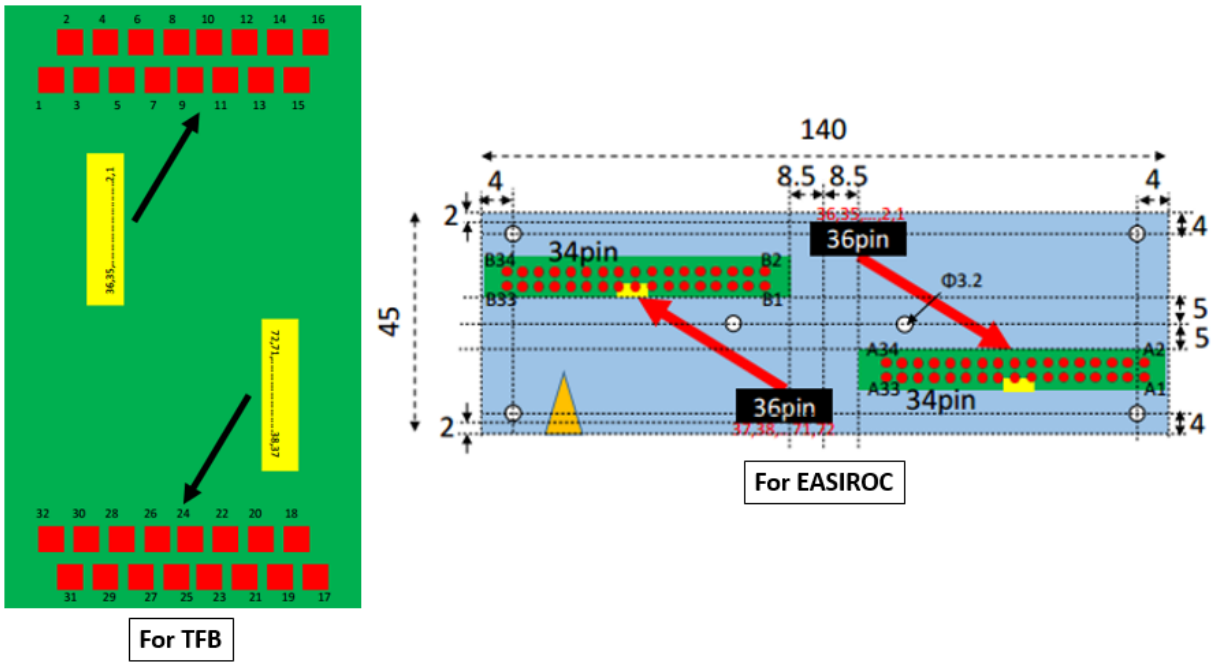

Figure 6.4.5: Design of PCB for connecting MPPC to TFB and EASIROC

Chapter 7

Construction work for the INGRID Water Module

7.1 Overview

Construction work was started in Oct. 2015 at the J-PARC NA building (Fig.7.1.1). Working members are from Osaka City University, INR[1], Kyoto University, LLR, University of Geneva, and University of Tokyo. We scheduled the shift and at least 6 people were working in NA.

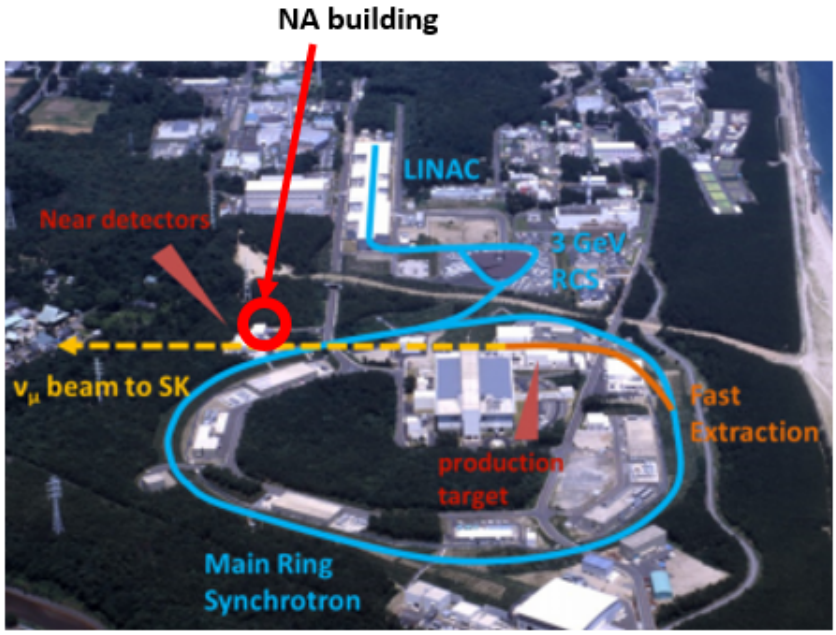

Figure 7.1.1: The site of the NA building in J-PARC : NA is the abbreviation for Neutrino Assembly.

[1]Institute for Nuclear Research of the Russian academy of sciencel, in Russia

7.2 Construction work

The construction work is mainly divided into 3 types : the fiber gluing work, reflector painting work, and assembly work.

7.2.1 Fiber gluing

This work was done by using the semi-automated gluing system (Fig.7.2.1). The detail of the system is described in Chapter 8. There were 3 cycles of this work[2], and in each cycle at least 2 people were assigned. In this work, WLS fibers were put into the groove of scintillators and glued with the optical cement. After gluing, it takes 24 hours for the cement to completely harden. 60 fibers and scintillators were glued per day.

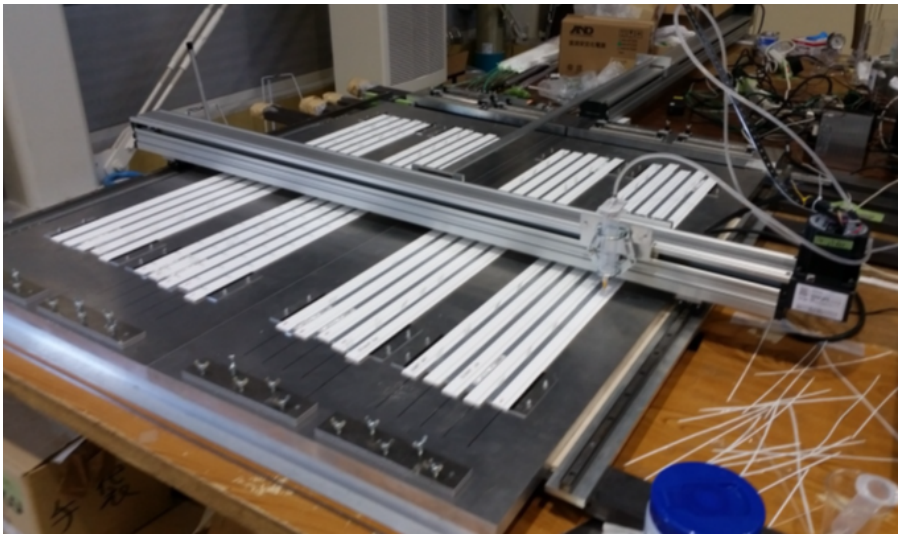

Figure 7.2.1: Overview of the semi-automated gluing system

7.2.2 Reflector painting

Before the fiber gluing work, we painted slits of scintillators with the white reflective coating, as shown in Fig.7.2.2. This is for preventing the crosstalk between scintillators in the grid structure. As mentioned in Sec.6.3.1, Avian-D, the two-part water based urethane coating, was used as the reflective coating, because it does not dissolve in the water[3]. Moreover, after the gluing work, fibers were also painted to reduce the crosstalk, as shown in Fig.7.2.3. In this work, 60 slits and fibers were painted per day.

7.2.3 Assembly

The assembly work also includes 3 procedures : the layer assembly work, sub-module assembly work, and module assembly work. There were two desks in the assembly space (Fig.7.2.4), so we could assemble two

[2] 9:00-10:30, 12:30-14:00, 17:00-18:30
[3] The water proof test was done in Kyoto University

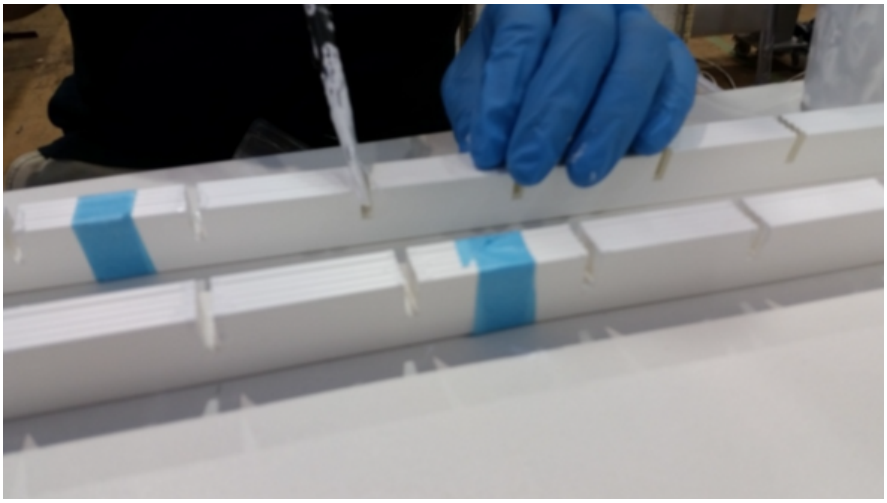

Figure 7.2.2: Slit painting work

Figure 7.2.3: Fiber painting work

layers in parallel.

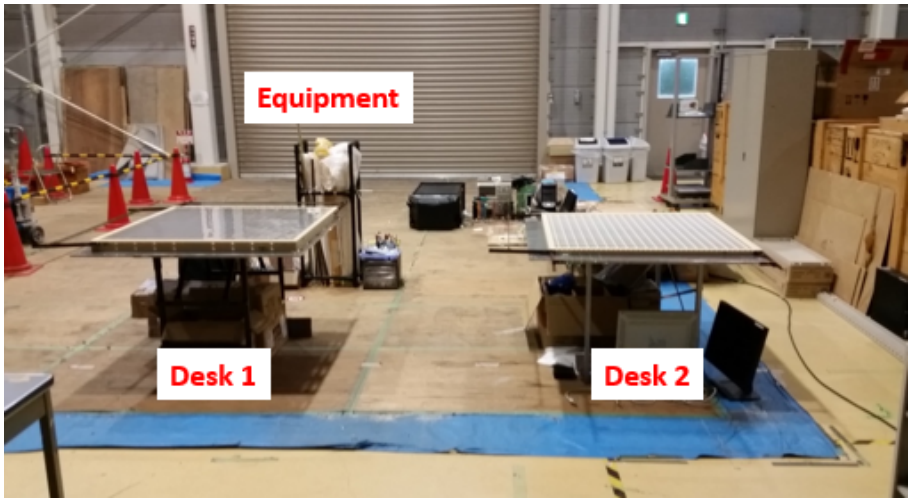

Figure 7.2.4: Space for the assembly work

- **Layer assembly**

  Procedures are as follows :

  1. Set the frame on the work desk (Fig.7.2.5)
  2. Set 20 grid scintillators on the frame (Fig.7.2.6)
  3. Set another 20 grid scintillators (Fig.7.2.7)
  4. Glue grid scintillators with the frame by the silicon glue (Fig.7.2.8)

Figure 7.2.5: Set frames : Materials are made by ABS resin

Figure 7.2.6: Set grid scintillators ①

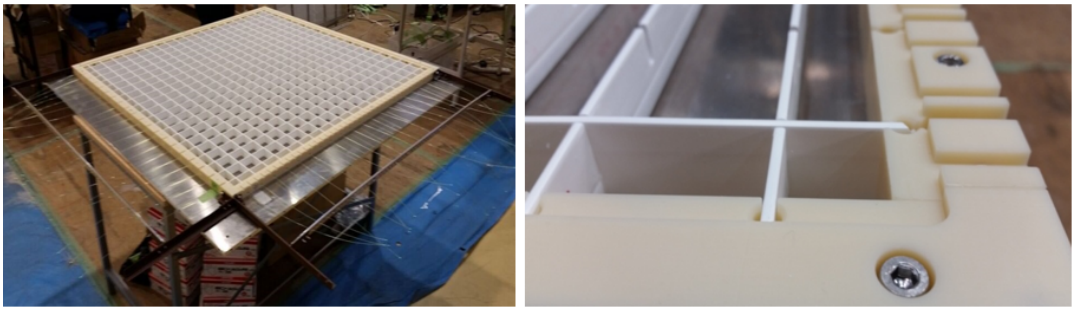

Figure 7.2.7: Set grid scintillators ②

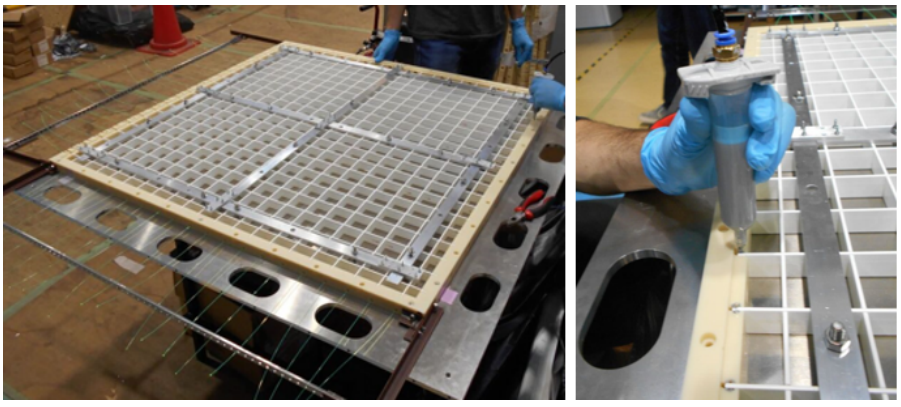

Figure 7.2.8: Glue scintillators with the frame : The aluminum frame is set to fix scintillators

It takes 24 hours for the glue to be hardened.

5. Set another 40 scintillators on grid scintillators and glue them by the silicon glue (Fig.7.2.9)

Figure 7.2.9: Set and glue scintillators on grid scintillators : These scintillators have no slit.

After the glue being hardened, the position of each scintillator was measured by a ruler (Fig.7.2.10).

These values are taken into account in the MC simulation.

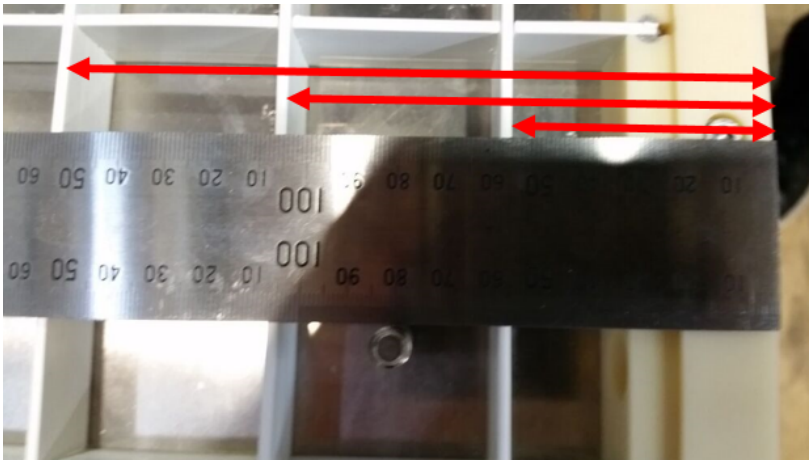

Figure 7.2.10: Measure each scintillator position : Measured points are between the right edge, center, left edge of each scintillator and the edge of the frame.

Through these processes, 16 layers were assembled.

- **Sub-module assembly**

Procedures are as follows :

1. Merge 4 layers to 1 sub-module (Fig.7.2.11)
2. Insert fibers to fiber bundles (Fig.7.2.12)
3. Cut extra fibers and glue them with fiber bundles by the optical cement (Fig.7.2.13)

In the 3rd procedure, we requested Daiichi-Tekko company to move 1 sub module, as shown in Fig.7.2.14. It is easier for fibers and fiber bundles to be glued in the condition that the sub-module is

Figure 7.2.11: Merge layers : The left figure shows 2 merged layers and the right shows 4 merged layers.

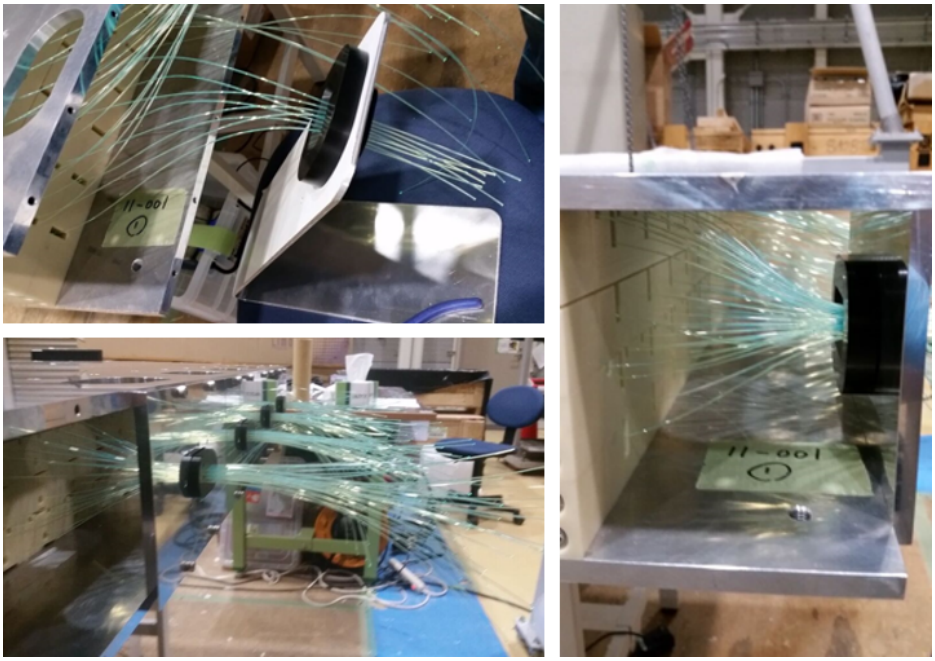

Figure 7.2.12: Insert fibers to the fiber bundle with some jig : Each hole in the fiber bundle corresponds to the active region of the MPPC.

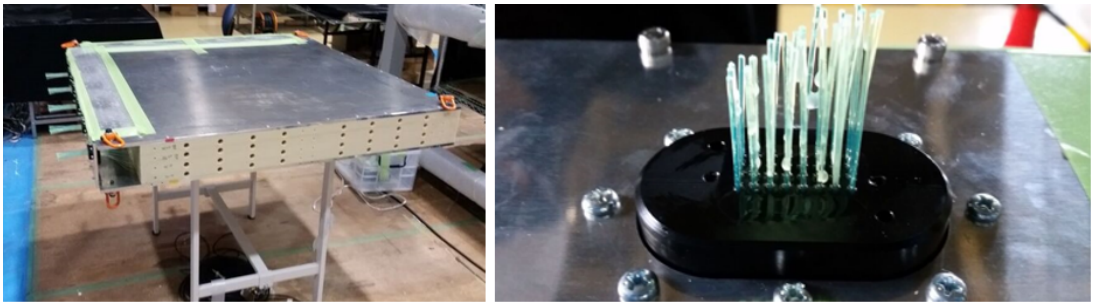

Figure 7.2.13: Cut fibers and glue them with the fiber bundle standing vertically.

After gluing, the sub-module was transported to Suzuno-Giken company in order for fibers to be polished, as shown in Figure.7.2.15. These procedures have been done for only 1 sub-modules at the present time.

- **Module assembly**

  4 sub-modules will be merged to 1 module. This assembly work is not done yet at the present time, and will be completed by the middle of Mar. 2016.

7.3 Near future schedule

After the construction work, we will install the INGRID Water Module into the water tank, and the performance test by cosmic-rays will be carried out. If the test goes well, MPPCs and TFBs will be connected to the module, and the prototype detector will be ready for taking the beam data by the end of Mar. 2016. During the beam-off timing, we will install the detector on the beam axis position in the detector hall.

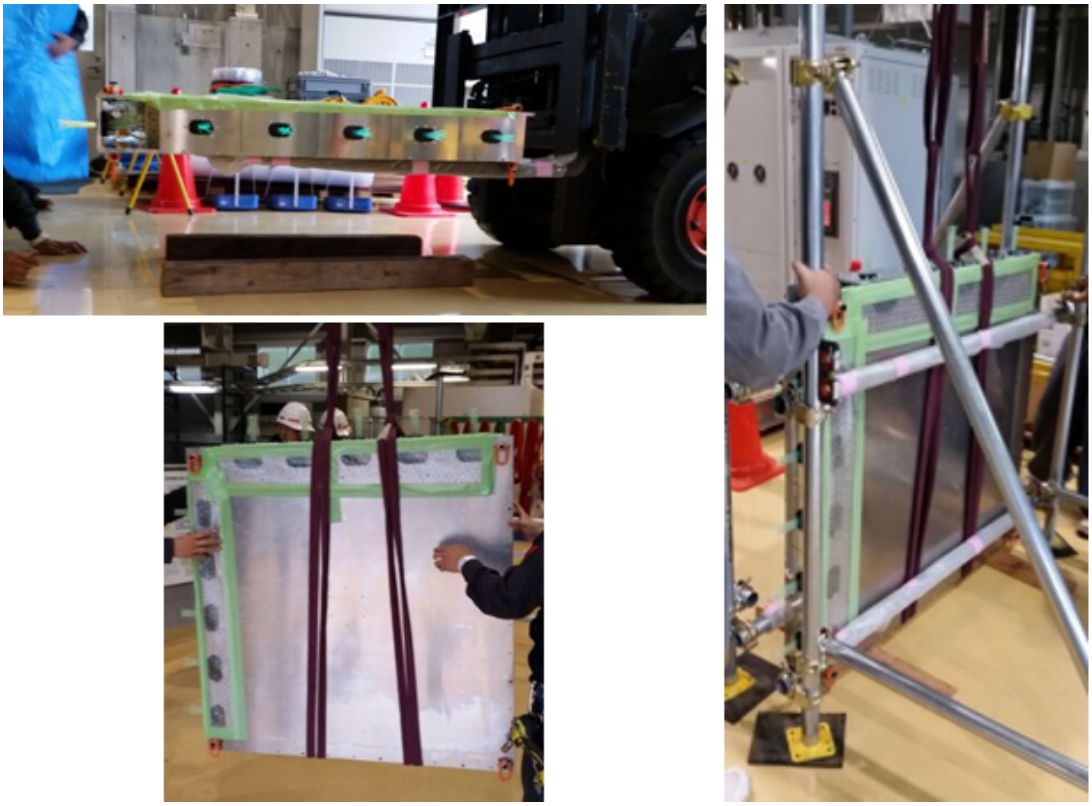

Figure 7.2.14: Pictures of the work by Daiichi-Tekko company

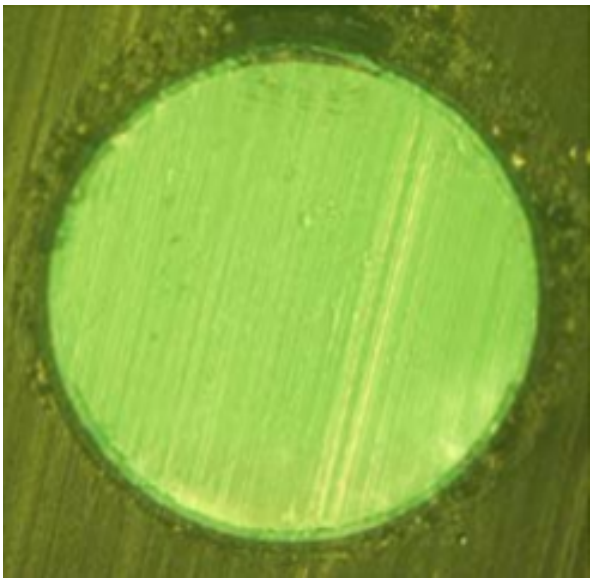

Figure 7.2.15: Cross sectional view of the polished fiber by the microscope of 200 magnifications.

Chapter 8

Development of the fiber and scintillator gluing system

8.1 Motivation

In order to mainly check the possibility for scintillators to be aligned in a 3D grid-like structure, we constructed a small prototype (pre-prototype) of the WAGASCI detector at Kyoto University (Fig.8.1.1). The construction work is described in Appendix B. The pre-prototype construction was completed well, but there was a problem. When we checked the light yield of scintillators, the variation was large, about 25%. The event display is shown in Fig.8.1.2, and result table is listed on Table.8.1.1. In the display, there are several scintillators which have a very low light yield. These scintillators have a certain characteristics that fibers are not correctly put into the groove of scintillators, as shown in Fig.8.1.3. In the construction process, we glued fibers with the groove of scintillators by the optical cement which is put on a toothpick, as shown in Fig.8.1.4. So, the amount of the optical cement was not constant, and the extra cement would float the fiber from the groove. This problem affects not only the precise measurement for the track reconstruction and particle identification, but also the alignment of a 3D grid-like structure. That is why we decided to develop a gluing system for gluing fibers and scintillators in order to keep the gluing quality.

Table 8.1.1: Result of the light yield measurement

Scintillator type	Mean light yield	RMS
w/ slit	26.56 p.e.	6.21 p.e.
w/o slit	26.59 p.e.	7.19 p.e.
All	26.58 p.e.	6.75 p.e.

8.2 System components

The gluing system consists of a lot of components. The main components are the optical cement, fiber fixing jigs, dispenser, and electrical actuator. In this section, other components are also described.

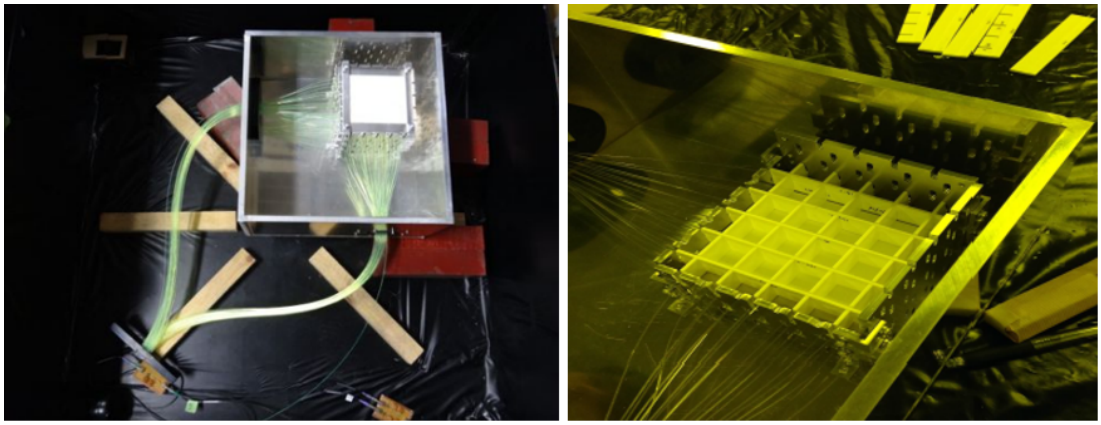

Figure 8.1.1: Pre-prototype

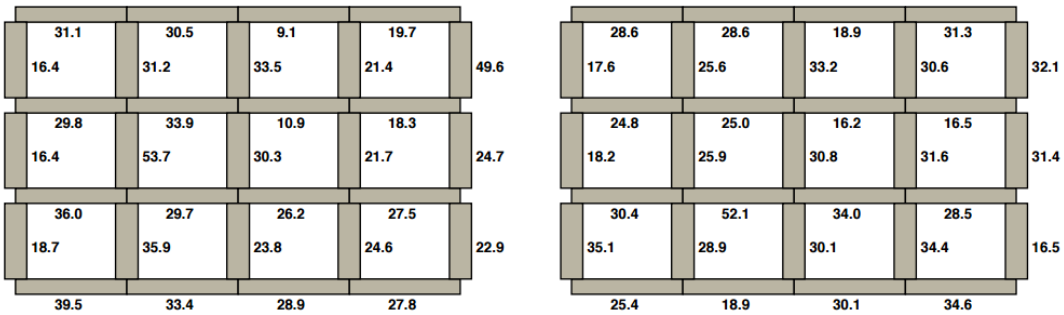

Figure 8.1.2: Event display for the light yield measurement

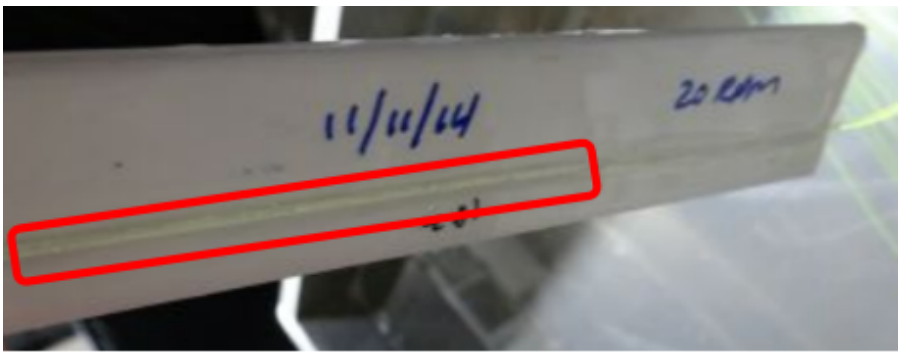

Figure 8.1.3: Gluing fiber and scintillator : In the red box, the fiber is a little floated from the groove of the scintillator.

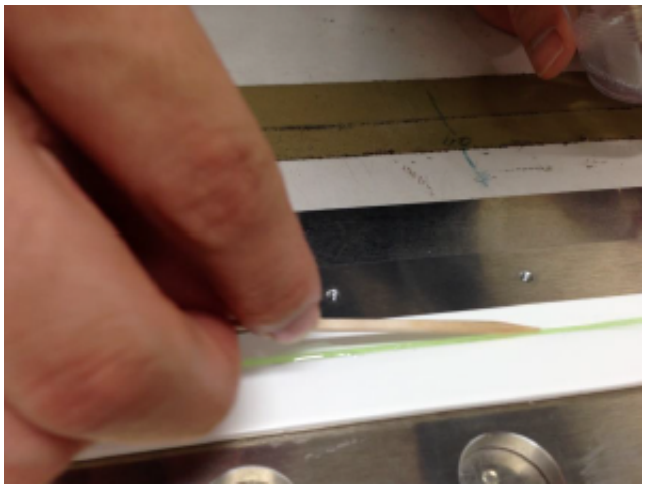

Figure 8.1.4: Gluing work with a toothpick

8.2.1 Optical cement

We use the optical cement, EJ-500. It is a two-part adhesive, the part A is a resin, and the part B is its hardener, as shown in Fig.8.2.1. Basically, we mix the resin and its hardener, and the weight ratio is 80% (resin) : 20% (hardener). In this condition, the cement takes 3-4 hours to set and 24 hours to harden. However, we tried to mix with different mass ratio, because we wanted for the cement to harden as quickly as possible in order to increase the gluing efficiency. It is desirable for the cement to go into the groove of scintillator sufficiently, so it is good to increase the wettability of it. We tested the mass ratio of 3.6 parts resin 1.4 parts hardener at the room temperature of 30 degrees. The test was done as shown in Fig.8.2.2. As a result, there was no difference in the time to harden and in the wettability between both conditions of mass ratio. On the basis of this result, we concluded to adopt the original mass ratio. The ratio 4 by 1 is easy to measure each weight, and there is no concern about a hardening failure of the cement which is caused by the extra hardener. Moreover, we evacuate bubbles in the optical cement using a sealed rotary vacuum pump and vacuum vessel (Fig.8.2.3). If they exist in the cement, it could also cause a decline of the adhesive strength. The change of the bubble state is shown in Fig.8.2.4.

8.2.2 Jigs for fixing the fiber

If the fiber is not tightened up correctly, the distance between the fiber and the groove of scintillator could fluctuate, and it would cause the light yield fluctuation. So, it is important how to fix it. We prepared two types of aluminum jigs (Jig 1 and Jig 2), and tested to fix the fiber with them, as shown in Fig.8.2.5.

- **Jig 1**

  Jig 1 is a fiber inserting type jig, as shown in Fig.8.2.6. There are 5 holes (ϕ = 1.5 mm). The fiber is inserted into the hole and fixed by thumbscrews, that is to say it is pushed by screws. This side of

Figure 8.2.1: Optical cement

Figure 8.2.2: Setup for the cement test : On a scintillator, the half of it was glued with the fiber in the mass ratio of 3.6 per 1.4, and the other side in the original mass ratio.

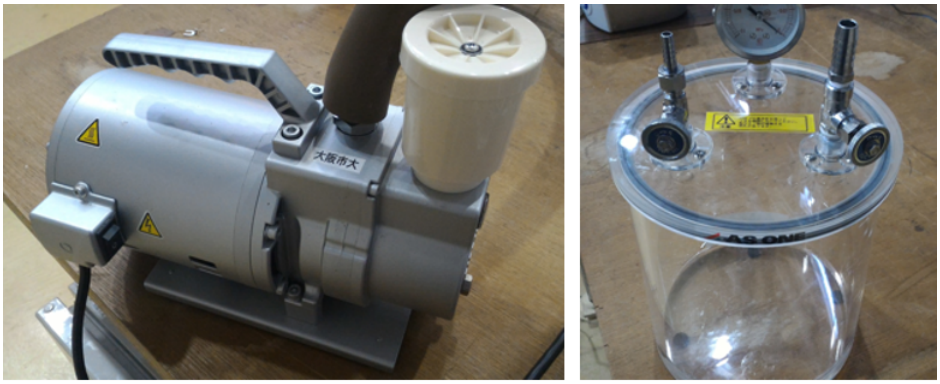

Vacuum pump Vacuum vessel

Figure 8.2.3: Vacuum pump and vessel

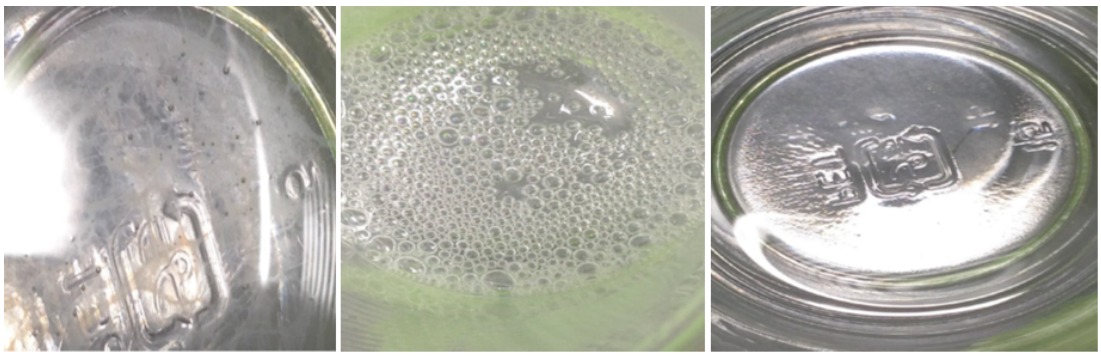

Initial state Intermediate state Final state

Figure 8.2.4: Change the bubble state in the evacuation

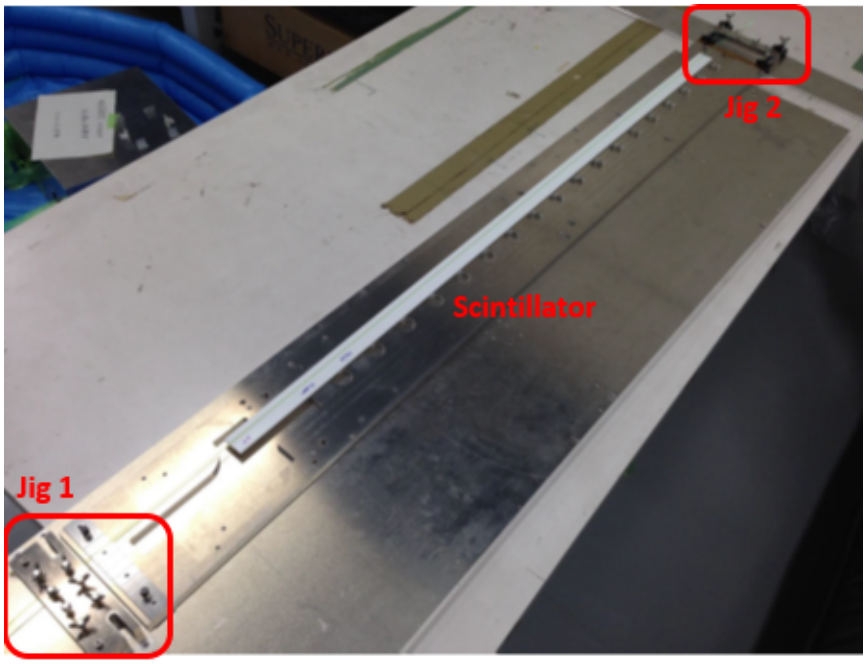

Figure 8.2.5: Setup for the fiber fixing test

fiber is cut after the gluing work, so the fiber can be damaged.

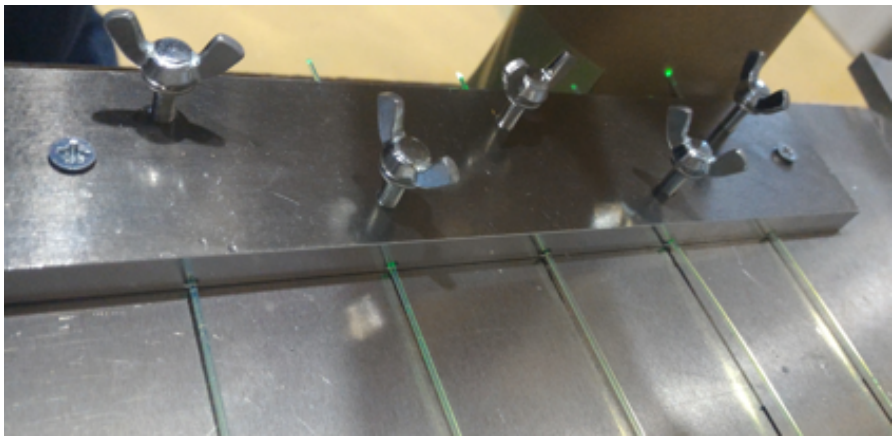

Figure 8.2.6: Jig 1

- **Jig 2**

Jig 2 is a fiber pressing type jig, as shown in Fig.8.2.7. The fiber is put on the groove of the jig, and then is pressed with the aluminum bar. This side of fiber is connected with MPPC, so it should not be damaged. That is why the jig like Jig 1 cannot be used, so we adopted the soft pressing type jig. In order to soften the fiber damage, we attached the rubber to each groove and aluminum bar. This increases the friction between the jig and fibers, so they can be fixed more tightly. The distance between each hole is 35 mm, so the gap between each scintillator is 10 mm.

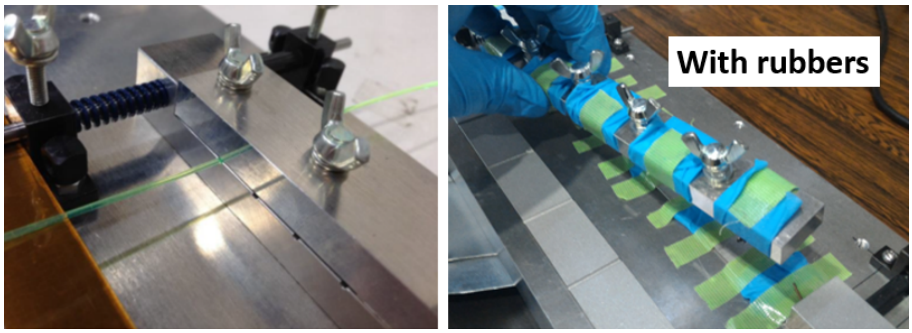

Figure 8.2.7: Jig 2

8.2.3 Dispenser

Using the toothpick causes the light yield fluctuation, so it should have been improved. At first, we tried to use DispensGun®[1](Fig.8.2.8). It enables us to control the discharged amount of the optical cement. Table.8.2.1 shows the result of the light yield measurement by cosmic-rays for scintillators which are glued with fibers by DispensGun®. The mean light yield is more than 10 p.e., and the fluctuation of the value

[1]DispensGun® was produced by Nordson EFD company

is about 9%. This result indicates that it is effective to use the tool for dispensing a certain amount of the cement. However, in order to discharge the optical cement, we had to continue to clasp the trigger of the gun, so it is very hard work. We concluded that we could not glue all WAGASCI scintillators with DispensGun®. Then, we had a try to use the dispenser[2] (Fig.8.2.9). Using this machine, the pressure and time to dispense can be adjusted. Moreover, it can be controlled by PC with serial communication. For, example, if we want to dispense the optical cement, control characters we should send to the dispenser is [ENQ stx 04DI__CF etx EOT], and we have to replace them with ASCII [\x05\x02\x30\x34\x44\x49\x20\x20\x03\x04]. We made a shell script to control it continuously in order to dispense the optical cement on a lot of scintillators efficiently. By the way, the optical cement is filled in the syringe (Fig.8.2.10) which is connected to the dispenser with the tube, and is dispensed from the nozzle attached to the syringe. Moreover, the plunger is used in order to protect the dispenser from the reverse flow of the cement.

Figure 8.2.8: DispensGun® : The light figure shows the nozzle for discharging the optical cement.

Table 8.2.1: Result of light yield measurement : Scintillators are glued with fibers by DispensGun®

Scintillator	Mean light yield	RMS
w/o grid	11.58 p.e.	1.08 p.e.

Figure 8.2.9: Dispenser : The right figure shows the control panel.

[2]We use the dispenser produced by Musashi Engineering, company

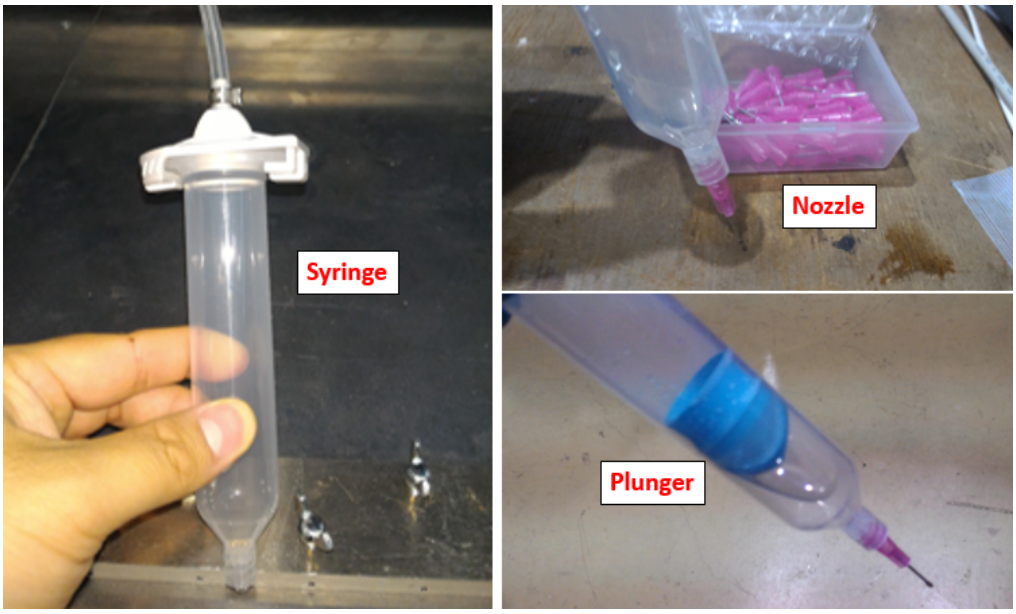

Figure 8.2.10: Syringe

8.2.4 Electrical actuators

The electrical actuator[3], as shown in Fig.8.2.11, is used to move the syringe filled with the optical cement automatically. It can move only linearly, so we combined two actuators in order to enable the syringe to move two-dimensionally by pushing and pulling one side of actuators with an aluminum bar. They are controlled by PC as same as the dispenser, and the command is also written in the shell script. The syringe is attached to the slider on the actuator. At first, we tried to set it with a wire, as shown in Fig.8.2.12, but this setup easily got the swing and the edge of the syringe fluctuated. The nozzle has to be just above the groove of the scintillator, so it was a problem. Then, we attempted to fix it more firmly with some jigs, as shown in Fig.8.2.13. It was strong to the swing, so we adopted this method.

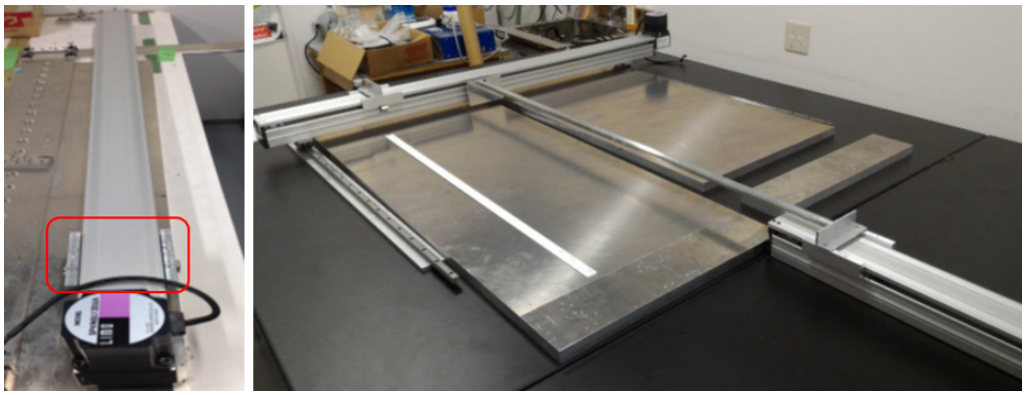

Figure 8.2.11: Electrical actuator : The syringe is attached to the slider in the red box.

[3]We use the electrical actuator produced by Oriental Motor company

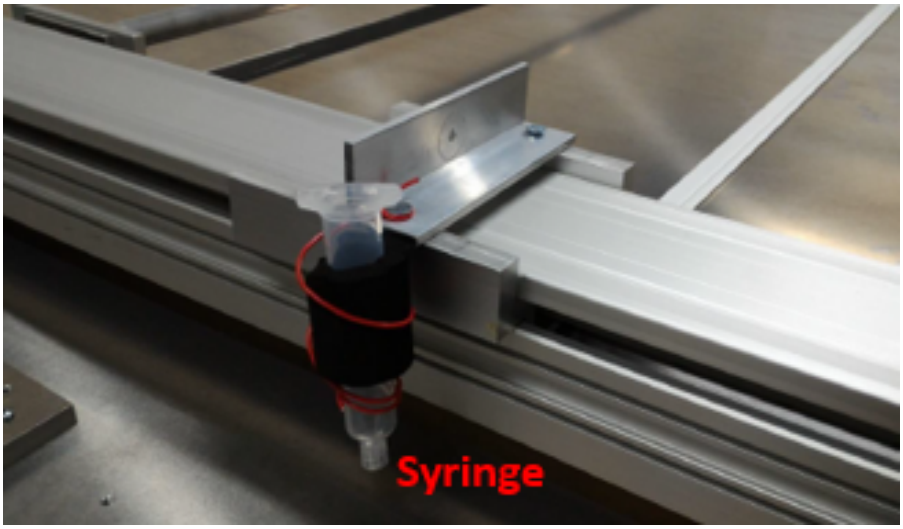

Figure 8.2.12: Setting the syringe on the actuator slider with a wire

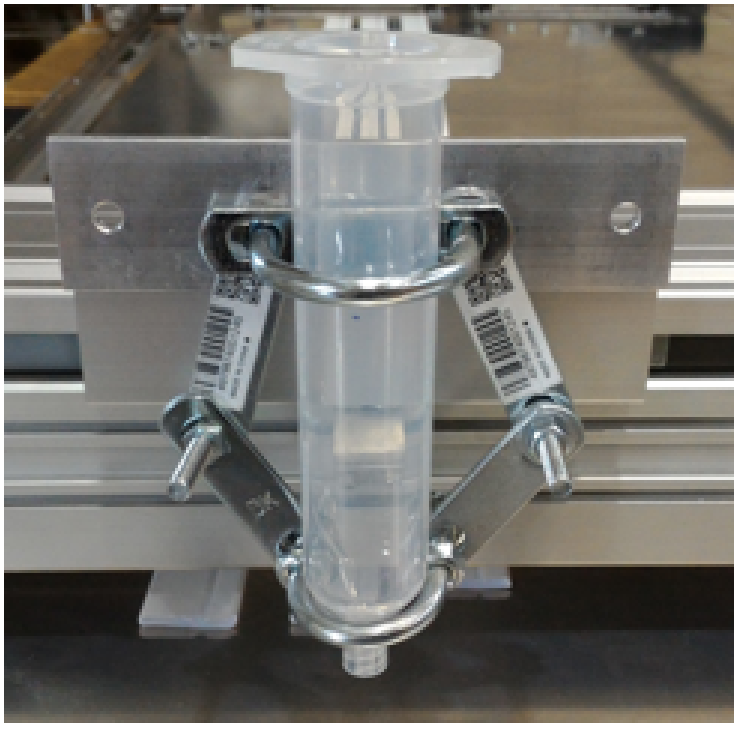

Figure 8.2.13: Fixing the syringe with some jigs

8.2.5 Other components

There are also other components in the gluing system.

- **Aluminum board**

  This is for setting scintillators. The size of it is 110 cm × 130 cm, and the thickness is 2.5 cm. On this board, 20 scintillators can be set at once.

- **Air compressor**

  This compressor[4] (Fig.8.2.14) is needed in order to supply compressed air to the dispenser. In the gluing work, the air pressure is kept about 0.6 MPa.

Figure 8.2.14: Air compressor : The right figure shows the connection with the dispenser.

- **Controller for the electrical actuator**

  There are two types of controllers for the actuator, as shown in Fig.8.2.16. One is connected to the actuator and another is connected to PC. They are also connected with the cable, and send the command from PC to actuators. The actuator key is attached to the former controller in order to identify the controlled actuator. Both of them are connected to the power supply of which the output is 24V (< 0.5 A). Power supplies are shown in Fig.8.2.17.

- **Linear guide**

  In order to guide the actuator to move linearly, linear guides are set on both edge of the actuator, as shown in Fig.8.2.15. It is a 130 cm long, and is fixed on the aluminum board with some screws.

- **PC**

  PC (Fig.8.2.18) is used to operate the dispenser and electrical actuators. The original OS is Windows type, but Linux OS is invited by the Virtualbox software. The shell script is in the virtual OS, so they are controlled with the Linux serial communication.

[4]We use the air compressor produced by Hitachi company

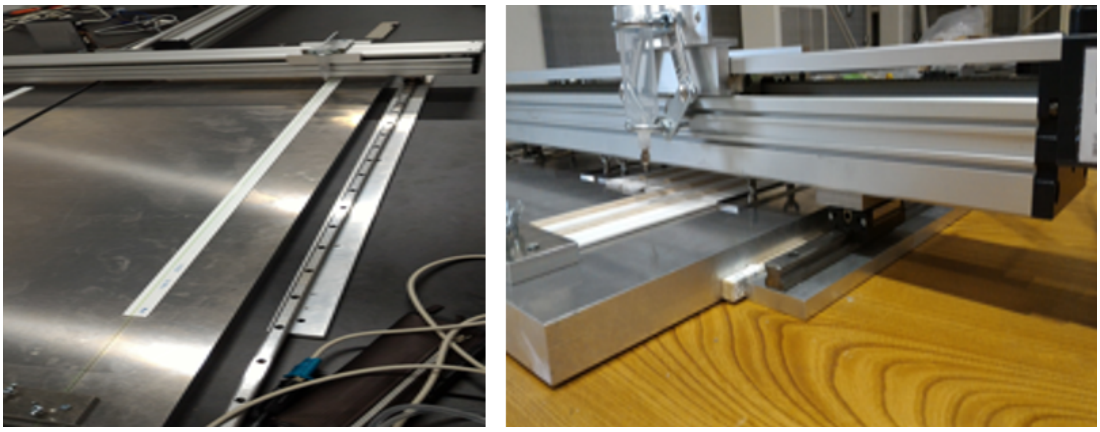

Figure 8.2.15: Linear guide

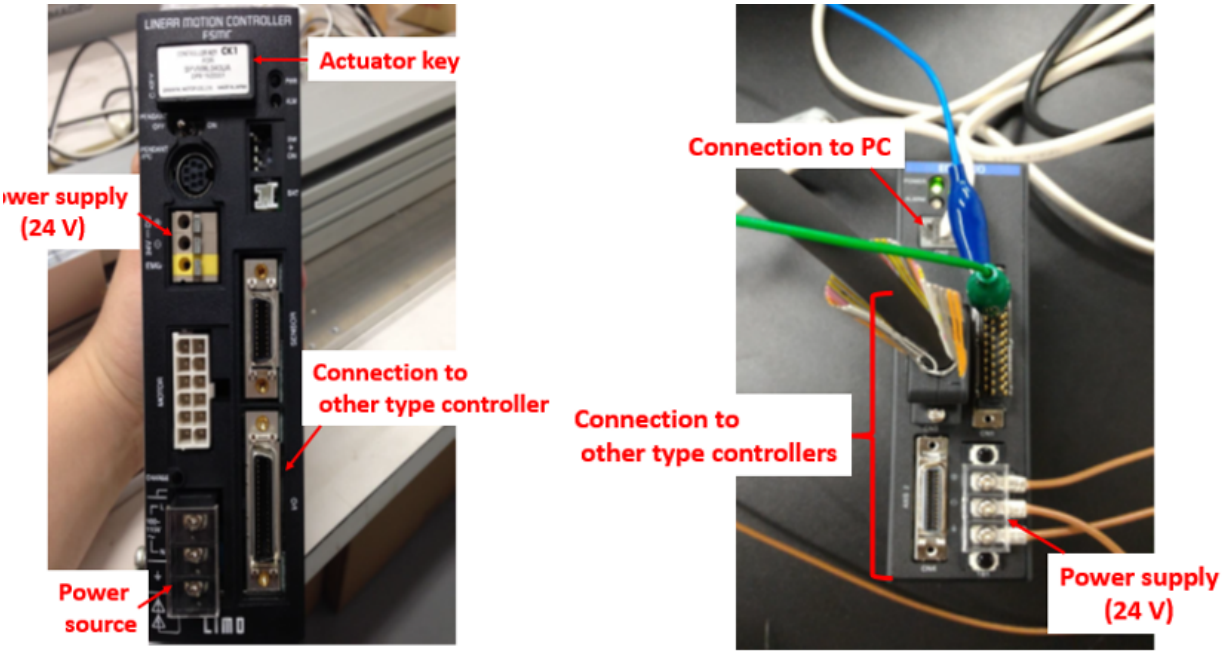

Figure 8.2.16: Two types of controllers : The left side of controller is connected to the outlet as a power source.

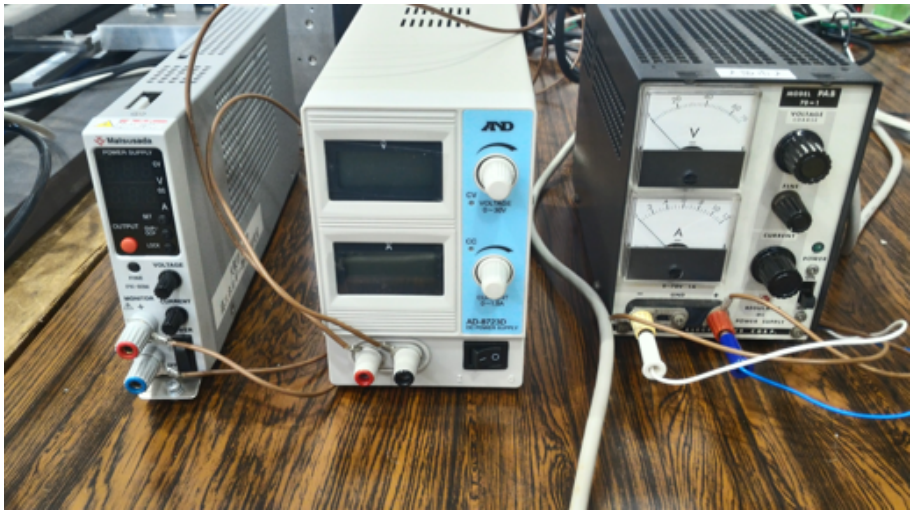

Figure 8.2.17: Power supplies for controllers

Figure 8.2.18: PC

8.3 Optimization of the gluing system

Once all the components were completed, we started to set and optimize the gluing system at J-PARC NA building from the middle of Aug. 2015. Overview of the gluing system is shown in Fig.8.3.1.

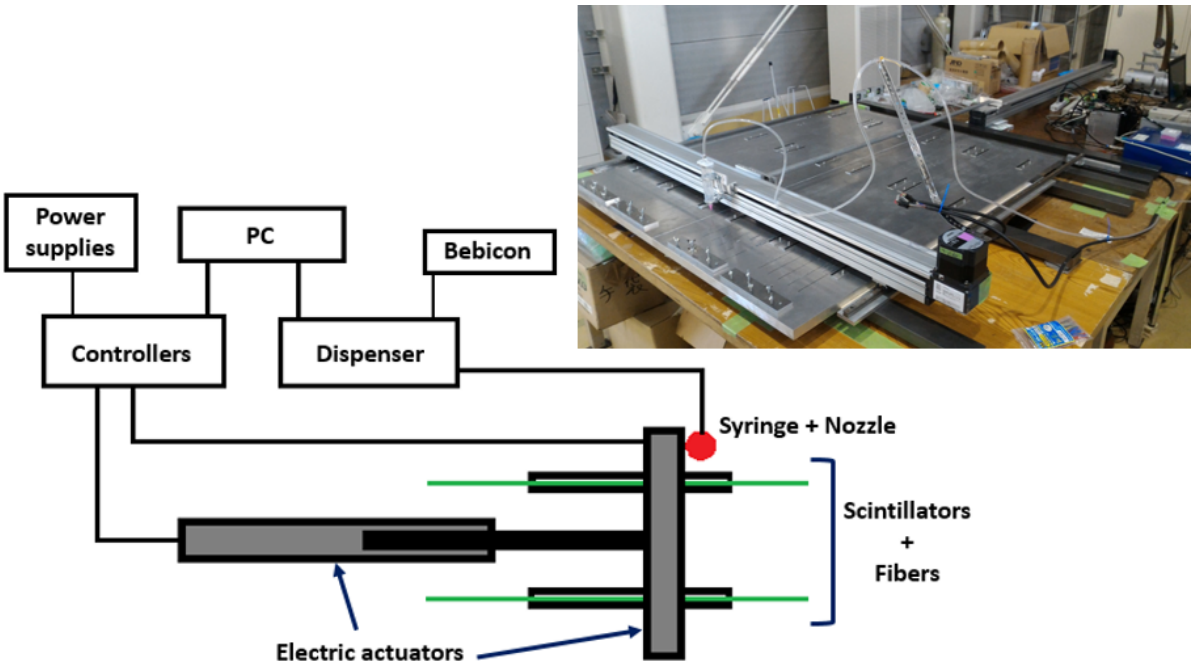

Figure 8.3.1: Overview of the gluing system

8.3.1 PC control

At first we confirmed that the dispenser and two electrical actuators are properly operated by only 1 PC with the shell script. As to the Linux PC, it was failed to control both implements due to the serial problem. One of the connector in the PC had some problems, and we could not send commands. On the other hand, we replaced the PC to the Windows PC with virtual Linux OS, then the control was succeeded. So, we decided to use the virtual Linux OS.

8.3.2 Fixing scintillators

As shown in Fig.8.3.2, the WAGASCI scintillator turned out to be distorted by about 1 cm. It was a serious problem because the nozzle can move only linearly. So, we made jigs for fixing scintillators straight, as shown in Fig.8.3.3. In this method, we set 10 mm spacers between each scintillator, and pinch all of them together by aluminum bars. Thanks to these jigs, the distortion of them was corrected.

8.3.3 Distancing between the nozzle and the fiber

Figure 8.3.2: WAGASCI scintillator : It is a slightly distorted.

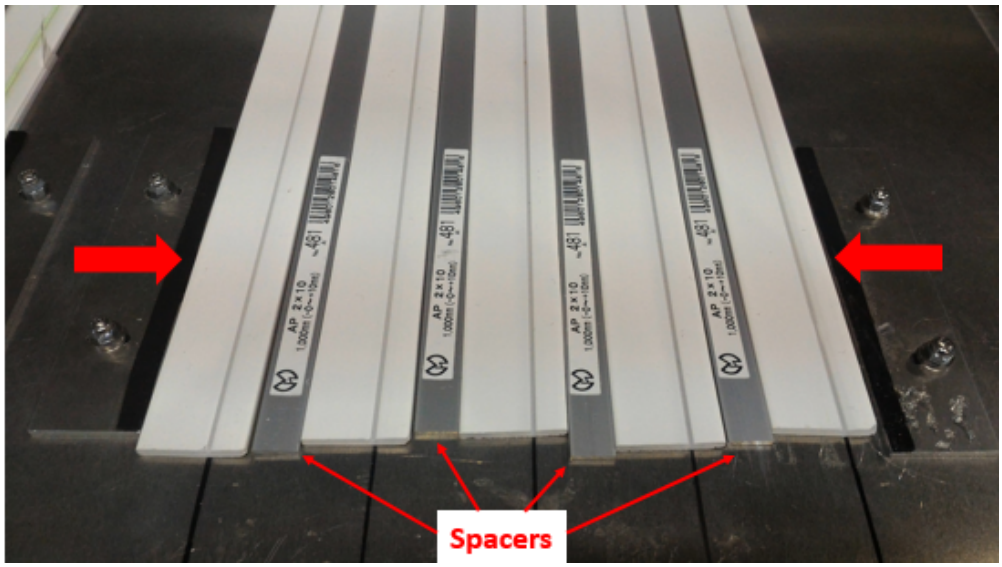

Figure 8.3.3: Jigs for fixing scintillator linearly

If the nozzle attached to the dispenser syringe is apart largely from the fiber put into the groove of the scintillator, the point where the optical cement should be dispensed easily fluctuates. The width of the groove is very narrow, 1 mm, so it is a problem. On the other hand, if the gap between the nozzle and the fiber is very small, in turn the fiber could be damaged by the tip of the nozzle. That is why it is important to decide the initial position of the nozzle. We repeatedly tested a variety of gap, and it turned out that 0.2 mm was the best. Taking this result, we prepared the 0.2 mm thickness aluminum board, and decided to adjust the distance by putting the board between the nozzle and the fiber, as shown in Fig.8.3.4.

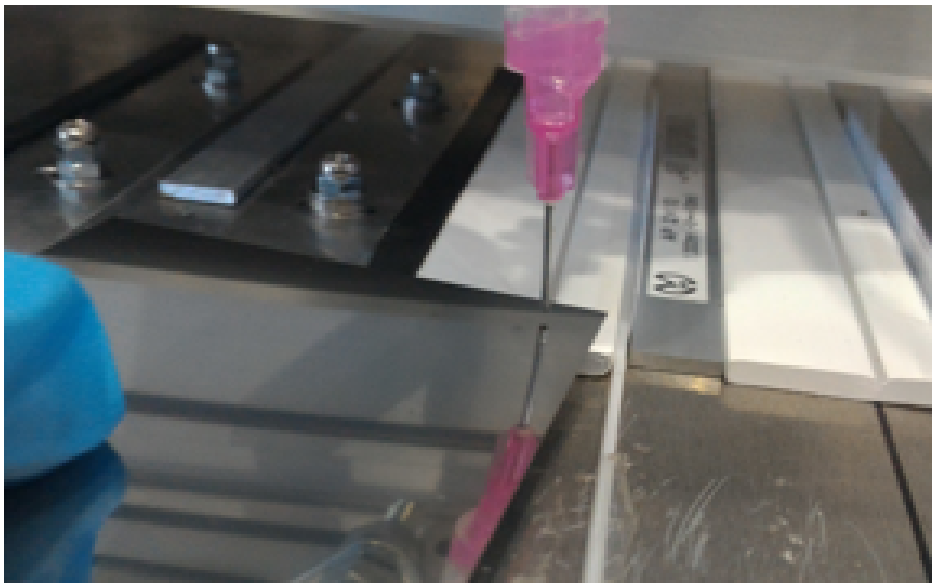

Figure 8.3.4: Aluminum board for adjusting the gap between the nozzle and the fiber

8.3.4 Pressure of the dispenser and velocity of the electrical actuator

If the pressure of the dispenser and the velocity of the actuator is not appropriate, the discharged amount of the optical cement could be excess or too short. The excess amount of the cement would cause the impossibility of aligning the grid structure, and too short would cause the separation of the fiber and scintillator easily. So, it is important to set the apposite pressure and velocity. We at first determined the pressure of the dispenser. Then, we found that around 200 MPa is a best value in the tested pressure, and it is almost corresponding to the dispensing speed 0.15 g / 3 s[5]. So, we determined that we should calibrate the discharging speed to 0.15 g / 3 s before the gluing work. After that, we tested the gluing work under a variety of velocity conditions as shown in Fig.8.3.5, at a calibrated pressure. The velocity of 7 m/s turned out to be the appropriate value. Finally, we concluded that the velocity of the actuator is set as the fixed value in the shell script, and we change the pressure of the dispenser according to the calibration of the discharging speed. In addition, the capacity of the syringe and the gauge of the nozzle is determined. The former is 30

[5] 1 s is too short to precisely measure the amount of the discharged cement, so we set the dispense time to 3 s.

ml, and the latter is 18G[6].

Figure 8.3.5: Test gluing work under a variety of velocity conditions

8.3.5 Leveling the aluminum board

As mentioned in Sec.8.3.3, the distance between the nozzle and the fiber is very important. However, when we checked the gluing system operation, it was found that the distance is not constant along the scintillator, and that the desk where we set the system was a little dented. So, we put iron bars between the desk and the aluminum board as leveling blocks, as shown in Fig.8.3.6. After setting these blocks on the desk, the problem was completely solved.

Figure 8.3.6: Leveling blocks : The right figure shows the spirit level for setting the block on the desk.

8.4 Gluing work in the detector construction

After the optimization of the gluing system, we started to operate it for the construction work.

8.4.1 Procedure

In this section, the procedure for the system operation is described in sequence. This gluing work is done by more than 1 person, as mentioned in Sec.7.2.

- **Warming-up for the dispenser**

  In order to dispense the optical cement stably, it is necessary to do the warming-up operation of

[6] 18G corresponds to the edge diameter of 1.2 mm

the dispenser while being connected with the air compressor. At first, all bulbs (Fig.8.4.1) on the air compressor should be confirmed to be closed, and then we turn on both the dispenser and air compressor. When the air pressure in the air compressor is up to 0.8 MPa, the operation of the compressor is automatically stopped, and then the air bulb is opened. After opening it, when the air pressure is down to 0.6 MPa, the operation is automatically restarted. Thereafter the pressure repeats raising and lowering, and on this condition we wait to start using the dispenser at least for 30 minutes.

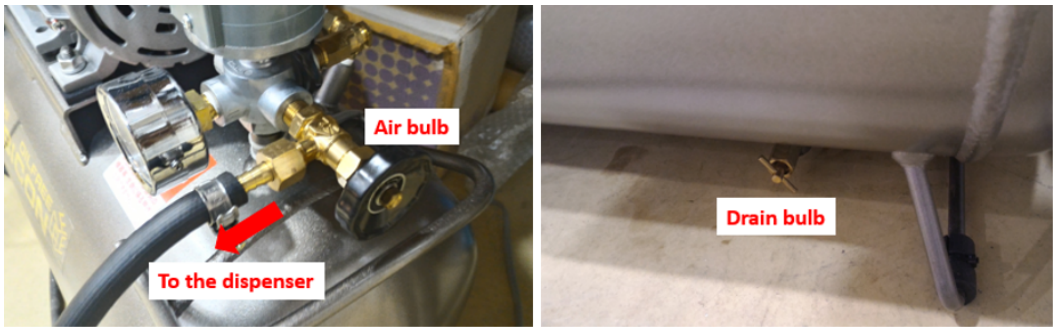

Figure 8.4.1: Bulbs on the air compressor

- **Setting scintillators**

Before setting scintillators, they should be wiped with the ethanol in order to prevent them from the dust, especially on the groove. After that, we put scintillators between aluminum bars, and then, we put spacers between each scintillator, as shown in Fig.8.4.2. Lines which indicate the position of fibers are drawn on the aluminum board, and each groove position is set to match with the line.

Figure 8.4.2: Setting spacers between scintillators

- **Setting fibers**

As the scintillator case, at first fibers should also be cleaned by the ethanol before setting them on the groove of scintillators. Secondly, one side of fibers is inserted into holes of Jig 1 and are pressed with screws, and then, other side of fibers are passed into holes of Jig 2 and are fixed by aluminum bars, as shown in Fig.8.4.3. After that, we temporary loosen screws in order for fibers to be moved freely, and pull fibers to strain them. If it is O.K., we tighten screws again. Finally, films are put

on fibers, as shown in Fig.8.4.4. If there is no film, the optical cement could drop on the aluminum board, and fibers could be glued to the board.

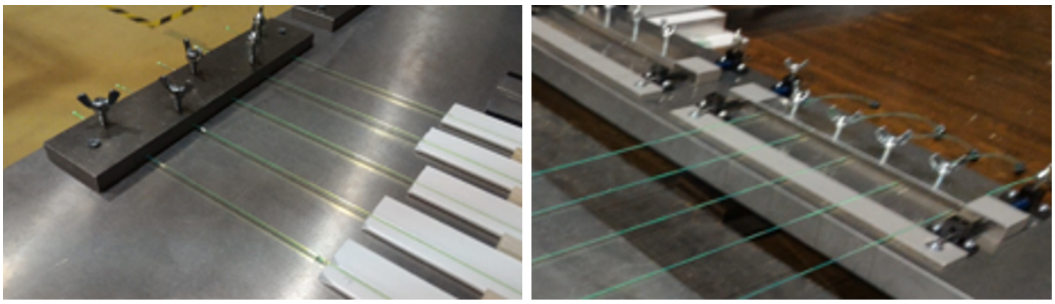

Figure 8.4.3: Fixing fibers with jigs

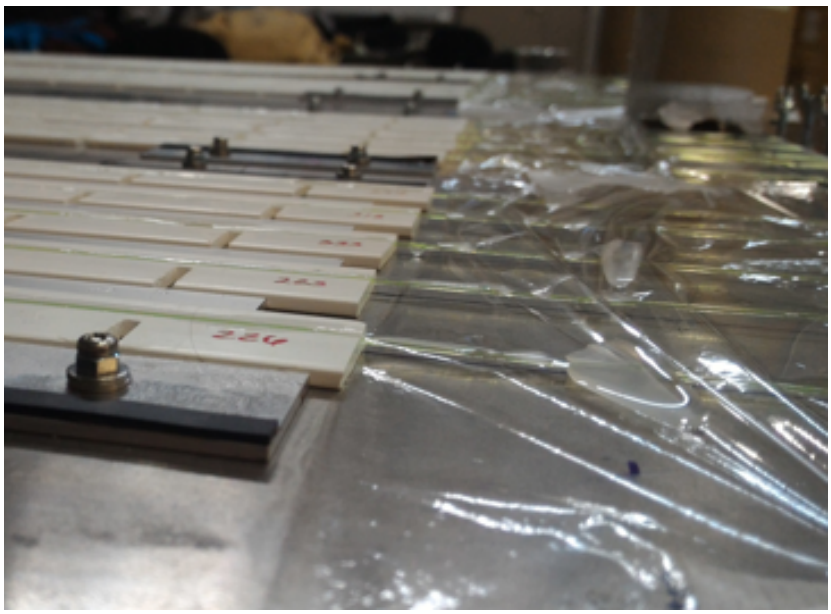

Figure 8.4.4: Putting films on fibers for preventing the cement from dropping

- **Making the optical cement**

During the fiber setting, 1 person makes the optical cement. The weight of the resin (24 g) and its hardener (6 g) are measured, and they are mixed for about 3 minutes. Then, in order to reduce bubbles, the cement is evacuated for about 5 minutes.

- **Calibration**

After making the optical cement, we fill it into the syringe and set the nozzle and plunger. Then,

we calibrate the dispensed amount of it. The discharge pressure is adjusted corresponding to the dispensing speed 0.15 g / 3 s. When the calibration is finished, the dispense time of the dispenser has to be changed into 21 s[7] for the system operation, as shown in Fig.8.4.5.

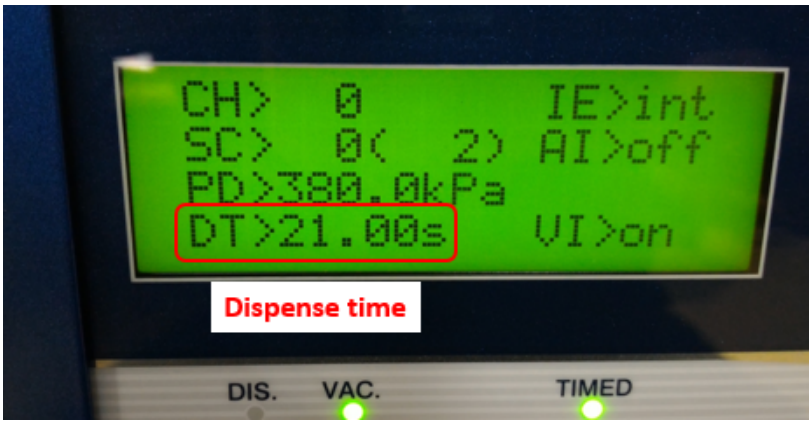

Figure 8.4.5: Setting dispense time for the gluing system

- **Test operation**

  While making the cement, another people confirm that both the dispenser and actuator can be controlled by PC properly. If there are some problems, we try to find solutions, such as rebooting the PC. If problems cannot be solved soon, we cancel the system operation in this cycle and dedicate to fix it.

- **Setting syringe**

  When the calibration and test operation are completed, the syringe filled with the cement is attached to the slider of the electrical actuator, as shown in Fig.8.2.13. Then, the nozzle height from the fiber is adjusted, as shown in Fig.8.3.4.

- **Gluing system operation**

  After all the preparation work are finished, the system operation is started. All we have to do is to enter in the Linux terminal the command for reading the shell script. During the system operation, we should pay attention to the system behavior. If there are any problems, for example the optical cement is not discharged from the syringe, we stop the system as quickly as possible. If there is no problem, it takes about 10 minutes to glue 20 fibers with scintillator grooves. Finally, the cover is set above scintillators, as shown in Fig.8.4.6, in order to protect scintillators and fibers from the dust.

- **Replacing scintillators**

  We operate the gluing system 3 times per day, as mentioned in Sec.7.2, so we have to replace scintillators. It takes about 3 hours for the optical cement to set, so we do this replacing work 3

[7] It takes about 21 s for the nozzle to move along the scintillator.

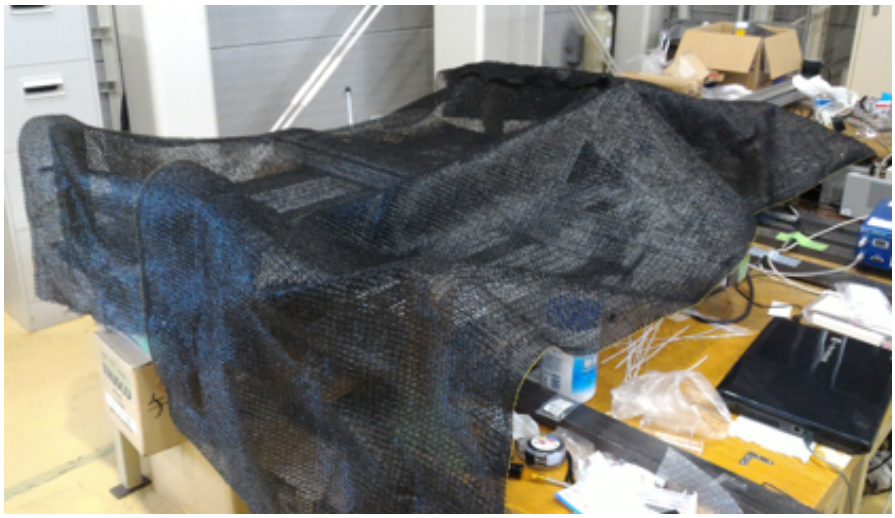

Figure 8.4.6: Cover

hours later from the end of the gluing work at 1 cycle. At first, we put curing tapes on the edge of scintillators in order to prevent fibers from floating from the groove of scintillators, and then, fibers on the Jig 1 side are cut, as shown in Fig.8.4.7. Fibers on the other side are not cut because they are connected with MPPCs. When the cutting work is finished, scintillators are moved to another desk for waiting the cement to harden, and new scintillators are set on the aluminum board.

Figure 8.4.7: Cutting fibers

8.4.2 Time schedule

Fig.8.4.8 shows the flowchart and rough time schedule of the gluing system operation. For the gluing work, it takes about 4.5 hours to do 1 cycle. We scheduled 3 shifts : 9:00-12:30, 12:30-17:00, 17:00-18:30[8], and we can set 20 fibers and scintillators at 1 cycle, so 60 fibers and grooves of scintillators are glued per day. The gluing work was started from the beginning of Oct. 2015 and was finished on the end of Nov. 2015. During this period, we have finished gluing about 1400 fibers and scintillators. 1280 is for the INGRID Water Detector construction, and the remnant is for the spare.

[8] After the last cycle, it is not necessary to replace scintillators, so we do not have to wait the optical cement to set.

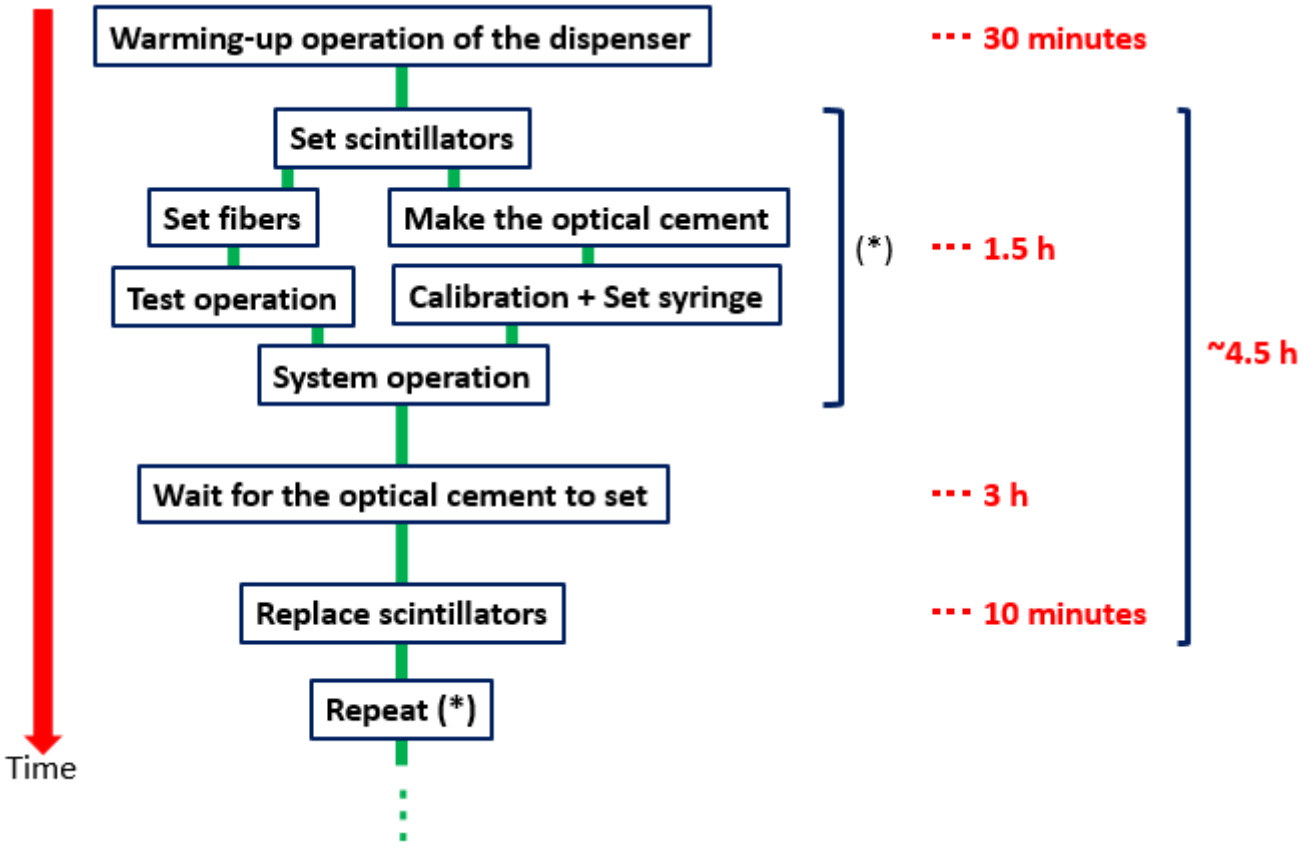

Figure 8.4.8: Flowchart of the gluing system operation

Chapter 9

Measurements for the WAGASCI scintillator

9.1 Measurements of the dimension

During the construction period, we measured a variety of parameters of WAGASCI scintillators. It was for understanding how many differences there are in each scintillator, and for take such differences into account in the MC simulation. Parameters of scintillators we measured are as follows : the width, thickness, weight, and density.

9.1.1 Width

We used a caliper for the measurement. Fig.9.1.1 shows points we measured and the average was defined as its width. We measured for 25 scintillators, and Table.9.1.1 shows the measurement result, and ① to ③ have almost the same mean value. Although we assumed that the width of the scintillator is 2.5 cm, it turned out that the width is a little smaller. This shortness affects to the assembly work, especially the scintillator setting work. So, we put spacers between each scintillator, as shown in Fig.9.1.2, in order to cover the fiducial region by scintillators.

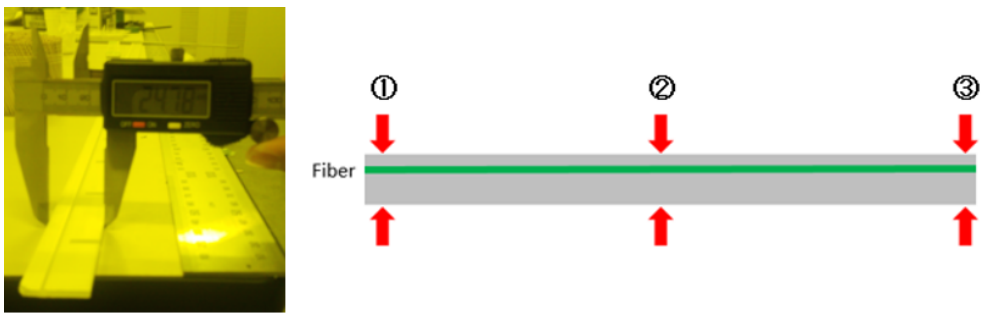

Figure 9.1.1: Width measurement

Table 9.1.1: Result of the width measurement

Position	Width	RMS
①	2.45 cm	0.07 cm
②	2.45 cm	0.08 cm
③	2.44 cm	0.08 cm
All	2.45 cm	0.08 cm

Figure 9.1.2: Put spacers between each scintillator

9.1.2 Thickness

The thickness of the scintillator was measured by a micrometer. Fig.9.1.3 shows measured points, and the average of them are defined as its thickness. The result is shown in Table.9.1.2. The thickness of ② has a little larger mean value than other points, and this result indicates that the scintillator is not flat, as shown in Fig.9.1.4. This distortion might be caused due to the groove cutting in the scintillator production process. However, the difference is so small that it can be negligible in the construction work, such as the gluing work.

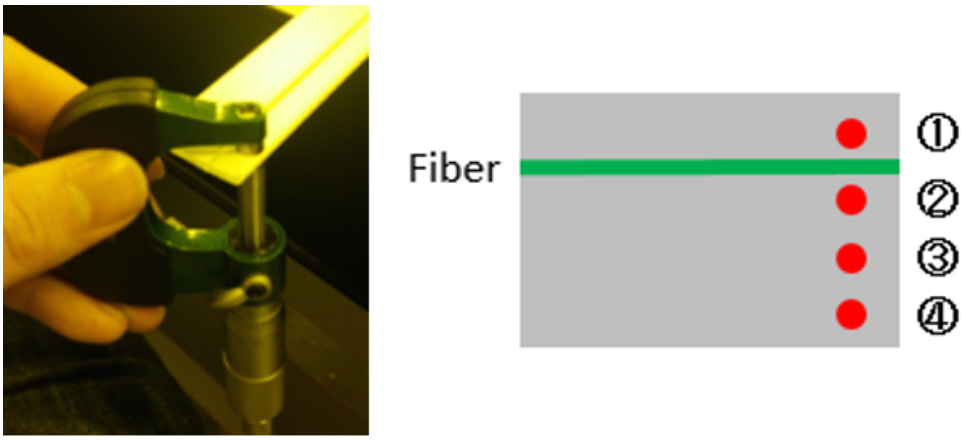

Figure 9.1.3: Thickness measurement

Table 9.1.2: Result of the thickness measurement

Position	Thickness	RMS
①	2.92 mm	0.02 mm
②	3.02 mm	0.02 mm
③	2.94 mm	0.01 mm
④	2.93 mm	0.01 mm
All	2.96 mm	0.04 mm

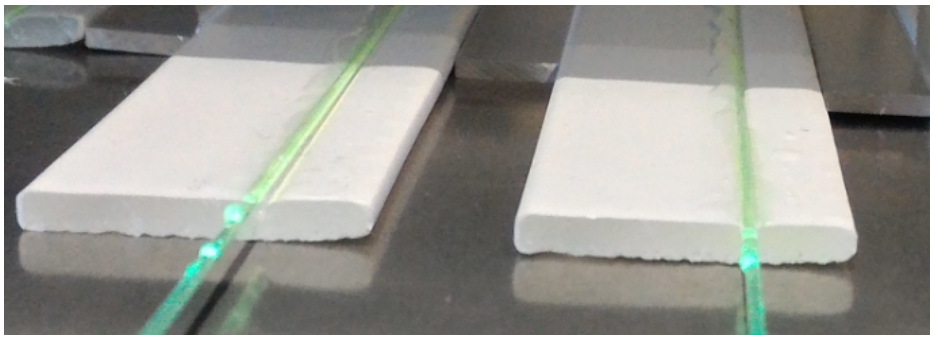

Figure 9.1.4: Cross sectional view of the scintillator : It is not a flat shape.

9.1.3 Weight

We measured the weight of the scintillator with a scaler and a jig box supporting the scintillator, as shown in Fig.9.1.5. Not only the weight of the scintillator but also that of the reflector was measured. In the measurement for the reflector, we just subtract the weight of the scintillator with the reflector from that of it without the reflector. Reflector is painted both on slits of the scintillator and on the fiber, so we measured two types of weight. Table.9.1.3 shows the measurement result of the reflector on slits, and Table.9.1.4 shows the result on the fiber. In both cases, the value fluctuation is about 20%. The reflector painting work was done by our hands, so the amount of the reflector varies person to person. The reflector amount affects the construction of the grid structure[1], so the way to paint it should be improved.

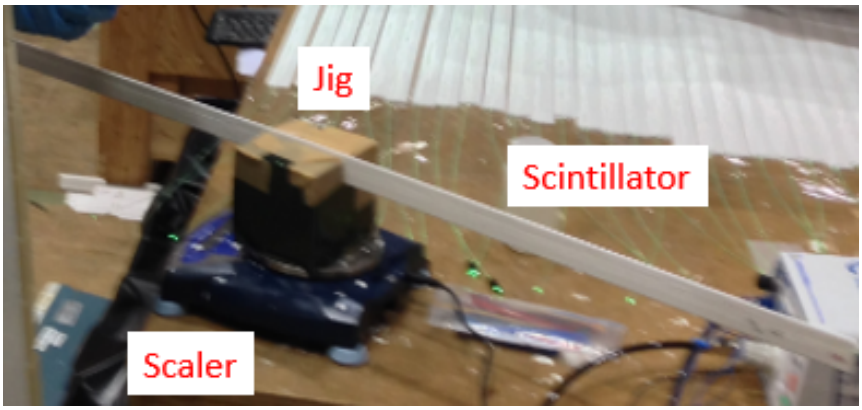

Figure 9.1.5: Weight measurement with the jig box

[1] If the amount of the reflector on the fiber is too large, the grid structure could not be constructed.

Table 9.1.3: Result of the reflector weight measurement on slits of the scintillator

	Weight	RMS
Mean	0.34 g	0.08 g
Max	0.48 g	-
Min	0.07 g	-

Table 9.1.4: Result of the reflector weight measurement on the fiber

	Weight	RMS
Mean	0.69 g	0.13 g
Max	0.99 g	-
Min	0.37 g	-

9.1.4 Density

If we know the weight and volume of the scintillator, we can calculate its density. The weight was already measured as above, so all we should do was to measure the scintillator volume. The measurement was done by tools shown in Fig.9.1.6, using Archimedes' principle. The scintillator is connected with the string by a clip, so we should subtract the clip volume (0.3 g/cm^3) from the measured value. The result is listed on Table.9.1.5. There was no difference between scintillators with slits and without slits.

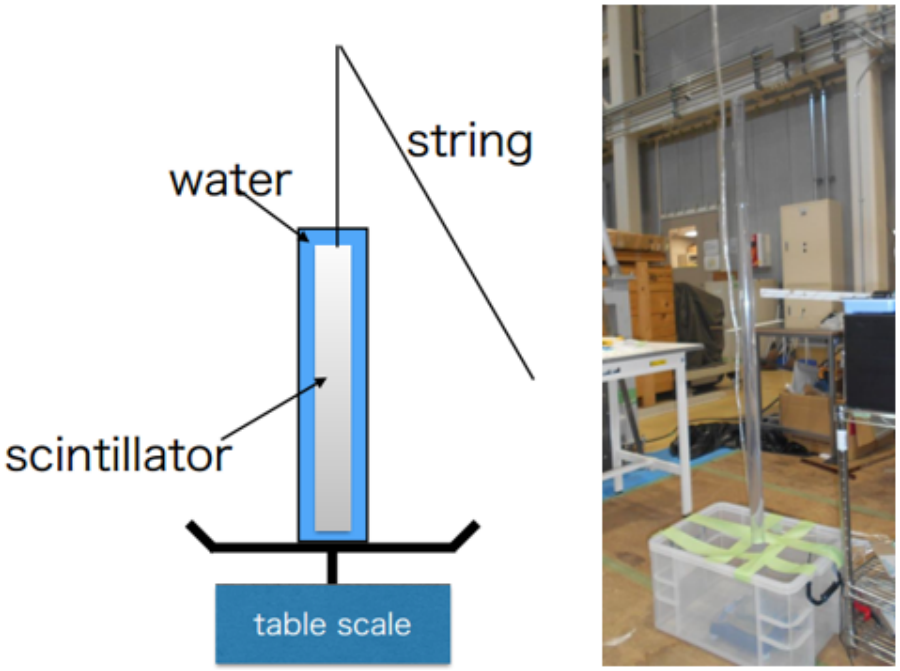

Figure 9.1.6: Illustration and picture for tools to measure the volume of the scintillator

9.2 Measurements of the light yield

We measured by cosmic-rays the light yield of scintillators glued with WLS fibers. The setup is shown in Fig.9.2.1. For the trigger, INGRID type scintillators[2] were used, and scintillators and MPPCs were put in

[2]Scintillators used for the INGRID detector. The size of each scintillator is 1.0 × 5.0 cm^2 and the length of it is 1.2 m.

Table 9.1.5: Result of the reflector weight measurement on the fiber

	Volume	RMS
w/o slits	1.075 g/cm^3	0.01 g/cm^3
w/ slits	1.075 g/cm^3	0.01 g/cm^3
All	1.075 g/cm^3	0.01 g/cm^3

the black box. The temperature in the box was kept in about 24 degrees. In this measurement, we took 100 events for each scintillator. The result is listed on Table.9.2.1. The fluctuation of the mean value is about 17%. Although it is improved from the measurement for the pre-prototype, it is still large. There are two reasons for this. First, some fibers are broken and recessed into the GOMI connector, as shown in Fig.9.2.2. It could result in the very low light yield. Secondly, the fiber polishing was very rough. As mentioned in Sec.6.3.1, it is important to keep a certain distance between the active region of MPPC and edge of the fiber. However, we missed to check the polishing work was complete. If these problems are avoided, the fluctuation will be smaller. Anyway, the mean light yield is enough large, more than 19 p.e. even for scintillators with slits.

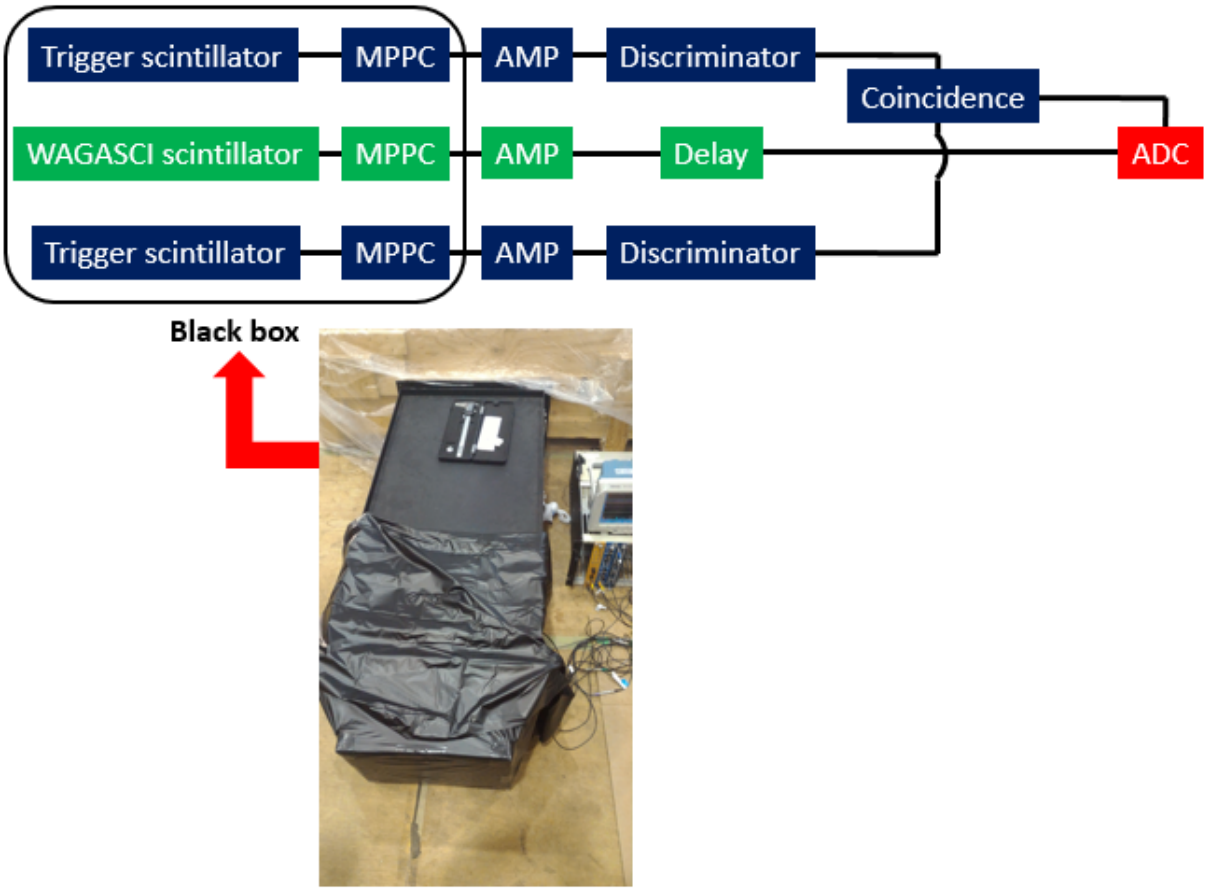

Figure 9.2.1: Setup for the light yield measurement

Table 9.2.1: Result of the light yield measurement by cosmic-rays

	Mean	RMS
w/o slits	22.54 p.e.	4.04 p.e.
w/ slits	19.86 p.e.	3.41 p.e.
All	20.76 p.e.	3.73 p.e.

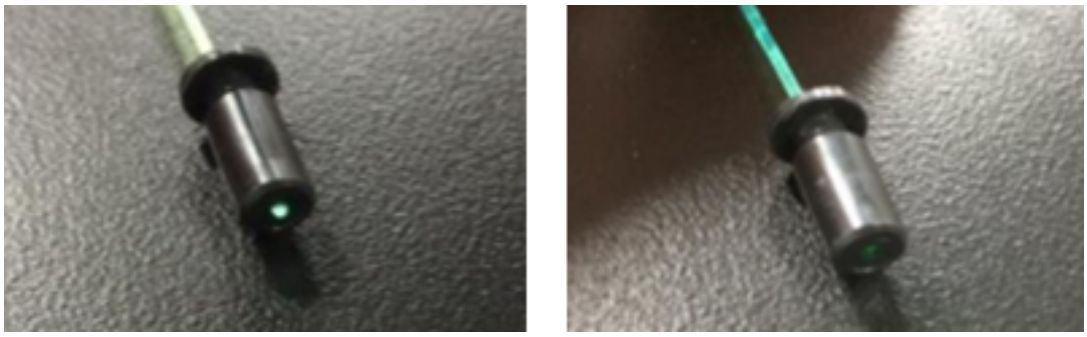

Figure 9.2.2: Picture of the connector with the fiber : The left picture shows the normal state, and the right shows the recessed fiber into the connector.

Chapter 10

Summary

In the T2K experiment, the near-detector INGRID is used for monitoring the intensity and direction of the neutrino beam. One of INGRID modules was moved to the position of an off-axis angle 1.6 degrees in the near-detector hall in order to measure neutrino interactions for sub-GeV region. In this thesis the data taken by this moved module (B2 module) from Jun. 4, 2014 to Dec. 22, 2014 is used for comparing with the Monte Carlo simulation result. There seems to be no contradiction between them at the B2 position. It is also confirmed that the event rate for the B2 module is very stable during the data taking period. The background fraction in the real data is estimated to be about 2 %, and it turns out that events from the upstream wall in the detector hall occupy about 70 % of all background events.

In the near future, a new neutrino detector, named WAGASCI detector, will be installed to the B2 module position in order to reduce the systematic error in the T2K neutrino oscillation analysis due to the target nucleus difference between the near detector ND280 and the far detector SK. The detector has scintillators aligned to the 3D grid-like structure, and thanks to this structure, charged particles which have a large angle to the beam axis are expected to be detected. The thickness of the scintillator is as thin as possible in order to maximize the volume of the beam target. Each scintillator has one groove which has 1.0 mm depth. The WLS fiber is put into the groove and they are glued with the optical cement. We developed a automated gluing system, and the system is using for the detector construction at J-PARC. The light yield of scintillators glued with the fiber was measured by cosmic-rays, and the mean light yield was more than 20 p.e., and it was sufficient value for the detector. Now, a prototype of the WAGASCI detector is under construction, and will be ready to install at the beam axis position by the end of Mar. 2016.

Appendix A

Neutrino interaction

A.1 Charged Current Quasi-Elastic scattering (CCQE)

CCQE interaction (Fig.1.3.1) is a major neutrino interaction in a few GeV region of a neutrino energy. This is a two-body interaction, and if a target nucleus is stationary, the neutrino energy can be reconstructed from the information of a charged lepton :

$$E_\nu = \frac{m_N E_\mu - m_\mu^2/2}{m_N - E_\mu + p_\mu \cos\theta_\mu}, \tag{A.1.1}$$

where E_ν and E_μ are a energy of a neutrino and that of a muon, m_N and m_μ are a mass of the target nucleus and that of a muon, p_μ is a momentum of a muon. It is used for the measurement of energy spectra of the low-energy neutrino beam.

A.2 Charged current Deep Inelastic Scattering (DIS)

DIS interaction (Fig.A.2.1) is a major neutrino interaction in a high energy (ten-odd energy) region, as shown in Fig.2.1.4. It is used for the measurement of energy spectra of the high-energy neutrino beam.

A.3 Single pion production

There are two-type interactions of a single pion production : CC1π and NC1π (Fig.1.3.1), as mentioned in Sec.1.3. SK has the charged-pion detection threshold of about 200 MeV/c, so if the energy of a pion produced by CC1π interaction is lower than the threshold, the pion would be missed and this interaction could be mistaken for CCQE interaction. That is why, CC1π interaction could be a background of the measurement of energy spectra using CCQE interaction. On the other hand, NC1π interaction could be a background of the measurement of the neutrino oscillation via the ν_e appearance because the Cherenkov ring of a electron and that of π^0 in SK is very similar, as described in Sec.2.3.2. If one of γ produced by

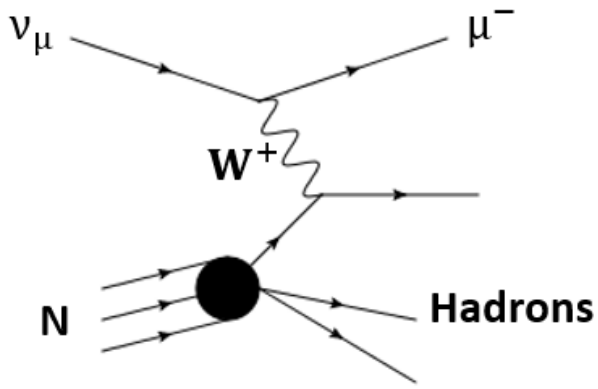

Figure A.2.1: Charged current deep inelastic interaction

the π^0 decay is missed due to the low momentum of the π^0, or if two γ are misidentified as one γ due to the small angle between these γ, this interaction could be mistaken for CCQE interaction.

Appendix B

Construction for the pre-prototype of the WAGASCI detector

B.1 Overview

The pre-prototype detector was constructed from Jan.13, 2015 to Jan.16, 2015 at Kyoto University in order to confirm the possibility to align the 3D grid-like scintillators for the WAGASCI detector. The top view of the detector is shown in Fig.B.1.1 The size of it is 3.5×3.5 cm^2, and the depth is 15 cm. The length of each scintillator is 13 cm, and the dimension of it is shown in Fig.B.1.2. The detector consists of 3 grid-like scintillator layers and 4 horizontal scintillator layers, as shown in FigB.1.3. Spacers are set to fix horizontal scintillators.

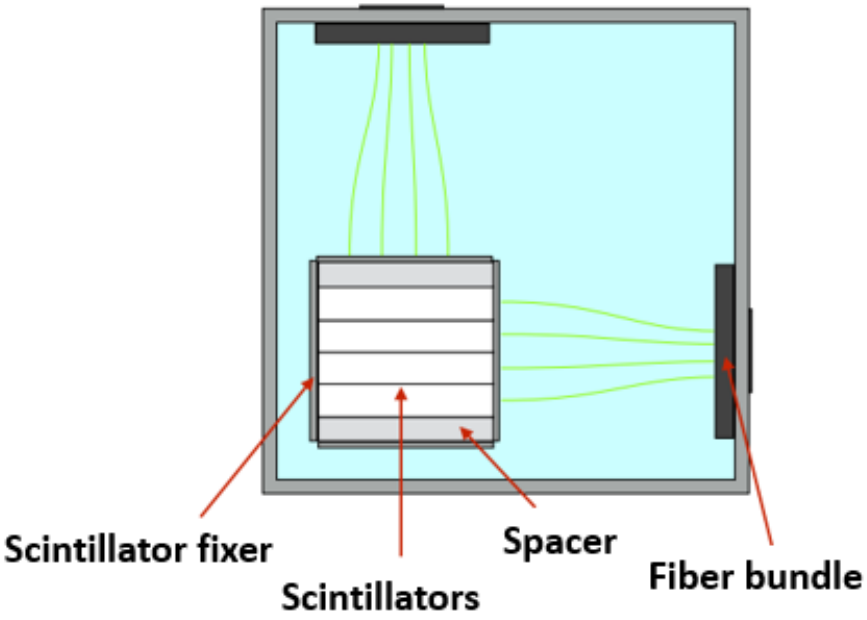

Figure B.1.1: Top view of the pre-prototype detector

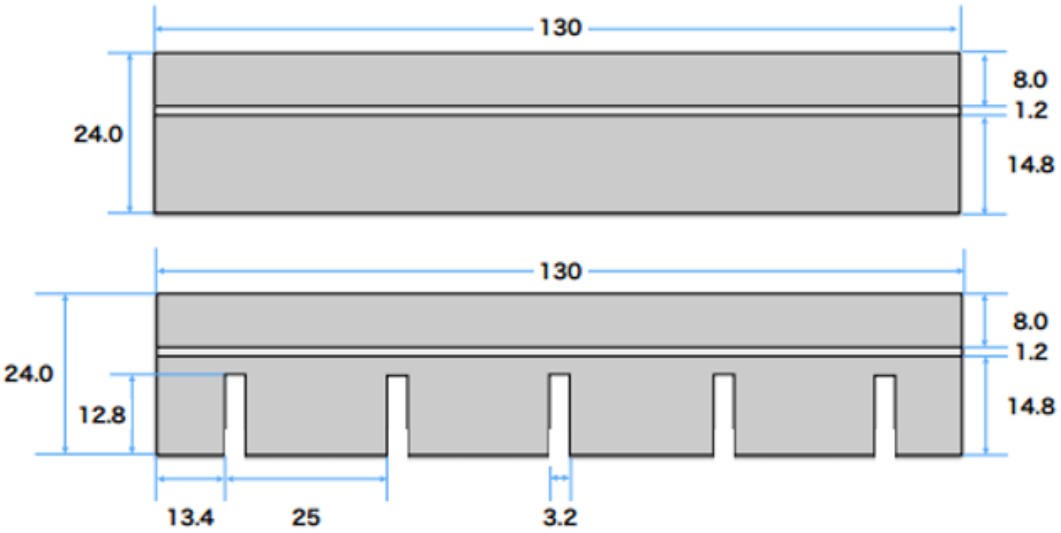

Figure B.1.2: Dimension of the scintillator for the pre-prototoype detector

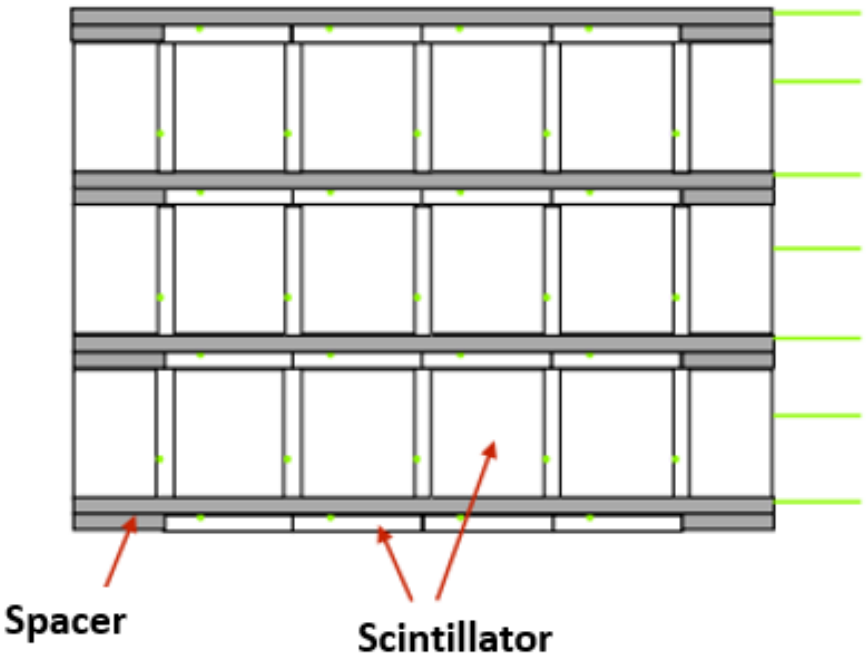

Figure B.1.3: Arrangement of scintillators

B.2 Construction work

In this section, construction work is described with some pictures.

B.2.1 Glue scintillators with WLS fibers

To start with, we glued scintillators and WLS fibers with the optical cement. As shown in Fig.B.2.1, we set rails on both sides of scintillators, and fixed fibers on them. Unlike the method of the WAGASCI detector construction, we put the optical cement on the groove of the scintillator before setting the fiber. The total number of glued scintillators is 66, including spares.

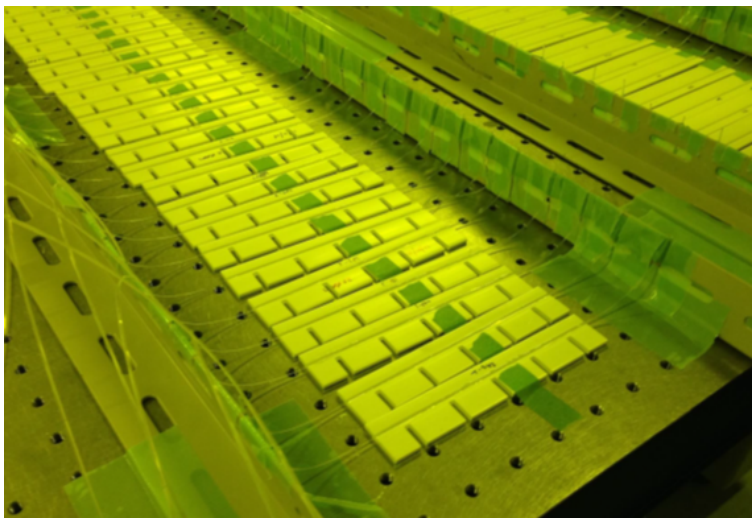

Figure B.2.1: Situation of fiber gluing

B.2.2 Polishing the edge of scintillators

The size of scintillator fixer is so tight that the protruded fiber from the edge of the scintillator could cause the impossibility for scintillators to be set in the fixer. So, we polished the edge of the scintillator by an electric circular saw, as shown in Fig.B.2.2.

B.2.3 Painting the white coating

In order to prevent the crosstalk of scintillators, we painted the white coating, EJ-510, on slits and the edge of each scintillator and on the fiber, as shown in Fig.B.2.3. We used a brush for this painting.

B.2.4 Aligning in a 3D grid-like structure

At first, we aligned scintillators in a 3D grid-like structure, as shown in Fig.B.2.4. Then, we set them layer by layer, as shown in Fig.B.2.5.

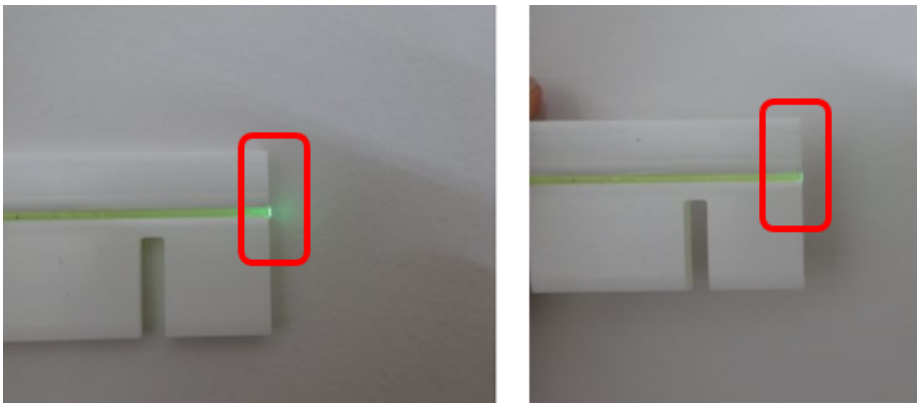

Figure B.2.2: Polish the edge of the scintillator : The right figure shows the edge after polishing.

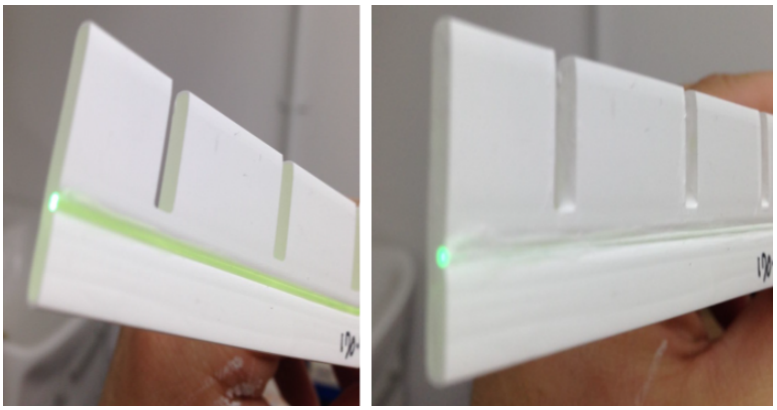

Figure B.2.3: Paint the edge of the scintillator : The right figure shows the edge after painting.

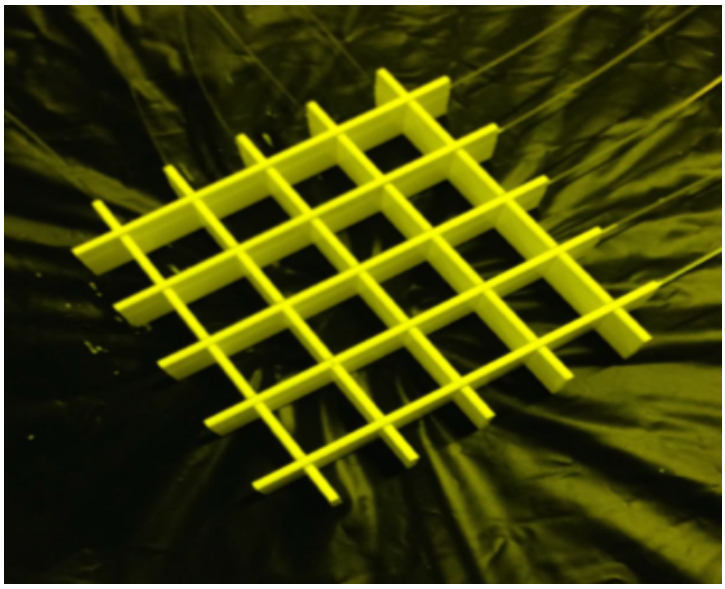

Figure B.2.4: Aligning in a 3D grid-like structure

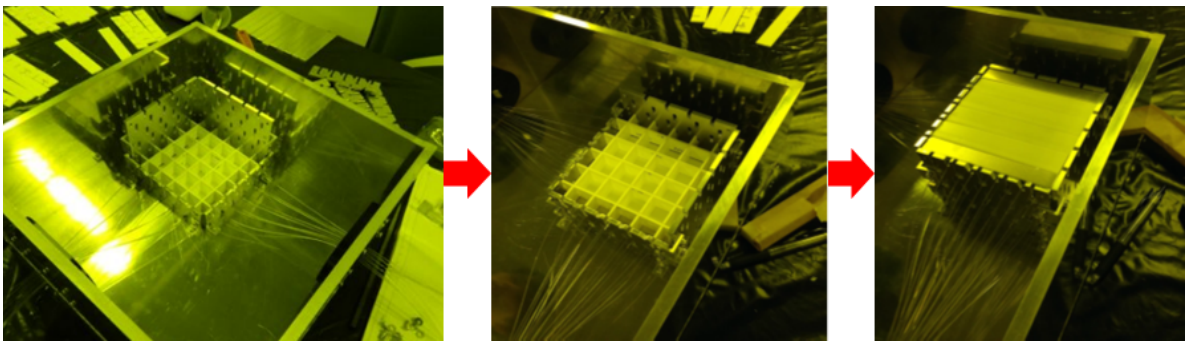

Figure B.2.5: Setting scintillator layers

B.2.5 Gluing WLS fibers with the fiber bundle

For gluing WLS fibers with each fiber bundle, we stood the detector as shown in Fig.B.2.6, in order for the optical cement to go into the hole of the fiber bundle. We used a toothpick for this gluing work, as shown in Fig.B.2.7.

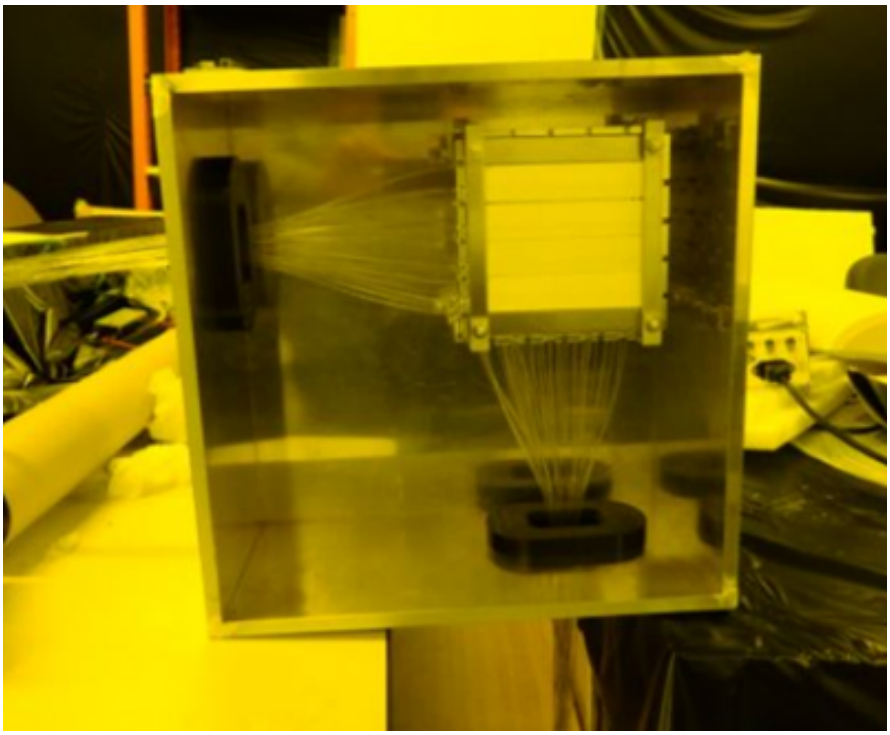

Figure B.2.6: Standing the detector

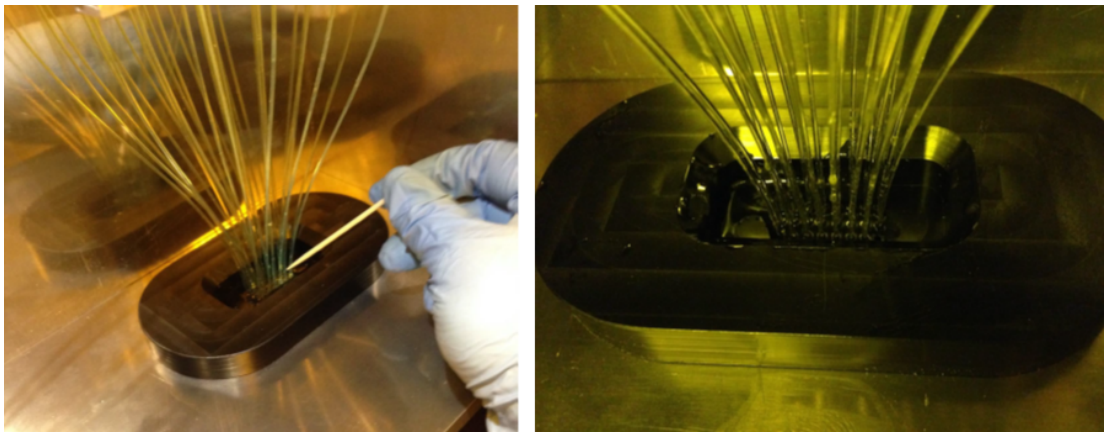

Figure B.2.7: Gluing fibers and the fiber bundle with a toothpick

B.2.6 Polishing the surface of the fiber bundle

In this construction work, fiber bundles for 32 ch array-type MPPC were used only for supporting fibers, and in turn, the bundle for the 64 ch array-type MPPC (Fig.B.2.8) was used for connecting with the MPPC. After inserting fibers into it and gluing them, we polished the surface of it by some sand papers, as shown

in Fig.B.2.9.

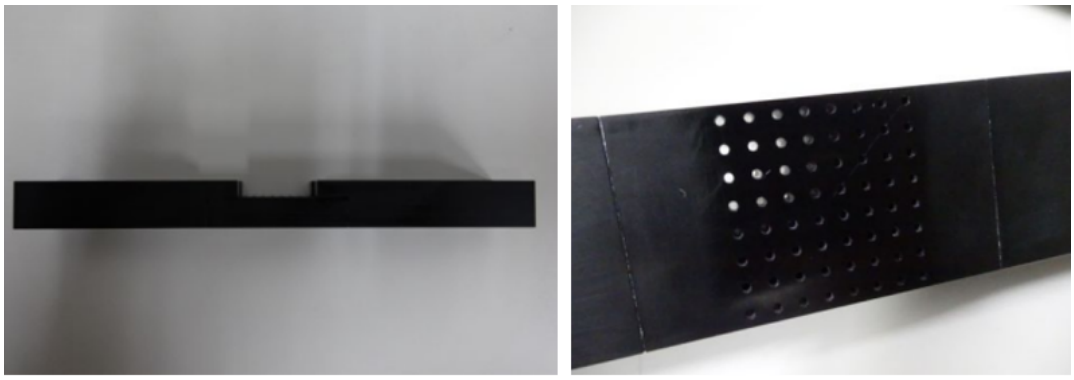

Figure B.2.8: Fiber bundle for the 64ch array-type MPPC

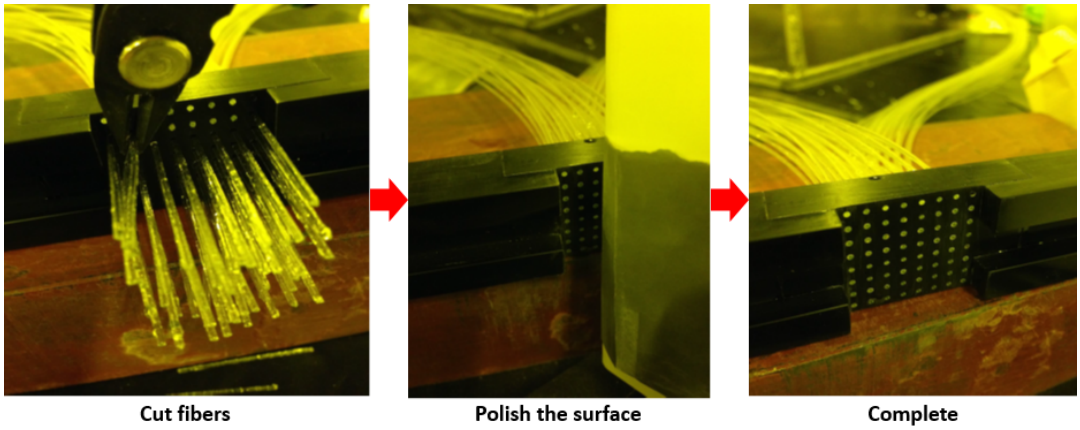

Figure B.2.9: Polishing the surface of the fiber bundle

B.2.7 Water leak test

In order to prevent the water leak, the o-ring was set on each fiber bundle for the 32 ch MPPC. We actually poured the water into the detector, as shown in Fig.B.2.10, and confirmed that the water was not leaked.

B.2.8 Setup

Fig.B.2.11 shows the black box in which we set the pre-prototype detector. Setting situation is shown in Fig.B.2.12, and the connection of the fiber bundle and MPPC is shown in Fig.B.2.13.

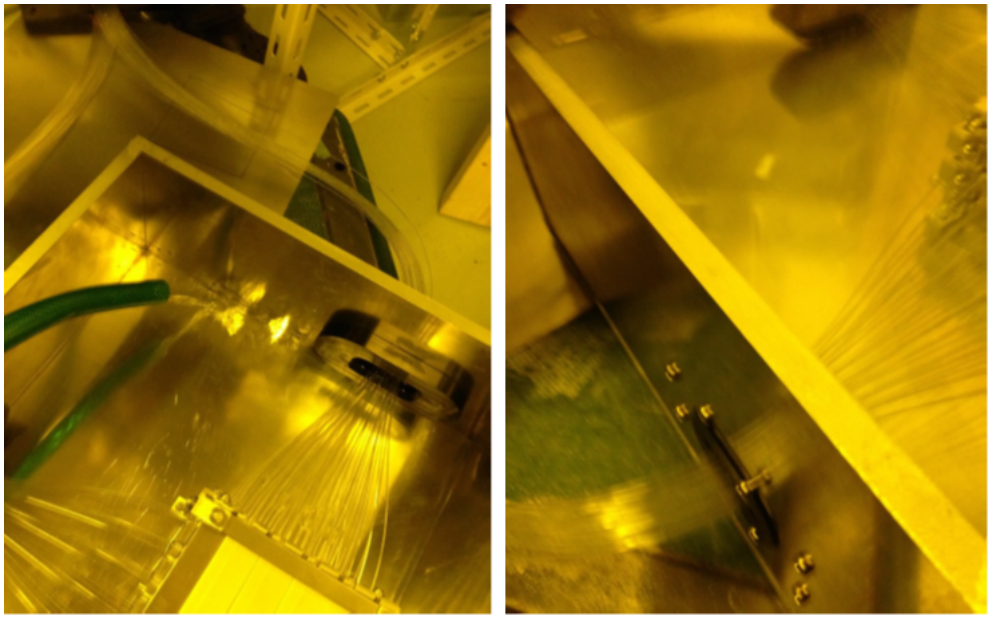

Figure B.2.10: Water leak test

Figure B.2.11: Box for the pre-prototype detector

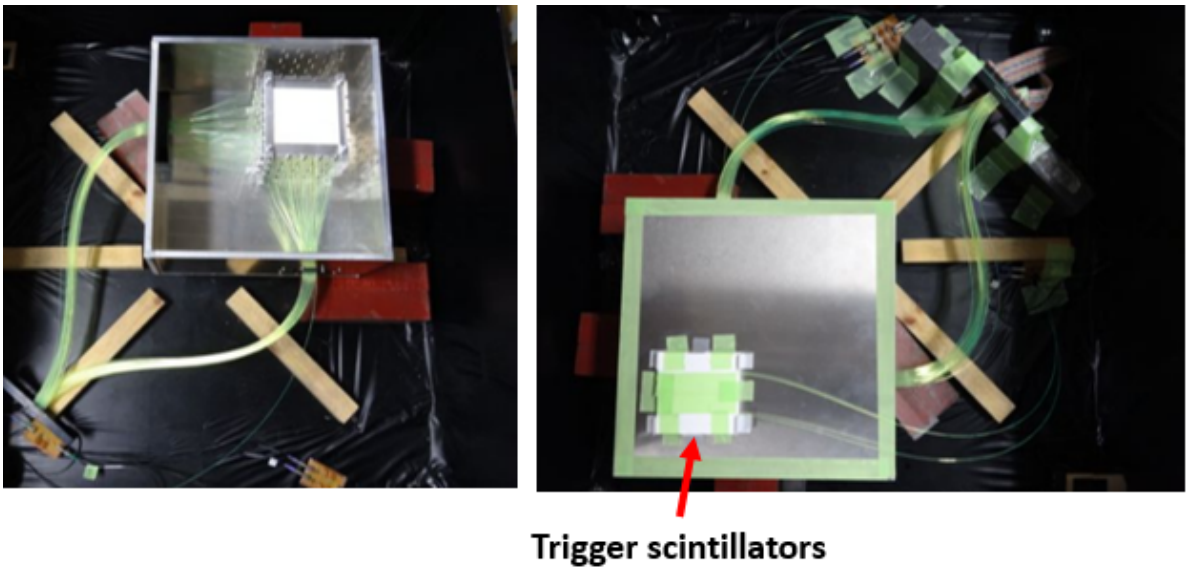

Figure B.2.12: Setup

Figure B.2.13: Connection of the fiber bundle and MPPC

Appendix C

Upgrade plan for the gluing system

Now, we are planning to upgrade the gluing system for the WAGASCI detector construction. In this section, the upgrade plan now under consideration is described.

C.1 Geometry of the aluminum board

Now, the size of the aluminum board is 1100×1300 mm^2, and the shape is rectangular. In the update plan, this size is expanded to 1400×1750 mm^2 and it has a concave shape, as shown in Fig.C.1.1. The hollow enables the board to fix the electrical actuator. The fluctuation of the position of the actuator could cause the nozzle position fluctuation, so it is necessary to stabilize the actuator position.

C.2 New board for replacing scintillators

As explained Sec.8.4, we need to replace scintillators and wait the optical cement to harden. If the scintillators can be moved with the board, it would we are able to set new scintillators on the board soon after the previous gluing work. So, we are planning to prepare the scintillator setting board, as shown in Fig.C.2.1, in order to replace scintillators just after finishing the gluing work. The size and how to fix the scintillator is now under discussion.

C.3 Jigs for attaching the syringe

The syringe fixing jig now we are using is a little weak for the vibration of the horizontal direction. That is why the new jig for fixing the syringe from the side, as shown in Fig.C.3.1, is under preparation. The XY stage will be used in order to adjust the nozzle position easily, and there is a hole in the jig for fixing the tip of the syringe and supporting it from the bottom side. With side boards and the front board, the syringe will be firmly attached to the XY stage.

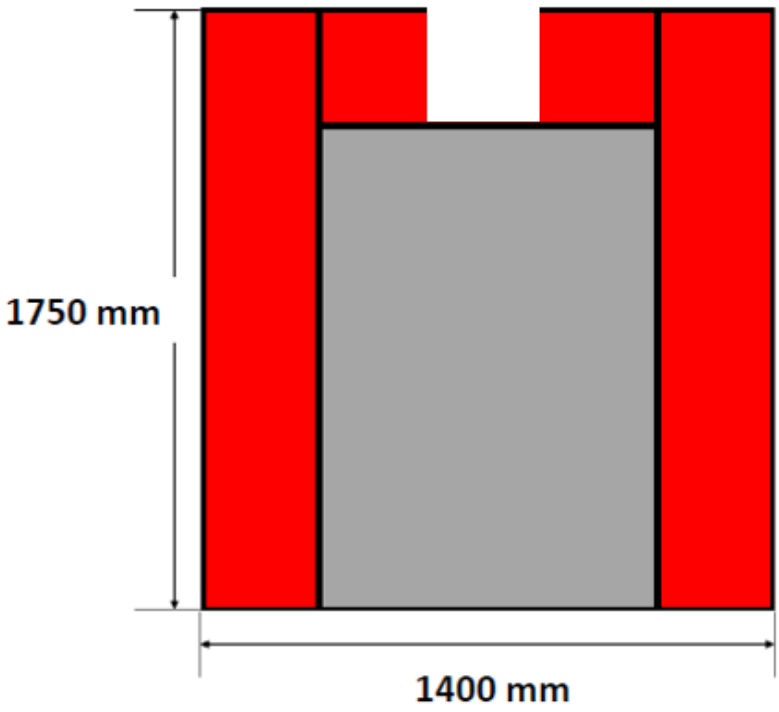

Figure C.1.1: Upgrade plan for the aluminum board : Red regions indicate expanded parts.

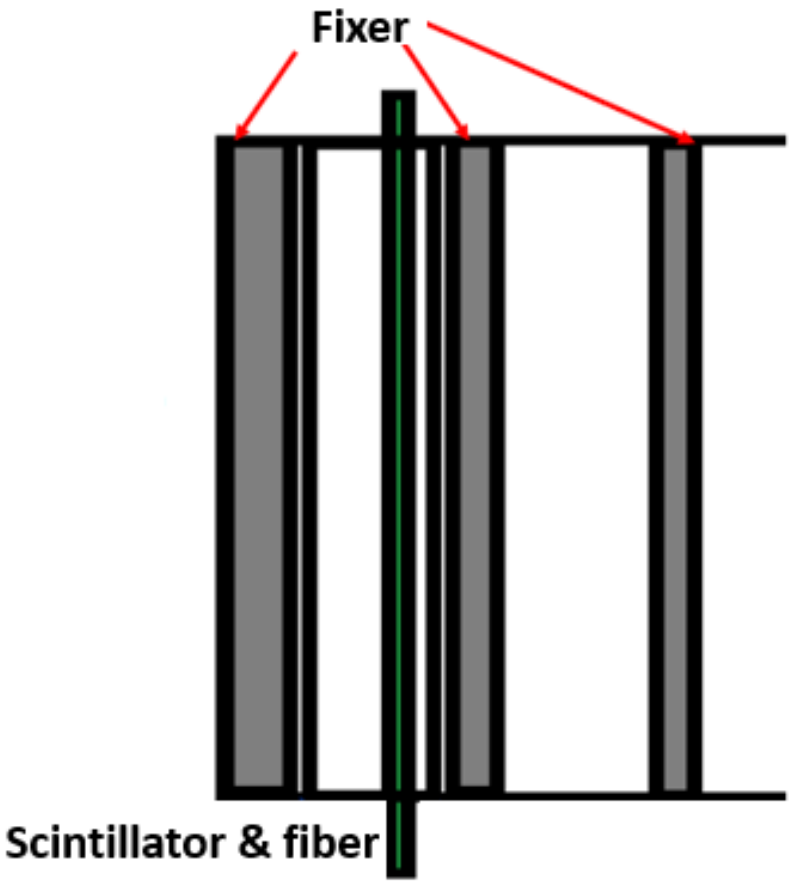

Figure C.2.1: New board plan for replacing scintillators

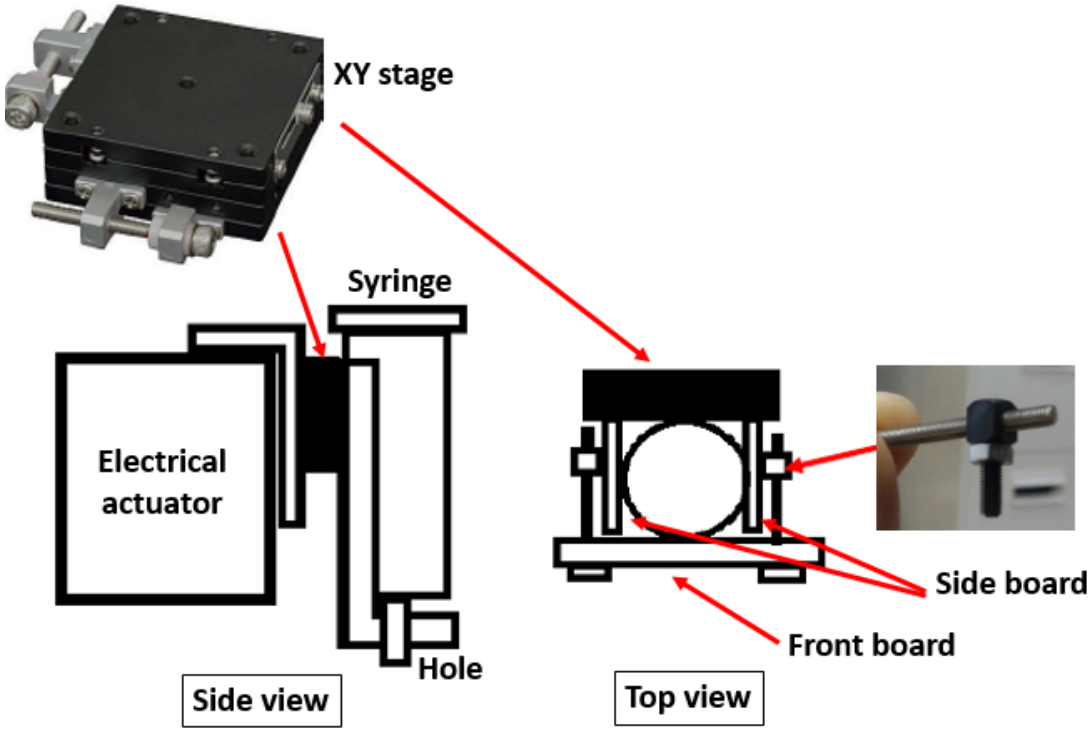

Figure C.3.1: New jig for fixing the syringe

C.4 Painting method for the white reflective coating

The white reflective coating was painted with the brush, so the painted amount varied by a person. The amount is not affected to the detector construction so much, but the extra coating could cause the impossibility to align scintillators for the 3D grid-like structure. So, we are planning to paint it with the gluing system. The brush nozzle (Fig.C.4.1) can be set to the syringe filled with the white coating, and the system operation is same as the gluing work. The possibility to apply the gluing system to the painting work is now under investigation.

Figure C.4.1: Brush nozzle

List of Figures

List of Tables

Bibliography

[1] W. Pauli. “Dear radioactive ladies and gentlemen”. Phys. Today, 31N9:27, 1978.

[2] F. Reines, C. L. Cowan, F. B. Harrison, A. D. McGuire, and H. W. Kruse. “Detection of the Free Antineutrino”. Phys. Rev., 117:159–173, Jan 1960.

[3] G. Danby, J-M. Gaillard, K. Goulianos, L. M. Lederman, N. Mistry, M. Schwartz, and J. Steinberger. “Observation of High-Energy Neutrino Reactions and the Existence of Two Kinds of Neutrinos”. Phys. Rev. Lett., 9:36–44, Jul 1962.

[4] Y. Ashie *et al*. “Measurement of atmospheric neutrino oscillation parameters by Super-Kamiokande I”. Phys. Rev. D, 71:112005, Jun 2005.

[5] Q.R. Ahmad *et al*.. “Measurement of the Rate of $\nu_e + d \rightarrow p + p + e^-$ Interactions Produced by ^8B Solar Neutrinos at the Sudbury Neutrino Observatory”. Phys. Rev. Lett., 87:071301, Jul 2001.

[6] M. H. Ahn *et al*.. “Measurement of neutrino oscillation by the K2K experiment”. Phys. Rev. D, 74:072003, Oct 2006.

[7] D. G. Michael *et al*. “Observation of Muon Neutrino Disappearance with the MINOS Detectors in the NuMI Neutrino Beam”. Phys. Rev. Lett., 97:191801, Nov 2006.

[8] S. Abe *et al*. “Precision Measurement of Neutrino Oscillation Parameters with KamLAND”. Phys. Rev. Lett., 100:221803, Jun 2008.

[9] Y. Abe *et al*. “Reactor $\overline{\nu}_e$ disappearance in the Double Chooz experiment”. Phys. Rev. D, 86:052008, Sep 2012.

[10] F. P. An *et al*. “Improved measurement of electron antineutrino disappearance at Daya Bay”. Chinese Physics C, 37(1):011001, 2013.

[11] J. K. Ahn *et al*. “Observation of Reactor Electron Antineutrinos Disappearance in the RENO Experiment”. Phys. Rev. Lett., 108:191802, May 2012.

[12] T. Kobayashi. High Energy Physics News, Vol. 28, 2009.

[13] K. Abe *etal*. First muon-neutrino disappearance study with an off-axis beam. Phys. Rev. D, 85:031103, Feb 2012.

[14] "J-PARC, Accelerators". http://j-parc.jp/Acc/en/index.html.

[15] "J-PARC, Neutrino Facility: Source of the World's-highest Intense Neutrino Beam". http://j-parc.jp/Neutrino/en/nu-facility.html.

[16] Y. Fujii and Y. Yamada. High Energy Physics News, Vol. 28, 2009.

[17] K. Matsuoka. "Measurement of the Neutrino Beam with the Muon Monitor and the First Result of the T2K Long-Baseline Neutrino Oscillation Experiment". phD thesis Kyoto University, 2007.

[18] S. Aoki, T. Nakaya, and T.Tsukamoto. High Energy Physics News, Vol. 29, 2010.

[19] M. B. Luque *et al*. The construction of the central detector for an experiment at the {CERN} p-p collider. Nuclear Instruments and Methods, 176(1-2):175 – 180, 1980.

[20] J. Altegoer *et al*. The {NOMAD} experiment at the {CERN} {SPS}. Nuclear Instruments and Methods in Physics Research Section A: Accelerators, Spectrometers, Detectors and Associated Equipment, 404(1):96 – 128, 1998.

[21] N. *et al* Abgrall. Time Projection Chambers for the T2K Near Detectors. Nucl. Instrum. Meth., A637:25–46, 2011.

[22] T.Lindner *et al*. The fine grained detector for the t2k experiment. Journal of Physics: Conference Series, 136(4):042035, 2008.

[23] M. Otani and A. Minamino. High Energy Physics News, Vol. 29, 2010.

[24] S. Sakashita and S. Suzuki. High Energy Physics News, Vol. 28, 2010.

[25] M. Otani. "Development and performance test of the neutrino beam monitor INGRID for the T2K long-baseline neutrino oscillation experiment". Master's thesis, Kyoto University, 2008.

[26] "Kuraray, Wavelength Shifting Fibers". http://kuraraypsf.jp/psf/ws.html.

[27] "Hamamatsu, MPPC". http://www.hamamatsu.com/jp/en/4004.html.

[28] N. Abgrall *et al*. "measurement of production properties of positively charged kaons in proton-carbon interactions at 31 gev/*c*". Phys. Rev. C, 85:035210, Mar 2012.

[29] "Geant4 Reference Physics Lists". http://geant4.cern.ch/geant4/support/proc_mod_catalog/physics_lists/referencePL.shtml.

[30] K. Wakamatsu. "Measurement of Neutrino Interactions at Off-axis Angle of 1.65 degrees Using the Neutrino Beam Monitor INGRID for the T2K Long Baseline Neutrino Oscillation Experiment". Master's thesis, Osaka City University, 2015.

[31] T. Koga. "Research and development of a new neutrino detector for precise measurement of neutrino-nucleus cross sections". Master's thesis, University of Tokyo, 2015.

[32] K. *et al* Abe. Measurement of the inclusive ν_μ charged current cross section on iron and hydrocarbon in the T2K on-axis neutrino beam. Phys. Rev., D90(5):052010, 2014.

[33] "Avian-D White Reflective Coating". http://www.aviantechnologies.com/products/coatings/highreflectance.php.

[34] K. Yoshida. "Development for a new neutrino detector, WAGASCI, which has 3D grid-like structure". Master's thesis, Kyoto University, 2015.

[35] "OMEGA, SPIROC 2 User Guide (Draft)". http://indico.cern.ch/event/232082/contribution/0/attachments/385835/536707/Spiroc2_userGuide2009_datasheet.pdf.

[36] "OMEGA, SPIROC Front-end Chip". http://omega.in2p3.fr/index.php/products/spiroc.html.

[37] "OMEGA, EASIROC Front-end Chip". http://omega.in2p3.fr/index.php/products/easiroc.html.